NATIONAL & INTERNATIONAL SCIENTIFIC EVENTS

16th European Conference on Antennas and Propagation (EuCAP 2022)

Venue: IFEMA Palacio Municipal
Location: Madrid, Spain

Begins: March 27, 2022
Ends: April 01, 2022

27th International Conference on Database Systems for Advanced Applications (DASFAA-2022)

Venue: Online Conference
Location: Hyderabad, India

Begins: April 11, 2022
Ends: April 14, 2022

20th International Conference on Soil Mechanics and Geotechnical Engineering (ICSMGE 2022)

Venue: International Convention Centre Sydney
Location: Sydney, Australia

Begins: May 01, 2022
Ends: May 05, 2022

The 31st IEEE International Symposium on Industrial Electronics (IEEE ISIE 2022)

Venue: Dena'ina Center/Egan Center
Location: Alaska, USA

Begins: June 01, 2022
Ends: June 03, 2022

8th European Congress on Computational Methods in Applied Sciences and Engineering

Venue: Norway Convention Center
Location: Oslo, Norway

Begins: June 05, 2022
Ends: June 09, 2022

39th IAHR World Congress

Venue: IAHR World Congress
Location: Granada, Spain

Begins: June 19, 2022
Ends: June 24, 2022

The 75th IIW Annual Assembly and International Conference

Venue: Grand Nikko Tokyo Daiba
Location: Tokyo, Japan

Begins: July 17, 2022
Ends: July 22, 2022

26th International Conference on Pattern Recognition

Venue: Palais des congrès de Montréal
Location: Montréal, Canada

Begins: August 21, 2022
Ends: August 25, 2022

36th European and 12th International Peptide Symposium

Venue: Hotel Meliá Sitges
Location: Barcelona, Spain

Begins: August 28, 2022
Ends: September 02, 2022

16th International Conferance of IACMAG

Venue: Politecnico di Torino
Location: Torino, Italy

Begins: August 30, 2022
Ends: September 02, 2022

27th IFHTSE Congress and European Conference on Heat Treatment 2022

Venue: Wyndham Grand Salzburg Conference Center
Location: Salzburg, Austria

Begins: September 05, 2022
Ends: September 08, 2022

48th Annual Conference of the IEEE Industrial Electronics Society

Venue: SQUARE Conference Center
Location: Brussels, Belgium

Begins: October 18, 2022
Ends: October 21, 2022

Abstracted & Indexed in:
TR Dizin Mühendislik ve Temel Bilimler Veri Tabanı | CrossRef | Google Scholar | MIP Database | StuartxChange | ResearchBib | Scientific Indexing Services (SIS)

HITTITE JOURNAL OF SCIENCE & ENGINEERING

HJSE Official Journal of Hitit University Volume 9, Issue 1, 2022 dergipark.org.tr/en/pub/hjse

---

ISSN 2148-4171

HİTİT UNIVERSITY

JOURNAL OF SCIENCE & ENGINEERING
HITTITE

Volume 9, Issue 1, 2022

dergipark.org.tr/en/pub/hjse

HJSE Official Journal of Hitit University Volume 9, Issue 1, 2022 dergipark.org.tr/en/pub/hjse

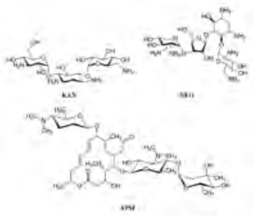

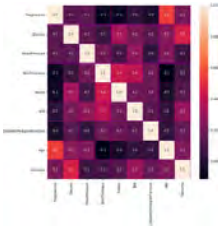

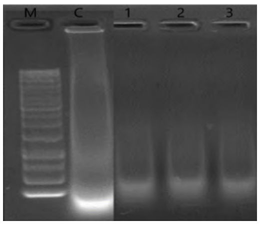
M
C
1
2
3

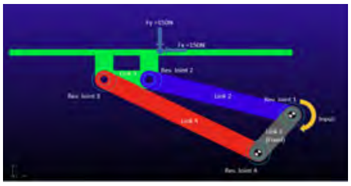

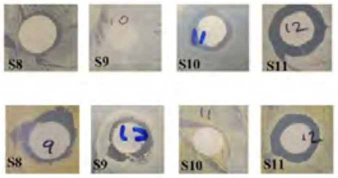
S8
S9
S10
S11
S8
S9
S10
S11

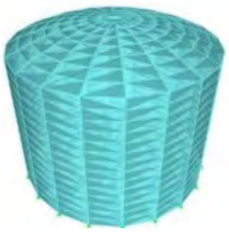

The characterization of X-ray diffraction verified that the ZnO nanosheets had a hexagonal phase and grew along the [002] direction.

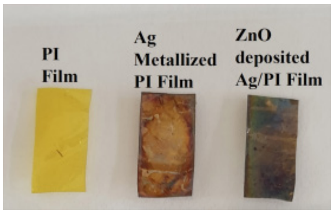

Owner
Prof. Dr. Ali Osman ÖZTÜRK on behalf of Hitit University

Editor-in-chief
Prof. Dr. Ali KILIÇARSLAN

Associate Editors
Prof. Dr. D. Ali KÖSE
Assoc. Prof. Dr. Öncü AKYILDIZ

Production
Assoc. Prof. Dr. Kazım KÖSE
Res. Asst. Dr. Erhan ÇETİN
Res. Asst. Mustafa Reşit HABOĞLU
Res. Asst. Harun Emre KIRAN
Res. Asst. Ömer Faruk TOZLU
Lect. Tugrul YILDIRIM

Editor's Office
Tel: +90 364 227 45 33 / 12 36
Fax: +90 364 227 45 35
Email: alikilicarslan@hitit.edu.tr

Subscription Service:
Tel: +90 364 227 45 33 / 12 82
Fax: +90 364 227 45 35
Email: hjse@hitit.edu.tr

EDITORIAL BOARD

Prof. Dr. Iftikhar AHMAD	University of Malakand, Chakdara, Pakistan
Prof. Dr. Mike BECKETT	Bangor University, Bangor, United Kingdom
Prof. Dr. İbrahim DİNÇER	Uoit Ontario University, Ontario, Canada
Prof. Dr. Ali ELKAMEL	University of Waterloo, Ontario, Canada
Prof. Dr. Mohamad S QATU	Central Michigan University, Michigan, United States
Prof. Dr. Saffa RIFFAT	The University of Nottingham, United Kingdom
Prof. Dr. Thanos SALIFOGLOU	Aristotle University of Thessaloniki, Thessaloniki, Greece
Prof. Dr. Yuehong SU	The University of Nottingham, United Kingdom
Dr. Wojciech NOGALA	Polish Academy of Sciences, Poland
Prof. Dr. Yusuf AYVAZ	Suleyman Demirel University, Turkey
Prof. Dr. Adil DENİZLİ	Hacettepe University, Turkey
Prof. Dr. Ali GENCER	Ankara University, Turkey
Prof. Dr. Metin GÜRÜ	Gazi University, Turkey
Prof. Dr. Murat HOŞÖZ	Kocaeli University, Turkey
Prof. Dr. Sadık KAKAÇ	TOBB University, Turkey
Prof. Dr. Tarık Ömer OĞURTANI	Middle East Technical University, Turkey
Prof. Dr. Ender SUVACI	Anadolu University, Turkey
Prof. Dr. Ali TOPÇU	Hacettepe University, Turkey
Prof. Dr. Kazım Savaş BAHÇECİ	Hitit University, Turkey
Prof. Dr. Cengiz BAYKASOĞLU	Hitit University, Turkey
Prof. Dr. Naki ÇOLAK	Hitit University, Turkey
Prof. Dr. Vedat DENİZ	Hitit University, Turkey
Prof. Dr. Hakan GÜNGÜNEŞ	Hitit University, Turkey
Prof. Dr. Bülent KABAK	Hitit University, Turkey
Prof. Dr. Ali KILIÇARSLAN	Hitit University, Turkey
Prof. Dr. Dursun Ali KÖSE	Hitit University, Turkey
Prof. Dr. İrfan KURTBAŞ	Hitit University, Turkey
Prof. Dr. İbrahim SÖNMEZ	Hitit University, Turkey
Assoc. Prof. Dr. Seyfi ŞEVİK	Hitit University, Turkey
Prof. Dr. Dilber Esra YILDIZ	Hitit University, Turkey

MASTHEAD

Journal Name : HITTITE JOURNAL OF SCIENCE AND ENGINEERING
Year : 2022
Managing Editor : Prof. Dr. Ali KILIÇARSLAN
Managing Office : Hitit University Faculty of Engineering
Managing Office Tel : +90 364 227 45 33 / 12 36
Publication Language : English
Publication Type : Peer Reviewed, Open Access, International Journal
Delivery Format : 4 times a year (quarterly)
Print ISSN : 2149-2123
Online ISSN : 2148-4171
Publisher Address : Hitit Üniversitesi Kuzey Kampüsü Çevre Yolu Bulvarı
19030 Çorum / TÜRKİYE
Publisher Tel : +90 364 227 45 33/1236

EDITORIAL

This new issue of Hittite Journal of Science and Engineering contains twelve manuscripts from different disciplines science and engineering. These manuscripts was first screened by Section Editors using plagiarism prevention software and then reviewed and corrected according to the reviewer's comments. I would like to express my gratitude to all our authors and contributing reviewers of this issue.

I would like to thank to the new President of Hitit University, Prof. Dr. Ali Osman Öztürk, for his support and interest in HJSE and also to the Associate Editors of HJSE, namely Prof. Dr. Dursun Ali Kose and Asst. Prof. Dr. Oncu Akyildiz, as well as our Production Editors Dr. Kazim Kose, Mustafa Reşit Haboğlu, Erhan Çetin, Tugrul Yildirim, Harun Emre Kıran and Ömer Faruk Tozlu for their invaluable efforts in making of the journal.

It's my pleasure to invite the researchers and scientists from all branches of science and engineering to join us by sending their best papers for publication in Hittite Journal of Science and Engineering.

Dr. Ali Kilicarslan

Editor-in-Chief

Hittite Journal of Science and Engineering, 2022, 9 (1) 01–07
ISSN NUMBER: 2148–4171
DOI: 10.17350/HJSE19030000249

Selective Recognition of Kanamycin via Molecularly Imprinted Nanosensor

Esma Sari
Yuksek Ihtisas University, Department of Medical Laboratory Techniques, Ankara, Turkey

Article History:
Received: 2022/02/15
Accepted: 2022/02/28
Online: 2022/03/30

***Correspondence to**: Esra Sari,*
Yüksek Ihtisas University, Medical Laboratory Techniques, 06291, Ankara, Turkey.
E-Mail: esmasariuzek@yiu.edu.tr
Phone: +90 (312) 329 7425
Fax: +90 (312) 329 1421

ABSTRACT

Herein, the molecular recognition sites on the surface of the chip were created by the molecular imprinting method to produce the surface plasmon resonance (SPR) based nanosensor for the real-time kanamycin (KAN) detection. Firstly, kanamycin imprinted nanofilm, which has specific recognition cavities for kanamycin were synthesized by in-situ radical polymerization. Fabricated nanofilm for the detection of kanamycin was characterized with FTIR, ellipsometer, and atomic force microscope by the means of structurally and morphologically. The mean thickness values were determined for the imprinted and non-imprinted nanofilms as 102.4±3.1 nm and 101.8±4.7, respectively. The sensitivity performance of imprinted nanosensor was investigated by using the KAN solutions at different concentrations (25-200 ng/mL). The refractive index and the KAN concentration were found to be in perfect agreement with a regression coefficient (R^2, 0.992). The detection limit was calculated as 0.40±0.05 ng/mL by using the equation in the calibration curve. The response of imprinted and nonimprinted nanosensors towards the chemical analogs of KAN (NEO and SPM) were investigated to prove the selectivity of KAN imprinted nanosensors. The reusability performance of imprinted nanosensor was investigated by spiking 25 ng/mL KAN solution with three replicates. When the kinetic analyzes were examined, high sensitivity real-time kanamycin analysis was performed at very low concentrations with good reusability.

Keywords:
Kanamycin; Surface plasmon resonance; Molecular imprinting; Nanosensor.

INTRODUCTION

Kanamycin (KAN) indicates two forms of aminoglycoside, a crystalline monosulfate monohydrate, and salt with a higher sulfate content [1]. Due to their low cost of production, these compounds are widely used in the treatment of narrow therapeutic indexes, especially in veterinary medicine [2-5]. Despite its widespread use in the form of injections and capsules as a second-line antibiotic, there is increasing concern about KAN overuse, as well as overconsumption of KAN-containing animal-derived food because it could induce accumulation in an animal body and transferred into the food chain [3, 5, 6]. Residues of kanamycin were found to imperil people's health, causing severe side effects such as hearing loss, kidney damage, and allergic shock [3, 7]. In this sense, there are effective strategies accessible for kanamycin detection in various mediums. Until now, numerous analytical methods have been applied for the KAN detection such as spectrophotometry [3, 6], cantilever array sensor [5], high performance liquid chromatography (HPLC) [8, 9], solid-phase extraction (SPE) [9], electrochemical [4, 7, 10], mass spectrophotometry (MS) [9], capillary electrophoresis [11, 12]. While substantial contributions and recompensing results have been provided to the KAN detection, the majority of these methods are time-consuming, laborious, and complicated [2, 6, 7]. Furthermore, they often entail a significant amount of raw material, professional personnel, and costly equipment [2, 6, 10]. Therefore, rapid, simple, and low-cost methods for sensitive and selective KAN detection need to be developed. The molecular imprinting technique (MIT) is a powerful tool to create selective recognition regions on the surface of interest [7, 13-16]. There are many applications such as drug delivery [17], diagnostics [18], biosensors [19], forensic science [20], regenerative medicine [21], tissue engineering [22], etc. that is used effectively and successfully to obtain high sensitivity, specificity, and accuracy. Surface plasmon resonance (SPR) with undeniable advantages is a suitable platform to obtain a low detection limit for the sensing application of MIT [23-25]. The sensing system produced by the combination of SPR and MIT is widely used in the detection of cells [20], pathogens [21, 26], biomolecules [27, 28], drugs [29], antibiotics [30-32], etc.

Herein, the nanosensor fabricated via MIT was developed to detect KAN with sensitivity and selectivity by using SPR. The KAN imprinted nanofilm which has specific recognition cavities for KAN were synthesized by in-situ radical polymerization on the chip surface. Before kinetic measurement of SPR chip surfaces with KAN imprinted nanofilms, FTIR, Ellipsometer, and AFM were used for the characterization of nanofilms on the surface of chips. The responses of nanosensors against KAN and competitors were investigated for selectivity studies. The KAN detection using the assay was successful, with high selectivity and sensitivity.

MATERIAL AND METHODS

Materials

Kanamycin (KAN), neomycin (NEO), spiramycin (SPM), allyl mercaptan, ethylene glycol dimethacrylate (EGDMA), methacrylic acid (MAA), and 2-hydroxyethyl methacrylate (HEMA), were obtained from Sigma Chemical Co (St. Louis, USA). Gold SPR chips were supplied from Horiba (UK). All other chemicals were of reagent grade and supplied from Sigma Chemical Co (St. Louis, USA) and Merck A.G (Darmstadt, Germany). All kinetic measurements were carried out with the SPR system (GenOptics, SPRi-Lab, Orsay, France). Barnstead D 3804 NANOpure cartridge with cellulose-containing Barnstead (Dubuque, A) RO pure LP reverse-osmosis unit was utilized for the purification of water used in all experiments.

Functionalization of the chip surface

The chip surface was functionalized with allyl mercaptan (CH_2CHCH_2SH). Before the modification, acidic piranha solution (3:1, H_2SO_4 / H_2O_2) was utilized to clean the gold surface. Then, ethyl alcohol was used as a washing solution for the cleaned chips, and the chips were placed to dry in a vacuum oven (200 mmHg, 40°C) for 3 hours. 10 µl of allyl mercaptan was applied to the cleaned SPR chip surface and allowed to stand for 12 hours. Following this, the final chips were washed with ethanol and dried in a nitrogen atmosphere. The modification resulted in the functionalization of the chip surface with allyl groups.

In situ synthesis of nanofilms

The following process was carried out for the fabrication of nanofilm on the surface of chips. The KAN selective molecularly imprinted nanofilm was obtained from the polymerization of MAA-KAN pre-complex towards EGDMA as a crosslinker and HEMA as a co-functional monomer. For the preparation of MAA-KAN pre-complex, 2 mg of KAN was complexed with 7.25 µL of MAA by providing a 1:5 (mmol) template molecule and functional monomer ratio. The pre-complex was dissolved by mixing 41 µL of toluene and 164 µL of ACN to obtain a homogeneous solution of the pre-complex. 13.4 µL of HEMA monomer and 27.7 µL of EGDMA crosslinker were added to the pre-complex solution. After adding AIBN (10 mg) as initiator, the final solution (5 µL) was dripped on the pre-vinylated chip. The prepared chip was placed under a UV lamp and polymerization was achieved by photopolymerization for 75 minutes. The unreacted monomer was removed with ethyl alcohol. The ratio of the crosslinker, monomer, and template molecule is 20:14:1, respectively. The percentage of monomer in solution was determined as 25 % (w/v). After the polymerization steps, the imprinted nanofilm-coated SPR chip was washed with methanol and acetonitrile solution (4:1, MeOH:MeCN) to extract the template. The KAN imprinted nanofilm was washed with this desorption solution at room temperature for one hour, renewing the desorption solution every ten minutes. This process was repeated until KAN could not be detected by UV spectrophotometer at 276 nm. To prove the selectivity of KAN imprinted nanofilm, the non-imprinted nanofilm was also fabricated in the same manner as described earlier without adding KAN.

Characterization of nanofilms

The thickness measurements on the surfaces of the prepared sensors were characterized by Nanofilm EP3-Nulling Ellipsometer (Göttingen, Germany). The laser with the wavelength of 532 nm at an incidence angle of 62° was used to perform thickness measurements. The SPR sensor is positioned beneath the laser light source. The average of the kinetic measurement results repeated three times in six different regions is reported. The contact angles of nanofilms were measured using a KRUSS DSA100 (Hamburg, Germany) instrument. The contact angles were determined by pouring water on the SPR chip surfaces using the Sessile Drop technique. For each drop, five independent photographs were taken from different regions of the chip surface to calculate contact angle data. Five independent photographs were recorded from various regions of the surface of the chips, and the contact angle data were calculated for each drop. The structural characterization of the nanofilm surfaces was carried out using Fourier transform infrared spectrometer (Thermo Fisher Scientific, Nicolet iS10, Waltham, MA, USA).

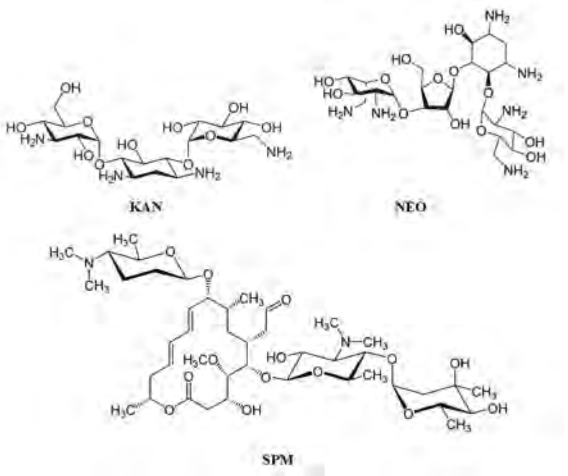

Figure 1. The molecular structures of KAN, NEO and SPM.

SPR measurement

Kinetic measurements by the KAN imprinted nanosensors were carried out by surface plasmon resonance. The kanamycin solutions at different concentrations (25-200 ng/mL) were interacted with SPR nanosensors by a peristaltic pump and kinetic data were obtained using SPRview software.

The following steps were applied for the real-time SPR analysis: first equilibrium buffer (Phosphate buffer, 10 mM, pH 7.5) then KAN solution was passed through the system until the system reached equilibrium again, and the desorption solution (2.0 M NaOH) was used in the last step. In all measurements, the equilibrium buffer waited for 5 minutes and kanamycin solution was waited for 10 minutes for the system to reach equilibrium. Desorption and regeneration processes were carried out in about 15 minutes. The isotherm models can be applied to examine the interaction between the imprinted nanosensor and KAN in the graphs. The response of imprinted and nonimprinted nanosensors towards the chemical analogs of KAN (NEO and SPM) were investigated to prove the selectivity of KAN imprinted nanosensors. The molecular structures of KAN, NEO and SPM were given in Figure 1. The reusability performance of imprinted nanosensor was investigated by spiking 25 ng/mL KAN solution with three cycles.

RESULTS AND DISCUSSION

Characterization

The average surface thickness of the nanofilm was investigated through spectroscopic ellipsometry. As seen in Figure 2, the mean thickness values were determined for the imprinted and non-imprinted nanofilms as 102.4±3.1 nm and 101.8±4.7, respectively.

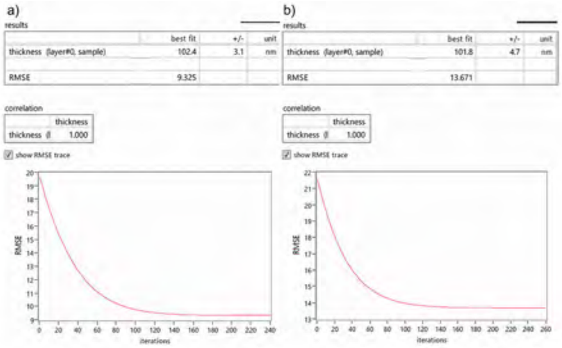
a)

results

	best fit	+/-	unit
thickness (layer#0, sample)	102.4	3.1	nm
RMSE	9.325		

correlation

	thickness
thickness (I	1.000

☑ show RMSE trace

b)

results

	best fit	+/-	unit
thickness (layer#0, sample)	101.8	4.7	nm
RMSE	13.671		

correlation

	thickness
thickness (I	1.000

☑ show RMSE trace

Figure 2. The molecular structures of KAN, NEO and SPM.

The surface hydrophobicity of the SPR chip surface was investigated by taking the contact angle measurements. The contact angles of imprinted, nonimprinted, and unmodified SPR chips were measured as 60.5°, 62.2°, and 76.4°, respectively (Figure 3). The decreasing of contact angle values indicates an increment in wettability as a result of the decrease in hydrophobicity. The imprinted and nonimprinted nanofilms synthesized on the chip surface have a hydrophilic character originating from the monomers (HEMA, EGDMA, and MAA) used, therefore, as expected, the contact angles are lower than the unmodified SPR chip.

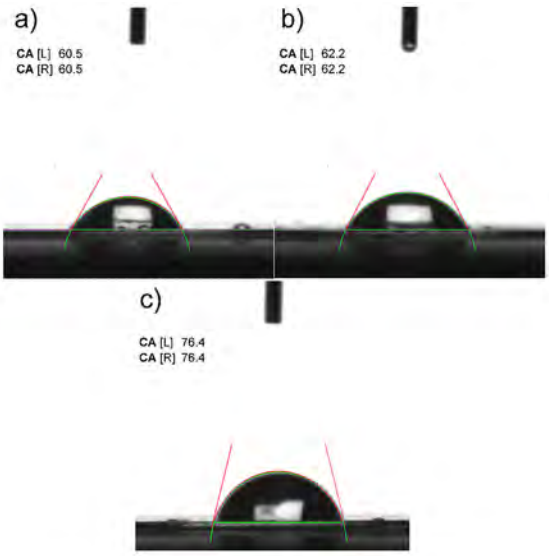

Figure 3. Contact angle measurement of SPR chips: imprinted (a), nonimprinted (b), and unmodified (c).

FTIR-ATR spectroscopy analysis was carried out for the structural characterization of nanofilms. The similarities in the chemical structures of nanofilms caused by crosslinker and functional monomers are clearly visible in FTIR-ATR spectra (Figure 4). The most prominent bands in the spectra, as shown in Figure 4, were O–H stretching bands, which correspond to the hydroxyl group of HEMA at about 3200–3300 cm^{-1}; aliphatic C–H stretching bands, which correspond to the methyl group of MAA and EGDMA at about 2900–3000 cm^{-1}; and C=O stretching bands, which correspond to the carbonyl group of MAA, HEMA and EGDMA at about 1700–1750 cm^{-1}; aliphatic C–H bending bands corresponds to the methyl group of MAA and EGDMA at about 1400– 1500 cm^{-1}; C–O stretching bands corresponds to the carboxyl group of MAA, HEMA and EGDMA at about 1150–1250 cm^{-1}. These bands in both spectra demonstrated the presence of MAA and HEMA in the structure of nanofilms.

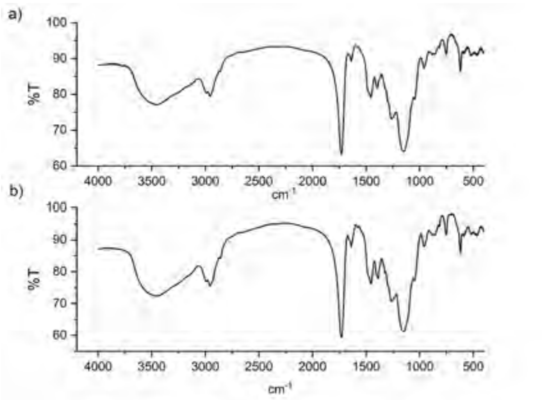

Figure 4. FTIR analysis of imprinted (imprinted) and nonimprinted (nonimprinted) nanofilms.

Kinetic and Equilibrium Analysis

To evaluate the relationship between SPR signal and kanamycin concentration, kanamycin solutions at various concentrations (25-200 ng/mL) were analyzed by the KAN imprinted nanosensor (Figure 5). The changes in the refractive index versus time were given in Figure 4a by applying the KAN solutions at the different concentrations to the imprinted nanosensors. As can be seen from the figures, the % refraction value increases with the application of kanamycin to the imprinted SPR nanosensor. The reason for this can be shown as the increase in the concentration difference, which is the driving force between the kanamycin solution and the surface. As seen in Figure 5, the % refraction value increases with the application of kanamycin to the surface. In a standard measurement; equilibrium solution was passed through the system first, then kanamycin solution until the system reached equilibrium again, and desorption solution was used in the last step. In all measurements, approximately 20 minutes were waited for the system to reach equilibrium. Desorption and regeneration processes were carried out in about 15 minutes. It was observed that the % refraction value increased greater with increasing the concentration. The reason for this can be explained as the increase in the concentration difference, which is the driving force between the KAN solution and the surface of imprinted nanofilm. The amount of KAN can be determined by using the calibration plot giving the relationship between SPR signal and KAN concentration in Figure 5b. The refractive index and the KAN concentration were found to be in perfect agreement (R2, 0.992). The detection limit was calculated as 0.40±0.05 ng/mL by using the calibration curve. When the kinetic analyzes were examined, high sensitivity real-time kanamycin analysis was performed at very low concentrations. Considering the importance of detecting residues of kanamycin for human health even at low concentrations, this method is thought to be a very successful technique for kanamycin analysis compared to literature (Table 1).

It is required to determine the binding parameters from the measurements of the process to quantify binding features. For the determination of constants, the models, whose equations are given below, are applied to the data [37-39].

$$Association\ kinetic\ analysis\ \frac{d\Delta R}{dt} = k_a C(\Delta R_{\max} - \Delta R) - k_d \Delta R \tag{1}$$

$$Scatchard\ \frac{\Delta R_{ex}}{[C]} = K_A(\Delta R_{\max} - \Delta R_{eq}) \tag{2}$$

$$Freundlich\ \Delta R = \Delta R_{\max}[C]^{\frac{1}{n}} \tag{3}$$

$$Langmuir\ \Delta R = \left[\frac{\Delta R_{\max}[C]}{K_d + [C]}\right] \tag{4}$$

$$Langmuir - Freundlich\ \Delta \mathrm{R} = \left[\frac{\Delta R_{\max}[C]^{\frac{1}{n}}}{K_d + [C]^{\frac{1}{n}}}\right] \tag{5}$$

where dR/dt is the change of the refractive index in unit time, R and R_{max} are experimental sensor responses measured during analyte molecule binding (Reflectivity %/s) and theoretical maximum sensor response, C is the concentration (M), k_a is the association rate constant (L/mol.s), k_d is the dissociation rate constant (1/s), and 1/n is the Freundlich heterogeneity index. The association constant, K_a, can be computed as $K_a = k_a/k_d$ (L/mol), while the dissociation constant, K_d (mol/L), is equal to $1/K_a$.

Table 1. The comparison of studies for the detection of KAN in literature.

Technique	Method	LOD (nM)	[R]
SPR	Aptamer based sensing	285	31
SPR	Molecular imprinting	12	32
Colorimetric	Aptamer based sensing	25	33
Fluorometric	Oligonucleotide	0.37	34
Electrochemical	Aptamer based sensing	2.37	35
Colorimetric	Chitosan-wrapped gold nanoparticles	8.0	36
SPR	Molecular imprinting	0.8	This study

The rate and equilibrium parameters reveal the intensity of association and dissociation tendency for the interaction of surface and molecule. As shown in Table 2, the association rate constant and s for (k_a) and the dissociation rate constant (k_d) were calculated as 2.2x10^2 M.s^{-1} and 2.8x10^{-3} s^{-1}, respectively, while the association (K_a) and dissociation (K_d)

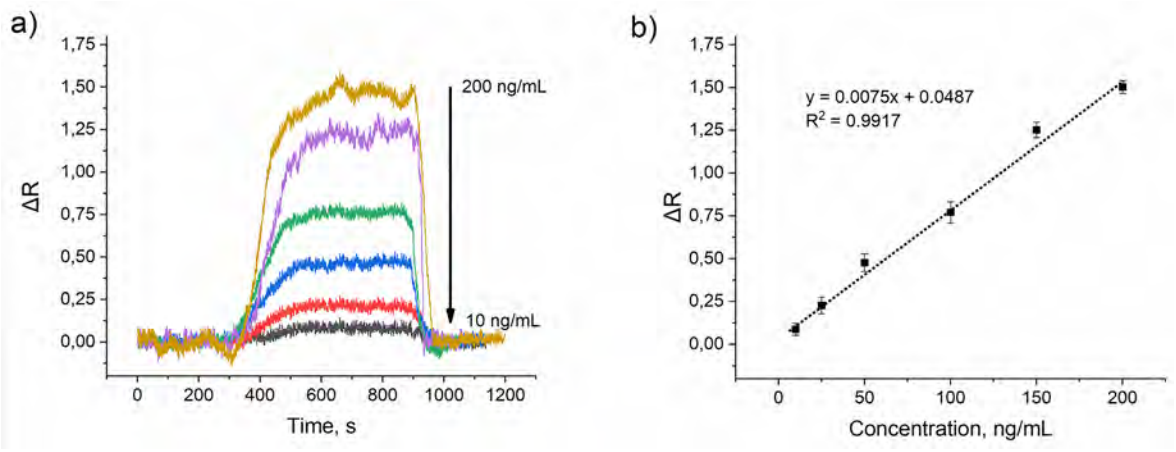

Figure 5. Real-time analysis of KAN with ERY via imprinted nanosensor: effect of concentration on the signal of imprinted SPR nanosensors (a) and the calibration curve obtained by plotting KAN concentration versus. ΔR (b).

Table 2. The comparison of studies for the detection of KAN in literature.

Association Analysis		Scatchard Analysis	
k_a (M.s^{-1})	2.2 x 10^2	ΔR_{max}	9.78
k_d (s^{-1})	2.8 x 10^{-3}	K_a (M^{-1})	4.1 x 10^5
K_a (M^{-1})	7.7 x 10^5	K_d (M)	2.4 x 10^{-6}
K_d (M)	1.3 x 10^{-6}	R^2	0.607
R^2	0.9743		

Table 3. Isotherm parameters.

Freundlich		Langmuir		Langmuir-Freundlich	
ΔR_{max}	1.870	ΔR_{max}	2.508	ΔRmax	18.018
1/n	0.947	K_a (M^{-1})	7.40 x 10^4	1/n	0.947
R^2	0.996	K_d (M^{-1})	1.35 x 10^{-5}	Ka (M^{-1})	1.40 x 10^4
		R^2	0.958	Kd (M)	7.20 x 10^{-5}
				R^2	0.936

constants were 7.7 x 10^5 M^{-1} and 1.3 x 10^{-6} M. As can be seen, the interactions between the nanosensor and KAN have a high affinity according to the association (K_a) and dissociation (K_d) constants.

Adsorption isotherm models were utilized to examine the surface heterogeneity and binding behaviours of imprinted nanosensors. The binding characteristics were investigated by using the Langmuir and Scatchard models for the imprinted nanosensor (Table 3). The Langmuir model supposes that the surface has homogeneous binding sites with the same binding affinity coefficient. The Freundlich model describes the heterogeneous binding behavior of surfaces. This model is useful for estimating adsorption on the heterogeneous nature of surfaces and thus avoiding the limitation of higher concentration related to the Freundlich model. Therefore, this model has been explained by Freundlich Isotherm at low concentration and the Langmuir model at high concentration.

The Freundlich model was used to match the experimental binding isotherms based on correlation coefficient and linearity data, as shown in Table 3. According to the Freundlich model, Rmax and the Freundlich constant, 1/n, were calculated to be 1.87 and 0.947, respectively. Although the binding sites on the kanamycin imprinted nanosensor are diverse, the population of high-affinity binding sites is greater. Consequently, the Freundlich model is best suited to elucidate the binding behaviors of imprinted polymers.

Selectivity of nanosensor

The response of imprinted and nonimprinted nanosensors towards the chemical analogs of KAN (NEO and SPM) were investigated to prove the selectivity of KAN imprinted nanosensors. The assay for the detection of KAN was separately applied to the chemical analogs solutions onto the imprinted and nonimprinted nanosensor and the sensograms are shown in Figure 6. As seen in Figure 6b, the nonimprinted nanosensor is non-selective and has a poor sensitivity to detect KAN. However, the imprinted nanosensor produces a strong signal with good selectivity for the detection of KAN (Figure 6a). The selectivity results prove that the imprinted nanofilm has specific cavities to recognize the KAN with high sensitivity and selectivity.

Reusability of nanosensor

The reusability performance of imprinted nanosensor was investigated by spiking 25 ng/mL KAN solution with three cycles. As seen in Figure 7, the change in the response of nanosensor after a three-cycle is not significant to detect kanamycin. Consequently, the developed nanosensor system indicates good repeatability to recognize kanamycin in an aqueous solution.

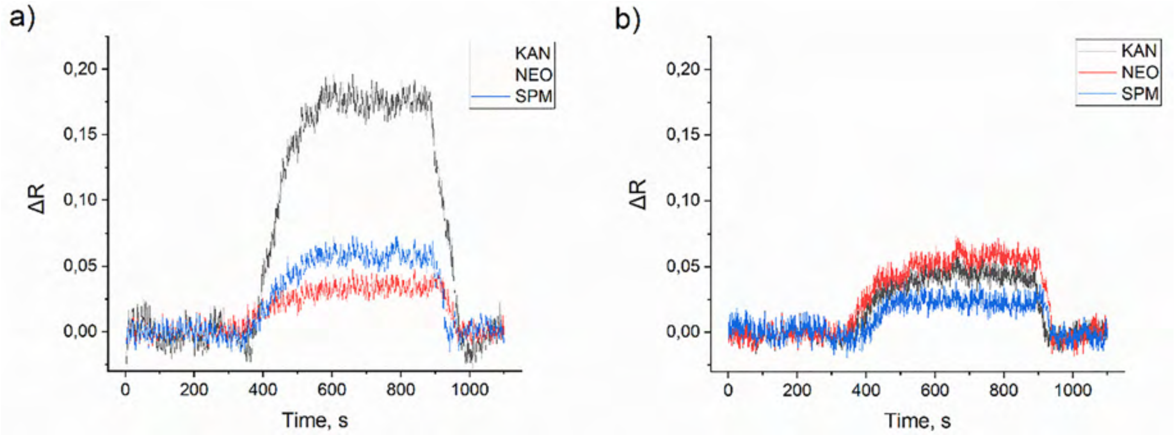

Figure 6. The SPR responses of imprinted (a) and nonimprinted (b) nanosensors for KAN, NEO, and SPM.

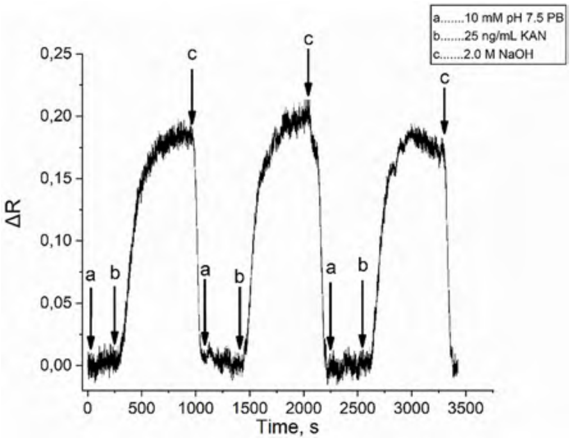

Figure 7. Reusability of the imprinted SPR nanosensor.

CONCLUSION

In this research, the KAN imprinted nanofilm for the SPR sensor was constructed and successfully synthesized by in-situ radical polymerization. Various methodologies were used to characterize the constructed system, and the refractive index changes were analyzed depending on the relation between the KAN concentrations and the signal enhancements. the refractive index changes depending on the relationship between kanamycin concentrations and signal enhancements were analyzed. The responses of imprinted nanosensors were found to be effective for detecting analytes of interest, whereas non-imprinted nanosensor responses were ineffective. For the detection of kanamycin, numerous analytical approaches have been used, including solid-phase extraction (SPE), spectrophotometry, electrochemical, high-performance liquid chromatography (HPLC), mass spectrophotometry (MS), cantilever array sensor, and capillary electrophoresis [3-12]. Such systems, in contrast to the suggested sensing system, are arduous, expensive, time-consuming, and difficult. Based on these findings, the imprinted nanosensors are capable of selectively capturing KAN from aqueous media. The imprinted nanofilms appear to be a promising tool for sensing applications in this area. Based on this successful approach and ease of extension to the analysis of additional analytes, the SPR system in combination with the MIP method is envisioned as a potential technique for detecting residues.

CONFLICT OF INTEREST

There is no financial conflict of interest with any institution, organization, person related to our article named “Selective Recognition of Kanamycin via Molecularly Imprinted Nanosensor” and there is no conflict of interest between the authors.

References

1. Claes PJ, Dubost M, Vanderhaeghe H. Kanamycin sulfate, Analytical Profiles of Drug Substances., New York, pp. 259–296, 1977.
2. Sharma N, Selvam SP, Yun K. Electrochemical detection of amikacin sulphate using reduced graphene oxide and silver nanoparticles nanocomposite. Applied Surface Science 512 (2020) 145742.
3. Xu Y, Han T, Li X, Sun L, Zhang Y, Zhang Y. Colorimetric detection of kanamycin based on analyte-protected silver nanoparticles and aptamer-selective sensing mechanism. Analytica Chimica Acta 891 (2015) 298-303.
4. Rahman M M. Chemical, Label-free Kanamycin sensor development based on CuONiO hollow-spheres: food samples analyses. Sensors and Actuators B: Chemical 264 (2018) 84-91.
5. Bai X, Hou H, Zhang B, Tang J. Label-free detection of kanamycin using aptamer-based cantilever array sensor. Biosensors and Bioelectronics 56 (2014) 112-116.
6. Wang R, Wang R, Ge B, Jia X, Li Z, Chang J. Spectral method determination of kanamycin sulfate using both gold nanoparticles and quantum dots. Analytical Methods 19 (2013) 5302-5308.
7. Long F, Zhang Z, Yang Z, Zeng J, Jiang Y. Imprinted electrochemical sensor based on magnetic multi-walled carbon nanotube for sensitive determination of kanamycin. Journal of Electroanalytical Chemistry 755 (2015) 7-14.
8. Adams E, Dalle J, De Bie E, De Smedt I, Roets E, Hoogmartens J. Analysis of kanamycin sulfate by liquid chromatography with

pulsed electrochemical detection. Journal of Chromatography A 766 (1997) 133-139.

9. Tao Y, Chen D, Yu H, Huang L, Liu Z, Cao X, Yan C, Pan Y, Liu Z, Yuan Z. Simultaneous determination of 15 aminoglycoside (s) residues in animal derived foods by automated solid-phase extraction and liquid chromatography–tandem mass spectrometry. Food Chemistry 135 (2012) 676-683.
10. Song HY, Kang TF, Li NN, Lu LP, Cheng SY. Highly sensitive voltammetric determination of kanamycin based on aptamer sensor for signal amplification. Analytical Methods 16 (2016) 3366-3372.
11. Lin YF, Wang YC, Chang SY. Capillary electrophoresis of aminoglycosides with argon-ion laser-induced fluorescence detection. Journal of Chromatography A 1188 (2008) 331-333.
12. Kaale E, Van Schepdael A, Roets E, Hoogmartens J. Development and validation of a simple capillary zone electrophoresis method for the analysis of kanamycin sulfate with UV detection after pre-capillary derivatization. Journal of Chromatography A 924 (2001) 451-458.
13. Arabi M, Ostovan A, Li J, Wang X, Zhang Z, Choo J, Chen L. Molecular imprinting: green perspectives and strategies. Advanced Materials 33 (2021) 2100543.
14. Mosbach K. Molecular imprinting. Trends in biochemical sciences 19 (1994) 9-14.
15. Mosbach K, Ramström O. The emerging technique of molecular imprinting and its future impact on biotechnology. Bio/technology 14 (1996) 163-170.
16. Wulff G. Molecular imprinting in cross-linked materials with the aid of molecular templates—a way towards artificial antibodies. Angewandte Chemie International Edition in English 34 (1995) 1812-1832.
17. He S, Zhang L, Bai S, Yang H, Cui Z, Zhang X, Li Y. Advances of molecularly imprinted polymers (MIP) and the application in drug delivery. European Polymer Journal 143 (2021) 110179.
18. Piletsky SS, Piletska E, Poblocka M, Macip S, Jones DJL, Braga M, Cao TH, Singh R, Spivey AC, Aboagye EO, Piletsky SA. Snapshot imprinting: rapid identification of cancer cell surface proteins and epitopes using molecularly imprinted polymers. Nano Today 41 (2021) 101304.
19. Zhang J, Wang Y, Lu X. Molecular imprinting technology for sensing foodborne pathogenic bacteria. Analytical and Bioanalytical Chemistry 413 (2021) 4581-4598.
20. Balayan S, Chauhan N, Chandra R, Jain U. Molecular imprinting based electrochemical biosensor for identification of serum amyloid A (SAA), a neonatal sepsis biomarker. International Journal of Biological Macromolecules 195 (2022) 589-597.
21. Perez-Puyana V, Wieringa P, Guerrero A, Romero A, Moroni L. (Macro) Molecular Imprinting of Proteins on PCL Electrospun Scaffolds. ACS Applied Materials & Interfaces 13.25 (2021) 29293-29302.
22. Bonatti AF, De Maria C, Vozzi G. Molecular imprinting strategies for tissue engineering applications: A review. Polymers 13 (2021) 548.
23. Cennamo N, D'Agostino G, Pesavento M, Zeni L. High selectivity and sensitivity sensor based on MIP and SPR in tapered plastic optical fibers for the detection of L-nicotine. Sensors and Actuators B: Chemical 191 (2014) 529-536.
24. Matsui J, Akamatsu K, Hara N, Miyoshi D, Nawafune H, Tamaki K, Sugimoto N. SPR sensor chip for detection of small molecules using molecularly imprinted polymer with embedded gold nanoparticles. Analytical Chemistry 77 (2005) 4282-4285.
25. Shrivastav AM, Mishra SK, Gupta BD. Fiber optic SPR sensor for the detection of melamine using molecular imprinting. Sensors and Actuators B: Chemical 212 (2015) 404-410.
26. Meneghello A, Sonato A, Ruffato G, Zacco G, Romanato F. A novel high sensitive surface plasmon resonance Legionella pneumophila sensing platform. Sensors and Actuators B: Chemical 250 (2017) 351-355.
27. Bognár Z, Supala E, Yarman A, Zhang X, Bier FF, Scheller FW, Gyurcsányi RE. Peptide epitope-imprinted polymer microarrays for selective protein recognition. Application for SARS-CoV-2 RBD protein. Chemical Science 13 (2022) 1263-1269.
28. Sinha RK. Wavelength modulation based surface plasmon resonance sensor for detection of cardiac marker proteins troponin I and troponin T. Sensors and Actuators A: Physical 332 (2021) 113104.
29. Jagirani MS, Mahesar SA, Uddin S, Sherazi STH, Kori AH, Lakho SA, Kalwar NH, Memon SS. Functionalized Gold Nanoparticles Based Optical, Surface Plasmon Resonance-Based Sensor for the Direct Determination of Mitoxantrone Anti-cancer Agent from Real Samples. Journal of Cluster Science 33 (2022) 241-247.
30. Wang W, Wang R, Liao M, Kidd MT, Li Y. Rapid detection of enrofloxacin using a localized surface plasmon resonance sensor based on polydopamine molecular imprinted recognition polymer. Journal of Food Measurement and Characterization 15 (2021) 3376-3386.
31. Écija-Arenas Á, Kirchner EM, Hirsch T, Fernández-Romero, JM. Development of an aptamer-based SPR-biosensor for the determination of kanamycin residues in foods. Analytica Chimica Acta 1169 (2021) 338631.
32. Zhang L, Zhu C, Chen C, Zhu S, Zhou J, Wang M, Shang P. Determination of kanamycin using a molecularly imprinted SPR sensor. Food chemistry 266 (2018) 170-174.
33. Song KM, Cho M, Jo H, Min K, Jeon SH, Kim T, Ban C. Gold nanoparticle-based colorimetric detection of kanamycin using a DNA aptamer. Analytical biochemistry 415 (2011) 175-181.
34. Zhu Y, Li W, Tan S, Chen TA. A label-free and functional fluorescent oligonucleotide probe based on a G-quadruplex molecular beacon for the detection of kanamycin. Chemical Research in Chinese Universities 34 (2018) 541-545.
35. Li F, Wang X, Sun X, Guo Y. An aptasensor with dsDNA for rapid and highly sensitive detection of kanamycin in milk. RSC advances 7 (2017) 38981-38988.
36. Lai C, Liu X, Qin L, Zhang C, Zeng G, Huang D, Huang D. Chitosan-wrapped gold nanoparticles for hydrogen-bonding recognition and colorimetric determination of the antibiotic kanamycin. Microchimica Acta 184 (2017) 2097-2105.
37. Sari E, Üzek R, Duman M, Denizli A. Detection of ciprofloxacin through surface plasmon resonance nanosensor with specific recognition sites. Journal of Biomaterials science, Polymer edition, 29 (2018) 1302-1318.
38. Sari E, Üzek R, Duman M, Denizli A. Fabrication of surface plasmon resonance nanosensor for the selective determination of erythromycin via molecular imprinted nanoparticles. Talanta 150 (2016) 607-614.
39. Sari E, Üzek R, Duman M, Alagöz HY, Denizli A. Prism coupler-based sensor system for simultaneous screening of synthetic glucocorticosteroid as doping control agent. Sensors and Actuators B: Chemical 260 (2018) 432-444.

Hittite Journal of Science and Engineering, 2022, 9 (1) 09–18
ISSN NUMBER: 2148–4171
DOI: 10.17350/HJSE19030000250

Diagnosing Diabetes with Machine Learning Techniques

Omer Faruk Akmese
Hitit University, Department of Computer Engineering, Corum, Turkey

Article History:
Received: 2021/09/12
Accepted: 2022/01/10
Online: 2022/03/30

***Correspondence to**: Ömer Faruk AKMEŞE, E-mail: ofarukakmese@hitit.edu.tr; Phone: +90 364 227 4533;*
Fax: +90 364 227 4535

ABSTRACT

The rate of diabetes is rapidly increasing worldwide. Early detection of diabetes can help prevent or delay the onset of diabetes by initiating lifestyle changes and taking appropriate preventive measures. Prediabetes and type 2 diabetes have proved to be early detection problems. There is a need for easy, rapid, and accurate diagnostic tools for the early diagnosis of diabetes in this context. Machine learning algorithms can help diagnose diseases early. Numerous studies are being conducted to improve the speed, performance, reliability, and accuracy of diagnosing with these methods for a particular disease. This study aims to predict whether a patient has diabetes based on diagnostic measurements in a dataset from the National Institute of Diabetes and Digestive and Kidney Diseases. Eight different variables belonging to the patients were selected as the input variable, and it was estimated whether the patient had diabetes or not. Of the 768 records examined, 500 (65.1%) were healthy, and 268 (34.9%) had diabetes. Ten different machine learning algorithms have been applied to predict diabetic status. The most successful method was the Random Forest algorithm with 90.1% accuracy. Accuracy percentages of other algorithms are also between 89% and 81%. This study describes a highly accurate machine learning prediction tool for finding patients with diabetes. The model identified in the study may be helpful for early diabetes diagnosis.

Keywords:
Diabetes; Diagnosis; Machine learning; Classification; Prediction

INTRODUCTION

Diabetes is a lifelong illness that occurs when the pancreas secretory gland does not produce sufficient hormone insulin levels or when the hormone insulin it produces cannot be used effectively. The patient cannot efficiently use the glucose that has been taken from the foods they have eaten, and as a result, the blood sugar level increases [1]. The chronic hyperglycemia of diabetes is associated with critical complications such as long-term damage, dysfunction and failure of the eyes, kidneys, nerves, heart and blood vessels and other different organs [2]. Failure to regularly intervene to maintain blood glucose levels at normal levels can cause many problems. Early diagnosis of diabetes is extremely important for effective treatments. However, some patients are unaware of their condition until complications occur [3]. There are three types of diabetes: type I diabetes, type II diabetes, and gestational diabetes [4]. Insulin-dependent Diabetes Mellitus (IDDM), which requires the injection of insulin to the patient as a result of the human body's inability to produce enough insulin, is classified as type I. Type II, which occurs when body cells cannot use insulin properly, is known as Non-Insulin Dependent Diabetes Mellitus (NIDDM). Type III Gestational Diabetes occurs with increased blood sugar in pregnant women where diabetes is not detected earlier [5]. Type 2 diabetes accounts for about 90% of cases of diabetes. The most common type 2 diabetes is considered a "silent disease," and disease indications may not be noticed for many years [6]. Obesity is considered the main cause of Type 2 diabetes in people genetically predisposed to the disease [7]. Early diagnosis and lifestyle changes or medical interventions can help prevent type 2 diabetes in many high-risk individuals [8]–[10]. For this reason, early diagnosis of diabetes is a crucial step to taking the necessary precautions.

Along with the increase in the world population, the number of patients with diabetes is increasing significantly. The main causes of increased diabetes are malnutrition, overweight, ageing, ease of transportation, inactivity, introducing computers into everyday life, the Internet, smartphones, tablets, and constant stress in business life. In the world, 450 million people are fighting against diabetes [11]. In Turkey, there are over 10 million diabetics. Diabetic patients in Turkey is almost two times the world average in terms of population. Turkey is the country with the fastest increase in diabetes in Europe. According to data from 2015, in Turkey, it is stated that one out of every six people is fighting against diabetes [11]. A large amount of money is spent on treating diabetes mellitus, seen in a wide variety. In addition, the treatment process requires severe care and work.

Data mining techniques are preferred in all areas, as computers' data processing and computing capacities increase rapidly. Health is one of the areas that makes the most use of its support in the diagnosis and treatment process. Medical diagnosis is a complex and important process requiring actual patient data, accurate medical literature knowledge, and clinical experience. The medical diagnosis process is much more complicated than the identification processes in other sectors because it includes many unexpected situations. Clinical decisions are often made based on physicians' perceptions and experiences [12]. However, patients may not always express their complaints correctly. The rapid increase in the amount of data also causes difficulties in decision making.

Data mining and machine learning techniques are widely used in diabetes studies [5], [13]–[22]. The number of studies that predict disease diagnosis with machine learning is increasing. Researchers for the diagnosis of diabetes conduct many studies. Sowjanya et al. [23]: developed an android-based application to raise awareness of diabetes. In application, machine learning techniques have been used to predict diabetes among users. The system also provides information about diabetes and some suggestions about the disease. Orabi et al. [24] designed a system for estimating diabetes. While the proposed system achieved high accuracy using the decision tree algorithm, the results were satisfactory. Nongyao et al. [25], in their study "Comparison of Classifiers for the Risk of Diabetes Prediction Diabetes Mellitus," applied an algorithm that classifies the risk of diabetes mellitus. The model is designed with Decision Tree, Artificial Neural Networks, Logistic Regression, Random Forest, and Naive Bayes algorithms. Findings show that the best performance of the disease risk classification is the Random Forest algorithm. According to Humar et al. [26] proposed a hybrid Neural Network System with Artificial Neural Network and Fuzzy Neural Network with 79.16% accuracy for Diabetes diagnosis. Mohammed et al. [27] proposed SVR, a hybrid method with the NSGA-II method, for diabetes detection and achieved 86.13% accuracy. Mujumdar and Vaidehi [5] achieved 98.8% accuracy using the AdaBoost classifier in their study. Faruque et al. [19], with the C4.5 decision tree, achieved an accuracy of 73.5% to predict diabetes. On the other hand, Sonar and Jaya Malini [19] achieved an accuracy of 85% with the Decision Tree in their research. Zou et al. [28] showed that the accuracy of diabetes prediction could be 80.8% with random forest. In their study, Kaur and Kumari [21] achieved the best 89% accuracy for diabetes prediction with the SVM-linear model. Acar et al. achieved a performance of 87.06% with the LS-SVM method in their study in which they presented the estimation of diabetes mellitus with biometric measurements [29].

Clinical records of the National Institute of Diabetes and Digestive and Kidney Diseases were used in this study. Vincent Sigillito of Johns Hopkins University is the database donor. These data include age, pregnancies, glucose, blood pressure, skin thickness, insulin, body mass index, and diabetes lineage function variables associated with diabetes in women with suspected diabetes. This study aimed to create an effective predictive model with high sensitivity and selectivity to better identify patients at risk for diabetes based on patient measurements. In the study, patients with diabetes were tried to be determined with ten machine learning algorithms. These are, in order of accuracy: Random Forest, Gradient Boosting, XGB, LGBM, Decision Tree, AdaBoost, Support Vector Machine, Logistic Regression, kNN, Naive Bayes algorithms. Accuracy percentages and experimental performances of all algorithms were compared. Compared to the previous ones, this study is a more comprehensive study that includes many algorithms used in diabetes diagnosis, aiming to compare their performance and find the best among them.

EXPLORATORY DATA ANALYSIS

The approach to analyzing datasets using visual methods to summarise their key features and seeing what the data can say beyond the task of modelling or hypothesis testing is often called Exploratory Data Analysis (EDA) [30]. EDA aims to perform initial investigations on data before formal modelling and graphical representations and visualizations to discover patterns, review assumptions, and test hypotheses. Data visualizations contain explanatory and comparative charts to effectively illustrate abstract and concrete ideas. Summary information about key features and hidden trends in data can help identify problems, and their resolution can improve accuracy in diagnosing diabetes.

Understanding and Visualizing Data

In this study, the diabetes dataset in Kaggle was used to model and test the proposed method [31]. The selected

Table 1. Dataset description

Name	Type	Description	Role
Outcome	Categorical	0(no diabetes) / 1(diabetes)	Target
Pregnancies	Numerical	Number of times pregnant	Input
Glucose	Numerical	Plasma glucose concentration is an oral glucose tolerance test.	Input
BloodPressure	Numerical	Diastolic blood pressure (mm Hg)	Input
SkinThickness	Numerical	Triceps skin fold thickness (mm)	Input
Insulin	Numerical	2-Hour serum insulin (mu U/ml)	Input
BMI	Numerical	Body mass index	Input
DiabetesPedigree Function	Numerical	Diabetes pedigree function	Input
Age	Numerical	Age (years)	Input

Categorical: Data that can be grouped and cannot be expressed numerically. Numerical: Data expressed as numbers, not letters or words that cannot be grouped. Target: Estimated output variable Input: Attribute, predictor, feature

dataset is part of a larger dataset maintained by the National Institutes of Diabetes and Digestive and Kidney Diseases. This data set has been used by many researchers in predictive analyses [14], [17], [21], [22], [28]. The dataset consists of data used for diabetes research on women of Pima Indian heritage, aged 21 and over, living in Phoenix, the 5th largest city of the State of Arizona in the USA. The data set consists of 768 observations and eight independent numerical variables. The target variable is specified as "result"; 1 indicates positive diabetes test result, 0 indicates negative. The name of the data, the data type definition, and its role are shown in Table 1.

Table 2 shows summary statistics, including measures of central tendency such as mean and median and measures of distribution such as standard deviation, which are useful in providing a quick and simple description of the dataset and its characteristics. Pregnancies appear in a realistic range from 0 to 17. Some other attributes in the data (Glucose, BloodPressure, SkinThickness, Insulin, BMI) include the value 0, which is not possible in practice. In this case, the impossible 0 values need to be corrected. All impossible values were corrected by replacing them with mean values at the pre-processing stage. The 'DiabetesPedigreeFunction' is a function that scores the probability of diabetes based on family history, with a realistic range of 0.08 to 2.42. Age has a realistic range from 21 to 81. The Outcome, in the target variable, 0 represents healthy people, and 1 represents those with diabetes.

Table 2. Basic descriptive statistics

	Count	Mean	Std	Min	25%	50%	75%	Max
Pregnancies	768	3.85	3.37	0	1	3	6	17
Glucose	768	120.89	31.98	0	99	117	140.25	199
BloodPressure	768	69.10	19.36	0	62	72	80	122
SkinThickness	768	20.54	15.95	0	0	23	32	99
Insulin	768	79.79	115.24	0	0	30.5	127.25	846
BMI	768	31.99	7.88	0	27	32.	36.60	67.1
DiabetesPedigree Function	768	0.47	0.33	0.078	0	0.37	0.62	2.42
Age	768	33.24	11.76	21	24	29	41	81
Outcome	768	0.34	0.47	0	0	0	1	1

Count: Number of values in the dataset. Mean: The average of values. Std: The standard deviation of values. Min: The smallest value. 25%: The value at the 25% percentile. 50%: The value at the 50% percentile. 75%: The value at the 75% percentile. Max: The largest value.

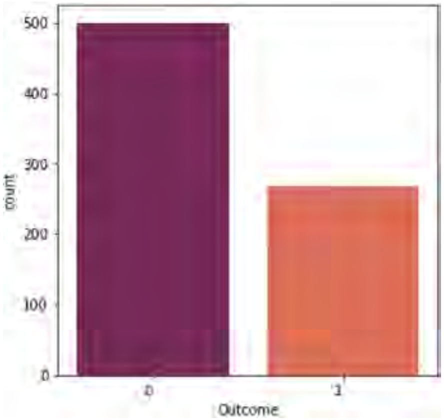

Figure 1. Count of diabetes Outcome.

The visual representation of quantitative data for communication and analysis is called data visualization [32]. With the increase in data types and diversity, there is a need for more analysis and presentation types that reveal the relationships between variables and summarise complex data with simple and easy-to-understand visuals [33]–[35]. Visualization of data is often performed without a model or hypothesis testing. Analysts can quickly and easily identify patterns, trends, and outliers from charts and charts [35]. The following visualizations were made in the data set to summarise complex data with simple and understandable visuals, reveal the relationships between variables, and identify patterns, trends, and outliers. Of the 768 clinical records analyzed according to Fig. 1, 500 (65.1%) were healthy, and 268 (34.9%) had diabetes.

Heatmaps can be used to cross-examine multivariate data, show variance between variables, show whether any variables are similar to each other, and detect whether there is a correlation between variables. Fig. 2 shows the heatmap

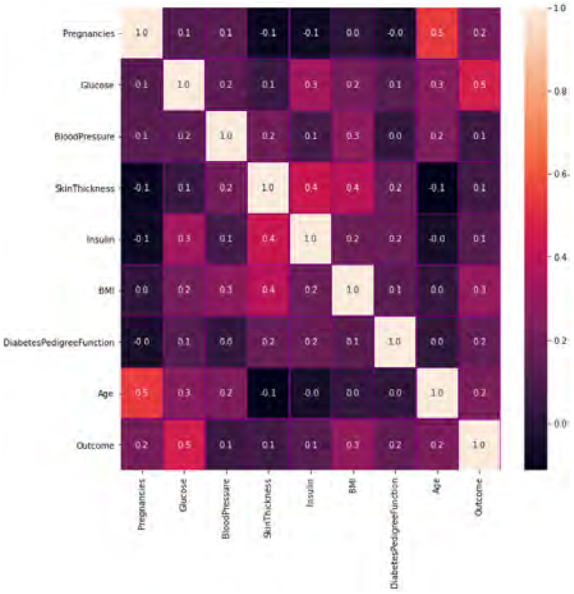

Figure 2. Heatmap

of the attributes in the data set. Accordingly, almost all attributes have weak linear correlations. This indicates that most variables are more likely to have nonlinear relationships.

To obtain accurate predictions in classification, mostly focused on the relationship between diabetes features in the dataset and the target feature resulting from diabetes. For example, when Glucose and BMI increase by 1 unit according to the heatmap, the positive Outcome of diabetes increases by 0.5 units and 0.3 units, respectively. The graph shows cases where diabetes patients generally have a higher number of Glucose, BMI, Age, Pregnancies and DiabetesPedigreeFunction. Glucose is the best indicator of diabetes outcome in this situation. It is seen that with strongly correlated features, the target class can be predicted more easily, and more meaningful results can be drawn.

MATERIALS AND METHODS

In the study, exploratory data analysis was performed to understand the data better. The dataset was pre-processed to provide reliable and acceptable results for estimating diabetes classifications. The modelling process was analyzed and evaluated with various classifier models, accuracy, precision, recall, and F1 score performance metrics. Data analysis in the research was carried out using the Python (3.8) programming language.

Pre-processing

Before analysis, pre-processing consists of steps to transform the raw data into a clean and organized dataset. Databases can have many quality control issues. Pre-processing aims to evaluate and improve data quality to allow reliable analysis [36]. Preprocessing refers to the transformations applied to the data before analysis. In this process, raw data is converted into an understandable dataset. Various techniques such as min-max, variance, deviation, standardization, mean scaling and elimination of missing values in the data set were applied in the pre-processing process [37]. In addition, outliers were also removed from the dataset.

In the pre-processing stage, it was observed that some records of the attributes in the data set contain the '0' value, which is not possible, some records contain outliers, and some records have missing values. Data containing missing, outlier and not possible value '0' were replaced with mean values. Thus, a data set without other noises with impossible values was obtained.

Feature Engineering

Feature engineering is the task of improving predictive modelling performance by transforming the feature space in a dataset. [38]. They are methods that enable to extraction of new features for machine learning models from raw data. Thus, better results can be obtained in terms of model performance. Feature engineering either changes the form of the variables in the data set or generates new and different variables in a machine learning process. Feature engineering was used in the study to improve the analyzability of the dataset further. In addition to generating new variables, the form of the variables has also been changed with the One-Hot Encoding and Robust Scaler methods. In this study, while nine variables were included in the original data set, the number of variables resulted in 17 with feature extraction.

Table 3 contains a cross-section showing the first five records of the data set. In addition to the new variables produced by feature extraction, it is seen that the form of the variables in the data set has changed. As such, the data is ready for analysis.

The architecture of the proposed model

The data set was estimated by algorithms of Random Forest, Gradient Boosting, XGB, LGBM, Decision Tree, AdaBoost, Support Vector Machine, Logistic Regression, kNN and Naive Bayes algorithms. The reason for choosing these algorithms was that they are widely used in the literature and give relatively better results in the existing data set.

Random Forest

Random forest algorithm is based on combining Decision trees and Bagging methods and falls under Ensemble methods [39]. Random forest is a flexible machine learning method used for regression or classification problems. In its simplest form, a random forest combines a large number of generated decision trees to obtain a more accurate prediction.

Table 3. Samples of the dataset

	0	1	2	3	4
Pregnancies	0.600	-0.400	1.000	-0.400	-0.600
Glucose	0.765	-0.790	1.630	-0.691	0.494
BloodPressure	0.000	-0.375	-0.500	-0.375	-2.000
SkinThickness	1.000	0.143	0.571	-0.714	1.000
Insulin	1.000	0.000	1.000	-0.127	0.978
BMI	0.170	-0.599	-0.962	-0.434	1.214
DiabetesPedigreeFunction	0.230	-0.019	0.271	-0.186	0.749
Age	1.235	0.118	0.176	-0.471	0.235
Outcome	1.000	0.000	1.000	0.000	1.000
New_Glucose_Class_ Prediabetes	1.000	0.000	1.000	0.000	0.000
New_BMI_Range_Healty	0.000	0.000	1.000	0.000	0.000
New_BMI_Range_ Overweight	0.000	1.000	0.000	1.000	0.000
New_BMI_Range_Obese	1.000	0.000	0.000	0.000	1.000
New_BloodPressure_HS1	0.000	0.000	0.000	0.000	0.000
New_BloodPressure_HS2	0.000	0.000	0.000	0.000	0.000
New_SkinThickness_1	0.000	0.000	0.000	0.000	0.000
NewInsulinScore_1	0.000	1.000	0.000	1.000	0.000

Gradient Boosting

Gradient Boosting is a powerful machine learning technique used for regression or classification problems, one of the ensemble methods. Each tree is grown using information from previously grown trees. The basic idea is to minimize the error and determine the target outputs for the next model. This technique relies on the progress of subsequent forecasts by learning from previous forecast errors [40].

XGB

The XGB (eXtreme Gradient Boosting) algorithm, which was brought to the literature by Chen and Guestrin, is an effective algorithm that has been frequently used in supervised machine learning applications such as regression and classification [41]. It is an efficient optimization of the gradient boosting technique [42]. It uses an approach to find the best decision tree model to achieve higher speed and better performance. XGBoost is one of the most successful machine learning algorithms [43].

LGBM

It is a machine learning algorithm with a decision tree approach that emerged late 2017 [44]. The algorithm released by Microsoft has the advantages of low memory consumption and providing high accuracy. LGBM is an optimized ensemble learning algorithm based on the Gradient Boosted Decision Tree. This model uses a histogram-based algorithm on high-dimensional data to speed up the computation time and avoid overloading the prediction system [45], [46].

Decision Tree

Decision Trees are a type of supervised machine learning where data is continuously divided according to a certain parameter. A decision tree is a method used to divide a data set into smaller clusters by applying rules. In other words, it is based on the principle of dividing large amounts of data into smaller data groups [47]. The decision tree contains the concepts of nodes and leaves. Nodes represent where data is divided, and leaves represent decisions. The tree structure used is easy to understand and interpret as it can be visualized.

AdaBoost

AdaBoost is a machine learning approach that combines many relatively weak and erroneous rules to create an accurate prediction rule. Freund and Schapire's AdaBoost algorithm was the first practical boosting algorithm and remained one of the most widely used. [48]. The AdaBoost algorithm produces strong classifiers with weak classifiers. In each cycle, the weights are adjusted, and a committee of weak classifiers is formed. While the weights of the training samples incorrectly classified by the existing weak classifier are increased, the weights of the correctly classified training samples are decreased. The AdaBoost algorithm has good performance due to generating expanding diversity [49].

Support Vector Machine

SVM (Support Vector Machine) is one of the machine learning methods used for classification. The high accuracy of SVM, which is widely used in classification problems, has made this method widespread. This method differs because the number of operations and algorithm complexity is low. SVM is divided into two as linear or nonlinear [50]. The algorithm proposed by Vapnik in 1963 was a linear classifier model [51]. However, in 1992 Bernhard E. Boser, Isabelle M. Guyon, and Vladimir N. Vapnik proposed a way to construct nonlinear classifiers [52]. In linear cases, there is a separation of classes with the help of a decision function obtained from the training data. The line that divides the data set into two is called the decision line. The main purpose of this model is to determine the hyperplane that will best separate the classes from each other. In the case of a nonlinear dataset, the kernel method is used because SVMs cannot draw a linear hyperplane. The kernel method greatly increases the classification accuracy for nonlinear data.

Logistic Regression

Logistic regression is a statistical method used to analyze a data set that determines an outcome and has independent variables. Although it is called regression, there is a classification here. Recently, logistic regression has come to the forefront and has become an intensively used method due to its ease of use and interpretation of numerical data. It is generally used in medicine, biology, and economics [53].

kNN

kNN (K Nearest Neighbor) is one of the machine learning methods used for classification. The k value determines the number of elements in the classification. It searches for the nearest neighbours in the dataset while estimating. Euclidean, Manhattan, Minkowski and Hamming functions can be used in distance calculations [40].

Naive Bayes

The Naive Bayes algorithm is a supervised learning algorithm based on Bayes' theorem, used in solving classification problems. Naive Bayes classification assumes that the variables are independent of the classes. It is a probabilistic classifier; that is, it makes predictions based on the probability of an object. The Naive Bayes Classifier is a simple and effective classification algorithm that can make fast predictions that help build fast machine learning models. The traditional Naive Bayes classifier is still widely used as a popular learning algorithm for data mining applications due to its simplicity [54]–[56].

Table 4 lists the parameters used in ten machine learning techniques.

In the study, calculations were made using hold-out and cross-validation methods. Similar results were obtained in both methods. Since the data set is large enough, the hold-out method, which is faster and requires less computational power, was preferred. Some of the data (75%) were used in training the model and some of it (25%) in testing. The proposed method is shown in Fig. 1.

Table 4. Parameters in algorithms

No	Algorithm	Parameters
1	Random Forest	{'criterion': 'gini', 'n_estimators': 100, 'max_depth': 10}
2	Gradient Boosting	{'criterion': 'friedman_mse', 'learning_rate': 0.1, 'max_depth': 3, 'n_estimators': 100, 'subsample': 1.0 }
3	XGB	{'booster': 'gbtree', 'learning_rate': 0.3, 'max_depth': 6, 'n_estimators': 100}
4	LGBM	{'boosting_type': 'gbdt', 'learning_rate': 0.1, 'max_depth': -1, 'n_estimators': 100, 'subsample': 1.0}
5	Decision Tree	{'criterion': 'gini', 'max_depth': 10, 'min_samples_leaf': 1, 'min_samples_split': 2, }
6	AdaBoost	{'learning_rate': 1, 'n_estimators': 100, }
7	SVM	{'C': 1.0, 'cache_size': 200, 'coefo': 0.0, 'kernel': 'rbf', 'max_iter': -1}
8	Logistic Regression	{'C': 1.0, 'max_iter': 1000, 'tol': 0.0001}
9	kNN	{'leaf_size': 30, 'metric': 'minkowski', 'n_neighbors': 5}
10	Naive Bayes	{'var_smoothing': 1e-09}

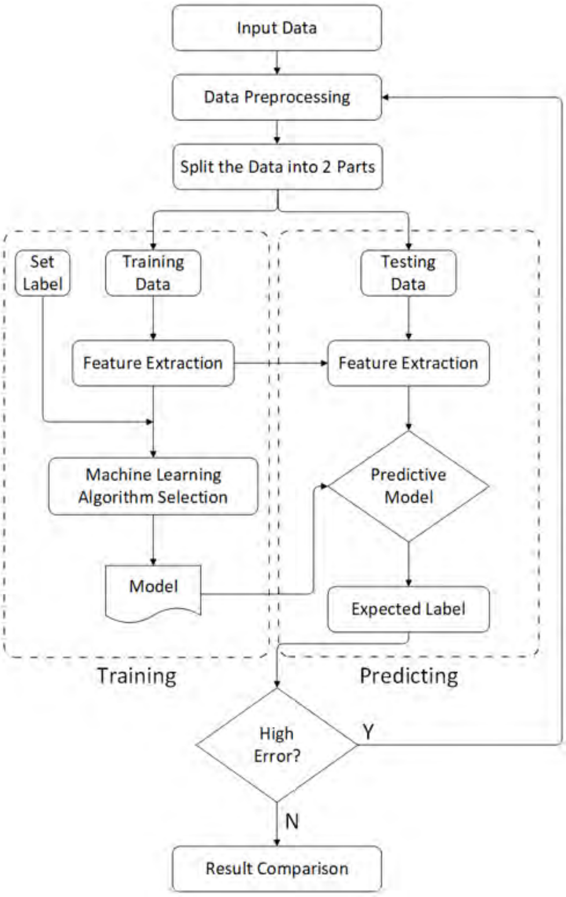

Figure 3. The proposed model

According to the architecture shown in Fig. 3, the collected data are subjected to pre-processing by the researchers. The fact that the quality of the data greatly influences the prediction result means that pre-processing plays an important role in the model [24].

Measurement

The following metrics were used to measure classification performance [57]. (TP: true positives, TN: true negatives, FN: false negatives, FP: false positives.)

Accuracy: Expresses the total accuracy rate.

$$\text{Accuracy} = \frac{TP + TN}{TP + FP + TN + FN} = \frac{TP + TN}{P + N}$$

AUC: The AUC value measures the accuracy of a diagnostic test. It is calculated according to the area under the ROC curve.

Precision: It expresses the ratio of correctly detected Positive classes to all positives.

$$\text{Precision} = \frac{TP}{TP + FP} = \frac{TP}{P'}$$

Recall: It expresses the ratio of correctly detected Positive classes to true positives.

$$\text{Recall} = \frac{TP}{TP + FN} = \frac{TP}{P}$$

F1-score: The F1-score is the harmonic mean of the sensitivity and precision.

$$\text{F1-score} = \frac{2 \cdot \text{Precision} \cdot \text{Recall}}{\text{Precision} + \text{Recall}}$$

RESULT AND DISCUSSION

Table 5 shows the results of the ten machine learning methods used in the study. Accordingly, the Random Forest algorithm is the most accurate conclusion.

Table 4 shows the Accuracy percentage, F1, Precision and Recall values of each model. Also, the most successful method according to the percentage of accuracy is found as Random Forest. In the algorithms selected according to Table 6, the complexity matrix is seen for the Random Forest method. This method gives the most accurate result with 90.1%.

According to Table 6, the model correctly predicted those with diabetes to be 90.1%. The rate of healthy people defined as ill (Type I error) was 11.8%, while the proportion of patients diagnosed as healthy (Type II error) was 9.2%.

Table 5. Accuracy values of models using data set

Method	Accuracy (%)	F1	Precision	Recall
Random Forest	90.1	0.90	0.90	0.90
Gradient Boosting	89.5	0.89	0.90	0.90
XGB	88.5	0.88	0.88	0.89
LGBM	88.5	0.88	0.88	0.89
Decision Tree	86.4	0.87	0.87	0.86
AdaBoost	86.4	0.86	0.86	0.86
Support Vector Machine	86.4	0.86	0.86	0.86
Logistic Regression	85.9	0.86	0.86	0.86
kNN	85.4	0.85	0.85	0.85
Naive Bayes	81.7	0.82	0.83	0.82

Accuracy: Total accuracy rate. F1-score: The F1-score is the harmonic mean of the sensitivity and precision. Precision: Ratio of correctly detected Positive classes to all positives. Recall: Ratio of correctly detected Positive classes to true positives.

Table 6. Results of Random Forest

Accuracy:90.1%	True 1	True 0	Total	Class Precision	
Pred. 1	45 (TP) Correct Decision	6 (FP) Type I error	51 (P')	88.2%	90% (weighted avg)
Pred. 0	13 (FN) Type II error	128 (TN) Correct Decision	141 (N')	90.8%	
Total	58 (P)	134 (N)	192		
Class Recall	77.5%	95.5%			
	90% (weighted avg)				

TP: true positives, TN: true negatives, FN: false negatives, FP: false positives. Precision: Ratio of correctly detected Positive classes to all positives. Recall: Ratio of correctly detected Positive classes to true positives.

The Receiver Operating Characteristic (ROC) curve is expressed as the ratio of sensitivity to specificity. ROC can also be expressed as the fraction of true positives, false positives. The ROC curve provides the opportunity to compare different tests and diagnostic activities of different practitioners, monitor practitioners' development, determine the test's discrimination power, and monitor the quality of the laboratory results [58]. A diagnostic test is useful to the extent that it distinguishes patients well from their health. In the case where the diagnostic test has no separation characteristics, the value of the area under the ROC curve is 0.50. In the case of an excellent diagnostic test, this value should be 1. The test should have a value between these two. The area under the ROC curve is called AUC (Area Under Curve). The larger the AUC value, the better the diagnostic test can discriminate it.

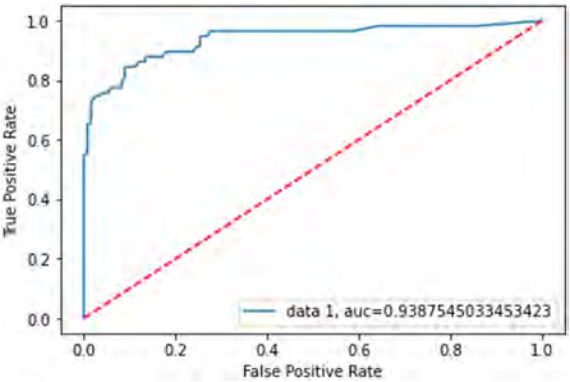

Figure 4. Receiver Operating Characteristic Curve (ROC AUC)

Table 7. Classification accuracies of other classifiers in the literature

	Authors	Year	Method	Best Accuracy
1	Mujumdar and Vaidehi [5]	2019	Logistic Regression	96%
2	Iyer et. al. (2015) [13]	2015	Naive Bayes	79.5%
3	Hasan et. al. [14]	2020	Ensembling AB+XB	95%
4	Meng et. al. [15]	2013	Decision Tree	78%
5	Lai et. al. [16]	2019	GBM	84.7%
6	Sarwar et. al. [17]	2018	SVM and KNN	77%
7	Faruque, et. al. [19]	2019	C4.5 Decision Tree	73.5%
8	Sonar and JayaMalini [20]	2019	Decision Tree	85%
9	Wei et. al. [21]	2018	Deep Neural Network	77.8%
10	Kaur and Kumari [22]	2020	Linear Kernel SVM	89%
11	Nai-arun and Moungmai [25]	2015	Random Forest	85.5%
12	Zangooei et. al. [27]	2014	SVR using NSGA-II	86.1%
13	Zou et. al. [28]	2018	Random Forest	80.8%
14	Acar et. al. [29]	2011	LS-SVM classifier	87.06%
15	Akmeşe (This study)	2022	Random Forest	90.1%

Fig. 4 shows the area under the curve and ROC curve (AUC) for the Random Forest algorithm. The area under the ROC curve is close to 1. Accordingly, it can be said that the analysis is close to perfect distinctiveness.

In Table 7, it is possible to see some studies on diabetes prediction in the literature. Differences in prediction percentages are due to the data set, the algorithms used, and the methodological differences in the studies.

Researchers have made comparative analyses using different machine learning algorithms to evaluate their predictive performance and select the most efficient ones in many studies. In studies reviewed, it is seen that the prediction accuracy is over 80%. However, factors such as the size of the data set and the number of features can significantly affect the algorithm's performance. For this reason, an algorithm with the best performance in a dataset may have a lower prediction accuracy in different data sets [59]. Because diabetes is a disease that can cause many complications, how to predict exactly this disease using Machine learning is worth studying. Early prediction of such diseases can be controlled and save human life. The type of diabetes cannot be predicted from the data set. Therefore, future work may predict the type of diabetes and increase the percentage of accuracy.

CONCLUSION

In this study, machine learning algorithms were used to predict the diagnosis of diabetes. All 768 patients studied were female, and the mean age was also 33 (21-81 years). Of the individuals in the data set, 268 (34.9%) were patients, and 500 (65.1%) were healthy individuals. Ten different machine learning algorithms have been applied to predict diabetic status. The estimation accuracy is considered the most important factor in the study. It has been determined that the Random Forest algorithm achieves the best success rate with a 90.1% correct prediction rate. Accuracy percentages of other algorithms are also between 81% and 89%. New patient data can be added to train the model in future studies. It is thought that a better result can be obtained for estimation as the number of data increases.

CONFLICT OF INTEREST

Authors approve that to the best of their knowledge, there is not any conflict of interest or common interest with an institution/organization or a person that may affect the review process of the paper.

References

1. K. G. M. M. Alberti, P. Zimmet, and J. Shaw, "International Diabetes Federation: A consensus on Type 2 diabetes prevention," Diabet. Med., vol. 24, no. 5, pp. 451-463, 2007, doi: 10.1111/j.1464–5491.2007.02157.x.
2. D. O. F. Diabetes, "Diagnosis and classification of diabetes mellitus," Diabetes Care, vol. 33, no. SUPPL. 1, 2010, doi: 10.2337/dc10–S062.
3. M. Franciosi et al., "Use of the Diabetes Risk Score for Opportunistic Screening of Undiagnosed Diabetes and Impaired Glucose Tolerance: The IGLOO (Impaired Glucose Tolerance and Long–Term Outcomes Observational) study," Diabetes Care, vol. 28, no. 5, pp. 1187-1194, May 2005, doi: 10.2337/diacare.28.5.1187.
4. Z. Tao, A. Shi, and J. Zhao, "Epidemiological Perspectives of Diabetes," Cell Biochem. Biophys., vol. 73, no. 1, pp. 181-185, Sep. 2015, doi: 10.1007/S12013–015–0598–4.
5. A. Mujumdar and V. Vaidehi, "Diabetes Prediction using Machine Learning Algorithms," Procedia Comput. Sci., vol. 165, pp. 292-299, 2019, doi: 10.1016/j.procs.2020.01.047.
6. P. Hossain, B. Kawar, and M. El Nahas, "Obesity and Diabetes in the Developing World — A Growing Challenge," N. Engl. J. Med., vol. 356, no. 3, pp. 213-215, 2007, doi: 10.1056/nejmp068177.
7. F. Mercaldo, V. Nardone, and A. Santone, "Diabetes Mellitus Affected Patients Classification and Diagnosis through Machine Learning Techniques," Procedia Comput. Sci., vol. 112, pp. 2519-2528, 2017, doi: 10.1016/j.procs.2017.08.193.
8. J. Tuomilehto et al., "Prevention of Type 2 Diabetes Mellitus by Changes in Lifestyle among Subjects with Impaired Glucose Tolerance," New England Journal of Medicine, vol. 344, no. 18. pp. 1343-1350, 2001, doi: 10.1056/nejm200105033441801.
9. J. L. Chiasson, R. G. Josse, R. Gomis, M. Hanefeld, A. Karasik, and M. Laakso, "Acarbose for prevention of type 2 diabetes mellitus: the STOP–NIDDM randomized trial," Lancet, vol. 359, no. 9323, pp. 2072-2077, Jun. 2002, doi: 10.1016/S0140–6736(02)08905–5.
10. A. Ramachandran, C. Snehalatha, S. Mary, B. Mukesh, A. D. Bhaskar, and V. Vijay, "The Indian Diabetes Prevention Programme shows that lifestyle modification and metformin prevent type 2 diabetes in Asian Indian subjects with impaired glucose tolerance (IDPP–1)," Diabetologia, vol. 49, no. 2, pp. 289-297, 2006, doi: 10.1007/s00125–005–0097–z.
11. T. Diyabet, V. Başkanı, and P. M. Temel, "DİYABET ORANI 10 YILDA YÜZDE 100 ARTTI," pp. 10-12, 2017.
12. L. Parthiban and R. Subramanian, "Intelligent Heart Disease Prediction System using CANFIS and Genetic Algorithm," Int. J. Biol. Med. Sci., vol. 3, no. 3, pp. 157-160, 2008.
13. A. Iyer, J. S, and R. Sumbaly, "Diagnosis of Diabetes Using Classification Mining Techniques," Int. J. Data Min. Knowl. Manag. Process, vol. 5, no. 1, pp. 01-14, 2015, doi: 10.5121/ijdkp.2015.5101.
14. M. K. Hasan, M. A. Alam, D. Das, E. Hossain, and M. Hasan, "Diabetes prediction using ensembling of different machine learning classifiers," IEEE Access, vol. 8, pp. 76516-76531, 2020, doi: 10.1109/ACCESS.2020.2989857.
15. X. H. Meng, Y. X. Huang, D. P. Rao, Q. Zhang, and Q. Liu, "Comparison of three data mining models for predicting diabetes or prediabetes by risk factors," Kaohsiung J. Med. Sci., vol. 29, no. 2, pp. 93-99, 2013, doi: 10.1016/j.kjms.2012.08.016.
16. H. Lai, H. Huang, K. Keshavjee, A. Guergachi, and X. Gao, "Predictive models for diabetes mellitus using machine learning techniques," BMC Endocr. Disord., vol. 19, no. 1, pp. 1-9, 2019, doi: 10.1186/s12902–019–0436–6.
17. M. A. Sarwar, N. Kamal, W. Hamid, and M. A. Shah, "Prediction of diabetes using machine learning algorithms in healthcare," ICAC 2018 – 2018 24th IEEE Int. Conf. Autom. Comput. Improv. Product. through Autom. Comput., no. September, pp. 6-7, 2018, doi: 10.23919/IConAC.2018.8748992.
18. A. U. Haq et al., "Intelligent machine learning approach for effective recognition of diabetes in e–healthcare using clinical data," Sensors (Switzerland), vol. 20, no. 9, 2020, doi: 10.3390/s20092649.
19. M. F. Faruque, Asaduzzaman, and I. H. Sarker, "Performance Analysis of Machine Learning Techniques to Predict Diabetes Mellitus," 2nd Int. Conf. Electr. Comput. Commun. Eng. ECCE 2019, pp. 7-9, 2019, doi: 10.1109/ECACE.2019.8679365.
20. P. Sonar and K. Jaya Malini, "Diabetes prediction using different machine learning approaches," Proc. 3rd Int. Conf. Comput. Methodol. Commun. ICCMC 2019, no. Iccmc, pp. 367-371, 2019, doi: 10.1109/ICCMC.2019.8819841.
21. S. Wei, X. Zhao, and C. Miao, "A comprehensive exploration to the machine learning techniques for diabetes identification," IEEE World Forum Internet Things, WF–IoT 2018 – Proc., vol. 2018–Janua, pp. 291-295, 2018, doi: 10.1109/WF–IoT.2018.8355130.
22. H. Kaur and V. Kumari, "Predictive modelling and analytics for diabetes using a machine learning approach," Appl. Comput. Informatics, 2019, doi: 10.1016/j.aci.2018.12.004.
23. K. Sowjanya, A. Singhal, and C. Choudhary, "MobDBTest: A machine learning based system for predicting diabetes risk using mobile devices," Souvenir 2015 IEEE Int. Adv. Comput. Conf. IACC 2015, pp. 397-402, 2015, doi: 10.1109/IADCC.2015.7154738.
24. K. M. Orabi, Y. M. Kamal, and T. M. Rabah, "Early predictive system for diabetes mellitus disease," in Lecture Notes in Computer Science (including subseries Lecture Notes in Artificial Intelligence and Lecture Notes in Bioinformatics), 2016, vol. 9728, pp. 420-427, doi: 10.1007/978–3–319–41561–1_31.
25. N. Nai–Arun and R. Moungmai, "Comparison of Classifiers for the Risk of Diabetes Prediction," Procedia Comput. Sci., vol.

69, pp. 132-142, 2015, doi: 10.1016/j.procs.2015.10.014.

26. H. Kahramanli and N. Allahverdi, "Design of a hybrid system for the diabetes and heart diseases," Expert Syst. Appl., vol. 35, no. 1-2, pp. 82-89, 2008, doi: 10.1016/j.eswa.2007.06.004.
27. M. H. Zangooei, J. Habibi, and R. Alizadehsani, "Disease Diagnosis with a hybrid method SVR using NSGA-II," Neurocomputing, vol. 136, pp. 14-29, 2014, doi: 10.1016/j.neucom.2014.01.042.
28. Q. Zou, K. Qu, Y. Luo, D. Yin, Y. Ju, and H. Tang, "Predicting Diabetes Mellitus With Machine Learning Techniques," Front. Genet., vol. 9, no. November, pp. 1-10, 2018, doi: 10.3389/fgene.2018.00515.
29. V. . ACAR, E , ÖZERDEM, M , AKPOLAT, "Forecasting Diabetes Mellitus with Biometric Measurements.," Int. Arch. Med. Res., vol. 1, no. 1, pp. 28-42, 2011.
30. J. Tukey, "Exploratory data analysis," 1977, Accessed: Sep. 08, 2021. [Online]. Available: http://theta.edu.pl/wp-content/uploads/2012/10/exploratorydataanalysis_tukey.pdf.
31. R. S. Smith, J.W., Everhart, J.E., Dickson, W.C., Knowler, W.C., & Johannes, "Pima Indians Diabetes Database," Https://Www.Kaggle.Com/Uciml/Pima-Indians-Diabetes-Database, 2016. https://www.kaggle.com/uciml/pima-indians-diabetes-database (accessed Aug. 01, 2021).
32. "Tufte: The visual display of quantitative information - Google Akademik." https://scholar.google.com/scholar_lookup?title=The Visual Display of Quantitative Information&publication_year=2001&author=E. Tufte (accessed Sep. 08, 2021).
33. S. Lavalle, E. Lesser, R. Shockley, M. S. Hopkins, and N. Kruschwitz, "Big Data , Analytics and the Path From Insights to Value Big Data , Analytics and the Path From Insights to Value," no. 52205, 2011.
34. R. Agrawal, A. Kadadi, X. Dai, and F. Andres, "Challenges and opportunities with big data visualization," 7th Int. ACM Conf. Manag. Comput. Collect. Intell. Digit. Ecosyst. MEDES 2015, pp. 169-173, Oct. 2015, doi: 10.1145/2857218.2857256.
35. S. Nestorov, B. Jukić, N. Jukić, A. Sharma, and S. Rossi, "Generating insights through data preparation, visualization, and analysis: Framework for combining clustering and data visualization techniques for low-cardinality sequential data," Decis. Support Syst., vol. 125, no. March, p. 113119, 2019, doi: 10.1016/j.dss.2019.113119.
36. C. M. Salgado, C. Azevedo, H. Proença, and S. M. Vieira, Setting the Stage: Rationale Behind and Challenges to Health Data Analysis. 2016.
37. S. B. Kotsiantis and D. Kanellopoulos, "Data pre-processing for supervised leaning," Int. J. ;, vol. 1, no. 2, pp. 1-7, 2006, doi: 10.1080/02331931003692557.
38. F. Nargesian, H. Samulowitz, U. Khurana, E. B. Khalil, and D. Turaga, "Learning feature engineering for classification," IJCAI Int. Jt. Conf. Artif. Intell., vol. 0, no. August, pp. 2529-2535, 2017, doi: 10.24963/ijcai.2017/352.
39. L. Breiman, "Random forests," Mach. Learn., vol. 45, no. 1, pp. 5-32, Oct. 2001, doi: 10.1023/A:1010933404324.
40. Ö. F. AKMEŞE, "Karın Ağrısı ile Acil Servise Başvuran Hastalarda Akut Apandisit Tanısı için Makine Öğrenmesi Yaklaşımlarının Kullanımı," Kırıkkale University, 2020.
41. T. Chen and C. Guestrin, "XGBoost: A scalable tree boosting system," Proc. ACM SIGKDD Int. Conf. Knowl. Discov. Data Min., vol. 13-17-August-2016, pp. 785-794, Aug. 2016, doi: 10.1145/2939672.2939785.
42. J. Friedman, "Greedy Function Approximation : A Gradient Boosting Machine Author (s): Jerome H . Friedman Source : The Annals of Statistics , Vol . 29 , No . 5 (Oct ., 2001), pp . 1189-1232 Published by : Institute of Mathematical Statistics Stable URL : http://www," Ann. Stat., vol. 29, no. 5, pp. 1189-1232, 2001.
43. W. Zhao, J. Li, J. Zhao, D. Zhao, J. Lu, and X. Wang, "XGB model: Research on evaporation duct height prediction based on XGBoost algorithm," Radioengineering, vol. 29, no. 1, pp. 81-93, 2020, doi: 10.13164/re.2020.0081.
44. G. Ke et al., "LightGBM: A Highly Efficient Gradient Boosting Decision Tree," Adv. Neural Inf. Process. Syst., vol. 30, 2017, Accessed: Nov. 28, 2021. [Online]. Available: https://github.com/Microsoft/LightGBM.
45. W. Cai, R. Wei, L. Xu, and X. Ding, "A method for modelling greenhouse temperature using gradient boost decision tree," Inf. Process. Agric., Sep. 2021, doi: 10.1016/J.INPA.2021.08.004.
46. M. Massaoudi, S. S. Refaat, I. Chihi, M. Trabelsi, F. S. Oueslati, and H. Abu-Rub, "A novel stacked generalization ensemble-based hybrid LGBM-XGB-MLP model for Short-Term Load Forecasting," Energy, vol. 214, p. 118874, Jan. 2021, doi: 10.1016/J.ENERGY.2020.118874.
47. K. S. Albayrak A., "VERİ MADENCİLİĞİ: KARAR AĞACI ALGORİTMALARI VE İMKB VERiLERİ ÜZERİNE BİR UYGULAMA * DATA MINING: DECISION TREE ALGORITHMS AND AN APPLICATION ON ISE DATA," no. May, 2014.
48. R. E. Schapire, "Explaining AdaBoost," Empir. Inference Festschrift Honor Vladimir N. Vapnik, pp. 37-52, Jan. 2013, doi: 10.1007/978-3-642-41136-6_5.
49. T. K. An and M. H. Kim, "A new Diverse AdaBoost classifier," Proc. - Int. Conf. Artif. Intell. Comput. Intell. AICI 2010, vol. 1, pp. 359-363, 2010, doi: 10.1109/AICI.2010.82.
50. V. Vapnik, The Nature of Statistical Learning Theory. Springer science & business media, 2013.
51. AIZERMAN and M. A., "Theoretical Foundations of the Potential Function Method in Pattern Recognition Learning," Autom. Remote Control, vol. 25, pp. 821-837, 1964, Accessed: Nov. 27, 2021. [Online]. Available: https://ci.nii.ac.jp/naid/10021200712.
52. Boser Berhard E., G. I. M., and V. N. Vapnik, "A training algorithm for optimal margin classifiers," in In Proceedings of the 5th Annual ACM Workshop on Computational Learning Theory, 1992, pp. 144-152.
53. E. Ürük, "İstatistiksel Uygulamalarda Lojistik Regresyon Analizi," Marmara University, 2007.
54. D. Soria, J. M. Garibaldi, F. Ambrogi, E. M. Biganzoli, and I. O. Ellis, "A 'non-parametric' version of the naive Bayes classifier," Knowledge-Based Syst., vol. 24, no. 6, pp. 775-784, Aug. 2011, doi: 10.1016/J.KNOSYS.2011.02.014.
55. "Naive Bayes Classifier in Machine Learning - Javatpoint." https://www.javatpoint.com/machine-learning-naive-bayes-classifier (accessed Nov. 29, 2021).
56. M. Hall, "A Decision Tree-Based Attribute Weighting Filter for Naive Bayes," Res. Dev. Intell. Syst. XXIII - Proc. AI 2006, 26th SGAI Int. Conf. Innov. Tech. Appl. Artif. Intell., pp. 59-70, Dec. 2006, doi: 10.1007/978-1-84628-663-6_5.
57. Gorunescu Florin, Data Mining: Concepts, Models and Techniques. Berlin: Springer Science & Business Media, 2011.

58. A. Dirican, “Tanı Testi Performanslarının Değerlendirilmesi ve Kıyaslanması,” Cerrahpaşa Tip Dergisi, vol. 32, no. 1, pp. 25-30, 2001.
59. I. Kavakiotis, O. Tsave, A. Salifoglou, N. Maglaveras, I. Vlahavas, and I. Chouvarda, "Machine Learning and Data Mining Methods in Diabetes Research," Comput. Struct. Biotechnol. J., vol. 15, pp. 104-116, 2017, doi: 10.1016/j.csbj.2016.12.005.

Hittite Journal of Science and Engineering, 2022, 9 (1) 19–25
ISSN NUMBER: 2148–4171
DOI: 10.17350/HJSE19030000251

An Investigating on DNA Binding Activity of Zn(II) Phthalocyanine Complex Having Tetra Substituted Phenoxy-3-methoxybenzoic Acid Group

Ali Arslantas[1] **Mehmet Salih Agırtas**[2] **Zekeriya Balli**[2]
[1]Izmir Bakircay University, Department of Biomedical Engineering, Izmir, Turkey
[2]Van Yuzuncu Yil University, Department of Chemistry, Van, Turkey

Article History:
Received: 2021/10/18
Accepted: 2022/03/13
Online: 2022/03/30

***Correspondence to**: Ali Arslantas, İzmir Bakırçay University, Department of Biomedical Engineering, 78050, İzmir, Turkey.*
E-Mail: arsoz33@gmail.com
Phone: +90 (232) 493 00 00
Fax: +90 (232) 844 71 22

ABSTRACT

The tetra substituted Zn(II) phthalocyanine complex having the dicyanophenoxy)-3-methoxybenzoic acid group had been obtained from 4-(3, 4-dicyanophenoxy)-3-methoxybenzoic acid and analyzed with the application of FT-IR, NMR, UV/Vis techniques in compliance with reported literature. The interacting property of 2,10,16,24–tetrakis (phenoxy-3-methoxybenzoic acid) phthalocyaninato) Zn(II) by CT-DNA was examined with absorption bands, emission titrations, melting temperature, viscosity, and gel electrophoresis procedures. The obtained findings from these techniques demonstrated that the complex containing the dicyanophenoxy)-3-methoxybenzoic acid binds to the DNA by means of intercalation attachment mechanisms.

Keywords:
CT-DNA; Zinc phthalocyanine; Absorption spectra; Gel electrophoresis

INTRODUCTION

The phthalocyanine metal complexes have distinct pharmacologic and biologic activities such as anticancer, enzyme inhibition, and antimicrobic activities [1-7]. Currently, the investigations over the attachment activities of metallic phthalocyanine complexes by DNA have gotten great attention to develop new anticancer medicines [8,9]. Due to their unique pharmacologic and biologic activities, the metal complexes of phthalocyanines are used as anticancer medicines because of their very large π-delocalized surface area that are easily changed depending on biological system [10-13].

Carcinoma infection is an important healthiness issue around the globe and many people die because of this health problem. Nowadays, cancer treatment scientists concentrate their studies on aiming cell cycle and DNA interaction mechanisms. Therefore, DNA has been considered to be cellular target for therapeutic molecules. The interaction characteristics of transition metal complexes with DNA had been studied understanding how the acting of their tumor prevention activities of new anticancer medicine for cancer therapy [14,15]. A substantial part of cancer therapy comprises of metal complexes which bind to DNA or inhibit the DNA relaxation [16, 17]. The interaction of drugs with DNA molecule may modify the building of DNA [18]. Therapeutic drugs also binding to DNA can cause in difference in replication of DNA molecule and expression of gene [19, 20]. It is thought that there are fundamental interaction modes of tiny compounds with DNA molecule are intercalative and non-intercalative binding mechanisms [19, 21]. The physicochemical activities of metal phthalocyanine complexes may be arranged by altering the transition metal ions and the environmental substituent [22]. Studies in recent years, the binding characteristics of the phthalocyanine compounds to DNA because of preventing of direct or indirect growth of cancerous tumor had accelerated in the literature.

In this current study, the complex of 2,10,16,24–tetrakis (phenoxy-3-methoxybenzoic acid) phthalocyaninato) Zn(II) (Pc4) had been studied via NMR, FT-IR, UV/Vis techniques. The interaction properties of Pc4 with DNA (Calf Thymus DNA) had been analyzed by carrying out electronic spectra titration, fluorescence spectra, the melting temperature, viscosity and the electrophoresis methods. The obtained findings from this study could be a revelation for new investigation regarding cancer medication.

MATERIAL AND METHODS

Acetonitrile, DMF, DMSO, 4-hydroxy-3-methoxybenzoic acid, K_2CO_3, methanol, THF and $ZnCl_2$ reagents were commercially purchased from the commercial company and also the chemicals such as DNA, Tris-HCl and NaCl were supplied by Sigma Aldrich commercial company. The NMR experiments were carried out using Agilent Spectrometer and for IR measurements, Thermo Scientific FT-IR spectroscopy was conducted at room temperature. For the UV/Vis analyses, Cary UV/Vis spectroscopy was used and fluorescence spectroscopic measurements were recorded by a Perkin Elmer LS Fluorescence Spectroscope. In this study, for the electrophoresis measurements, Thermo Scientific owl electrophoresis instrument was used in a buffer solution at room temperature. Ubbelohde viscometer system was used for the viscosity measurements.

The Synthesis of 4-(3,4-dicyanophenoxy)-3-methoxybenzoic acid compound (3)

The compound of 4-(3, 4-dicyanophenoxy)-3-methoxybenzoic acid was synthesized in conformity with the published literature [23].

The synthesis of 2,10,16,24–tetrakis (phenoxy-3-methoxybenzoic acid) phthalocyaninato) Zn(II) complex (4)

The phthalocyanine complex of zinc (II) was synthesized by means of interaction of 4-(3,4-dicyanophenoxy)-3-methoxybenzoic acid compound in the presence of $ZnCl_2$ according to reported literature [23]. A mixture of 4-(3,4-dicyanophenoxy)-3-methoxybenzoic acid 3 (0.050 g, 0. 17 mmol) and $ZnCl_2$ (0.022 g) was powdered in a quartz crucible and heated in a sealed glass tube for 6 min under nitrogen at 270 °C. The reaction was terminated by pouring the solution into an aqueous solution of 2 M HCl followed by overnight storage. The precipitates were filtered and washed with water and acetic acid to a neutral pH. The product was washed with cold and hot methanol. The THF soluble were taken, and final product was obtained by solvent THF removal. The product is soluble in THF, DMF and DMSO. The yield was 0.019 g (38 %). MALDI-TOF MS: m/z$[M]^+$ Calcd. for $C_{64}H_{40}N_8O_{16}Zn$: 1242.43; found 1241.23$[H]^+$. IR spectrum (cm^{-1}):3525, 3078, 2935, 1691, 1591, 1467, 1400, 1267, 1213, 1176, 1112, 1093, 1029, 945, 881, 742. UV-Vis (THF) λmax (log ε): 674 (5.24), 608(4.65), 348(5.04). ^{1}H NMR (400 MHz, DMSO-d_6) δ ppm: 8.53, 7.78, 7.22, (Ar-H), 3.85(CH_3), 3.33(DMSO-d_6) 2.48(DMSO-d_6), 1.13 (CH_3) [23].

DNA binding experiments

The binding of Pc4 to CT-DNA was investigated by UV/vis, emission titration, melting point viscosity and gel electrophoresis experiments to analyze its binding activities with DNA. CT-DNA samples were prepared in the Tris-HCl buffer solution. UV absorbance of CT-DNA stock solution in buffer at 260 nm was measured and it was found that CT-DNA stock solution was free of protein. CT-DNA sample was kept at 4 °C overnight and used within 2 days. The solutions of the complex were prepared in DMF solvent and diluted in the Tris-HCl/NACl buffer solution at pH 7.03. The UV/vis absorption spectra titrations were carried out between 260 and 800 nm at 25 °C. Absorption spectra, emission titrations were performed fixed concentrations of the complex (20 μM) and spectra were recorded after each adding. For the all experiments, the solutions were incubated for 5 min for each run. Melting point study, the certain amounts of CT-DNA and Pc4 were heated up through 25 °C to 95 °C. The mixture of CT-DNA + Pc4 was incubated at the certain time for each 5 °C and the values of absorption titration were recorded.

For agarose gel electrophoresis studies was performed using Thermo Scientific Owl Electrophoresis System and for the viscosity measurements, Ubbelohde viscometer apparatus was used.

RESULTS AND DISCUSSION

The chemical synthesis route of Zn(II) phthalocyanine complex is indicated in Figure 1. The four peripheral substituted the Zn(II) complex was synthesized via cyclotetramerization of the compound by refluxing to $ZnCl_2$ at certain temperature and underneath nitrogen gas. The Pc4 complex was qualified with UV/Vis, FT-IR and the NMR measurements. The obtained findings were consistent with the prospective molecular structure. The characterization of the complex was reported in literature [23].

The characterization of the compound including a combining of techniques, involved elemental analysis, FT-IR, UV/Vis, and ^{1}H NMR spectroscopy. The spectroscopic data of the complex consistent with its proposed chemical structure. In the ^{1}H NMR spectrum, the expected aromatic protons for Pc4 are observed at 8.53, 7.78 and 7.22 ppm, while aliphatic CH_3 groups are observed at 3.85 and 1.13 ppm. IR spectral data of the compound as expected, OH groups at 3525 cm^{-1}, Ar-H vibrations at 3078 cm^{-1}, CH_3 vibrations at 2935 cm^{-1}, C=C vibrations at 1691 and 1591 cm^{-1}, Ar-O-Ar

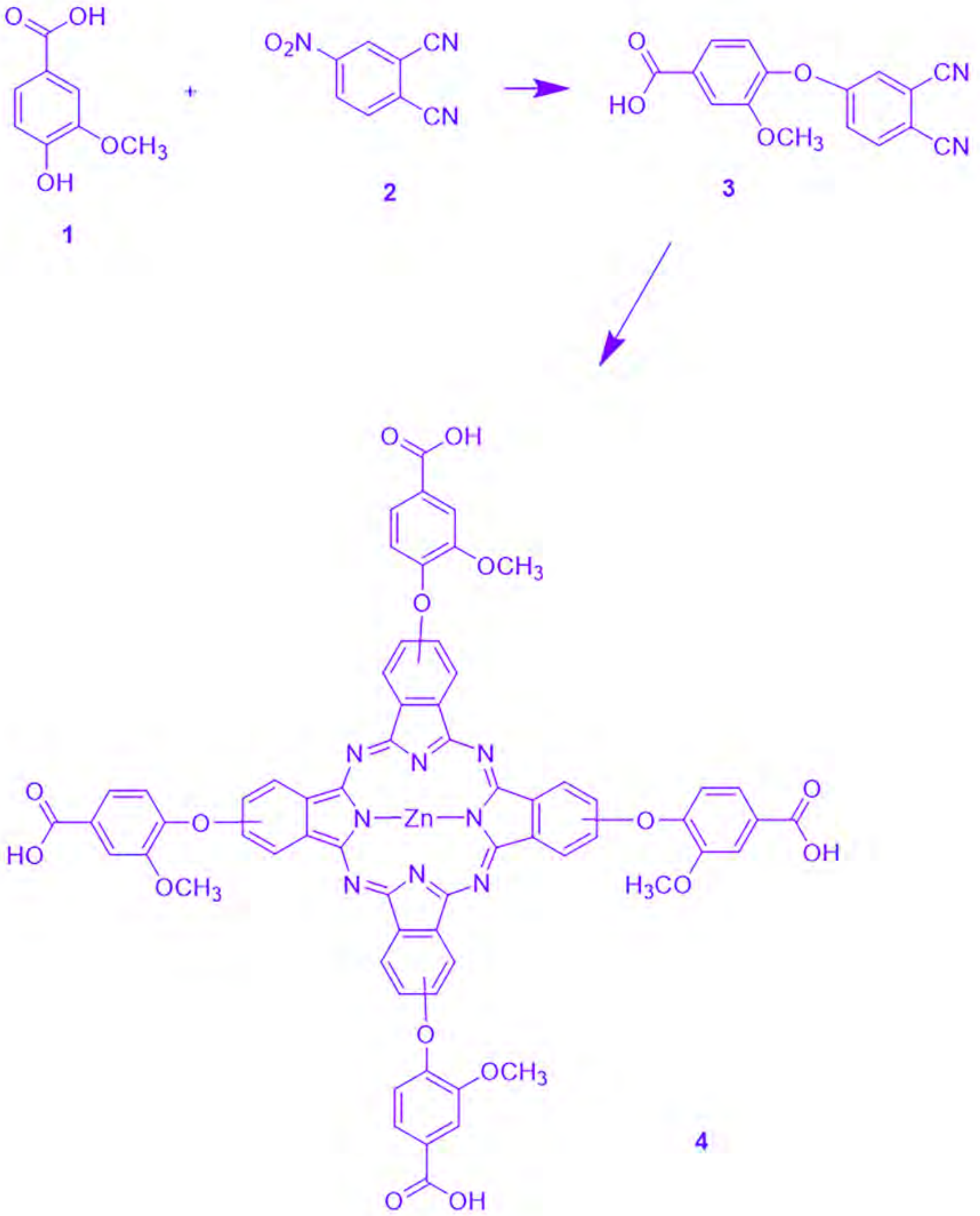

Figure 1. The chemical synthesis route of Zn(II) phthalocyanine complex.

vibrations at 1267 cm^{-1} is also observed. The UV-Vis absorption spectrum data of the zinc phthalocyanine compound give the characteristic absorption bands of the phthalocyanine compound, Q and B bands, at 674 and 348 nm, respectively. It yields the shoulder band at 608 nm as expected.

The binding study of Zn (II) phthalocyanine complex with the DNA

UV/Vis titrations were conducted by increasing concentration of the DNA with a constant concentration (20 µM) of Pc4 and electronic spectra had been recorded afterward adding of the DNA sample. In this study, also the binding constant (K_b) was computed by using Wolfe-Schimer equation [24]. With increases in amount of the DNA, the absorbance values of Pc4 gradually dropped. The dropping of absorbance values demonstrated that the complex Pc4 interacts with CT-DNA and also three main absorbance bands were observed with hypochromism, and these bands were located at around 362, 625 and 682 nm related to the red shift as illustrated in Figure 2. The complex showed hypochromism, which reducing in absorption spectra is called as a hypochromism and incrementing in absorbance values is defined as a hyperchromism. Hypochromicity is related to a mild bathochromic shifting generally originated from the intercalation binding mechanism, comprising a packing interaction among a chromophore compound and DNA base pairs [13]. The Pc4 complex is quite planar central part and it can likely interact with the DNA by an intercalating binding mechanisms. The obtained results from absorption titration method showed that Pc4 complex binds to the DNA molecule through an intercalative mechanism, and the K_b value for Pc4 was obtained as 2. 17 x 10 6 M^{-1} as indicated in Figure 2. The calculated Kb value for the complex also demonstrated that Pc4 binds to the DNA with the intercalation mechanisms.

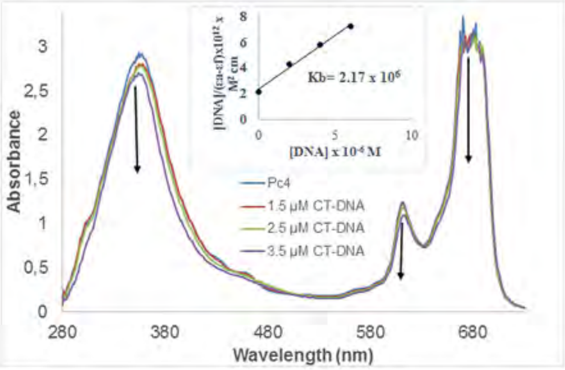

Figure 2. Electronic titrations of Pc4 in the buffer system on addition of calf thymus DNA. [Pc4] = 20μM and [CT-DNA] = 0–3.5μM. The arrows represent the dropping in absorption intensities on increasing the calf thymus DNA amount.

The emission titration studies

The emission study is frequently used to determine the investigating of DNA-drug binding activity because this technique is a very sensitive to explain DNA interaction probes and it can provide further information about the intercalation of molecular compounds [25]. In this present study, the DNA binding activity of Pc4 to the DNA was investigated using emission titration spectra. When the complex Pc4 was interacted with the DNA, it was seen that the intensities of emission spectra were dropped gradually as indicated in Figure 3. The dropping in emission intensity demonstrated that the complex binds to the DNA using hypochromic mechanism. It is seen in Figure 3 that the complex Pc4 gave a strong emission spectra in the absence of CT-DNA at pH 7.03 at around 457 nm. The strong fluorescence spectra could be originated from the ligand [25]. On the adding of the DNA, the decreases in intensity of emission spectra for Pc4 were illustrated in Figure 3. The findings from this technique demonstrated that Pc4 interacts with the DNA via the mechanism of intercalative binding.

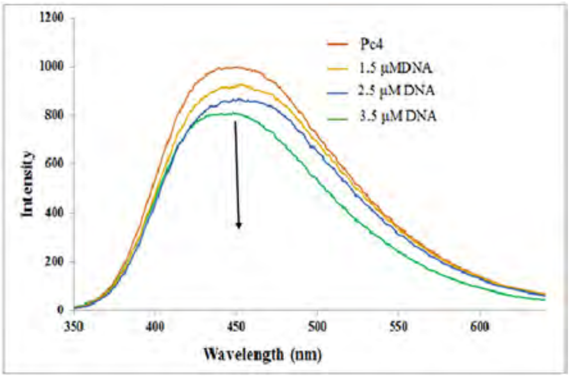

Figure 3. Fluorescence titrations of Pc4 in the buffer solution in the absence and presence of the DNA. [Pc4] = 20μM and [CT-DNA] = 0 – 3.5μM. The arrow displays the intensity change on mounting the DNA concentration.

The viscosity studies for DNA Binding

In addition, the above methods, the viscosity technique was also applied to search DNA binding activity of Pc4. The viscosity method could supply more information about DNA interaction mechanisms that is very precise to change in length of DNA molecule. Generally, when a chemical complex inserts into the base pairs of DNA, DNA molecule elongates because the base pairs of DNA are decomposed to adapt the attached ligand, which causes to increases in the DNA viscosity [25]. On the other hand, chemical compounds react with DNA by non-intercalative binding mode may decrease the length of DNA by twisting the DNA [26] but, non-intercalative and electrostatic binding mechanisms cause to very a little impact upon DNA viscosity.

In the present study, the changing in the DNA viscosity in the presence of Pc4 was monitored. When the complex reacts with the DNA molecule in an intercalative binding mechanisms, it has an impact upon the DNA viscosity. It is indicated in Figure 4 that on the adding of Pc4 to the DNA, the surge in the DNA relative viscosity was observed. The increasing in CT-DNA viscosity that could relate to the reacting of Pc4 with the DNA molecule. The obtained findings proved that Pc4 attaches to the DNA via intercalative binding mechanisms with a strong affinity.

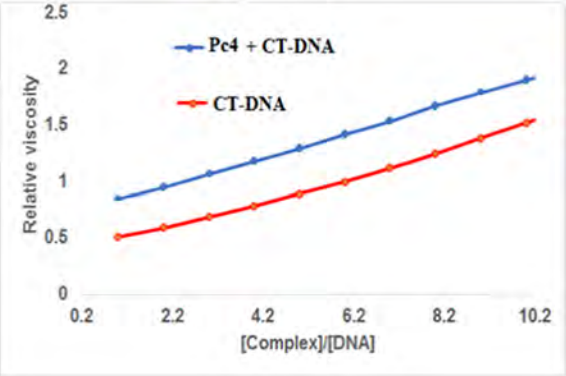

Figure 4. The viscosity study of Pc4 indicating the impact of surging amounts of the complex upon the DNA viscosity.

Thermal denaturation studies for DNA binding

The solution of CT-DNA + Pc4 was incubated at the certain time for each 5 °C and the values of absorption titration were recorded. The recorded absorbance values versus temperature chart were plotted as illustrated in Figure 5. It is observed in Figure 5 that thermal melting temperature of CT-DNA was recorded as approximately 70.40 °C, and the Tm value of CT-DNA + Pc4 was observed as 78.63 °C. Mostly, if the thermal melting variation of the DNA sample and CT-DNA + Pc4 is great, the DNA binding activity is believed to be an intercalation. If this value is not great, the DNA binding mechanism is considered as a non-intercalation. The obtained result from the viscosity measurement demonstrated that Pc4 reacts with the DNA by an intercalative binding mechanism.

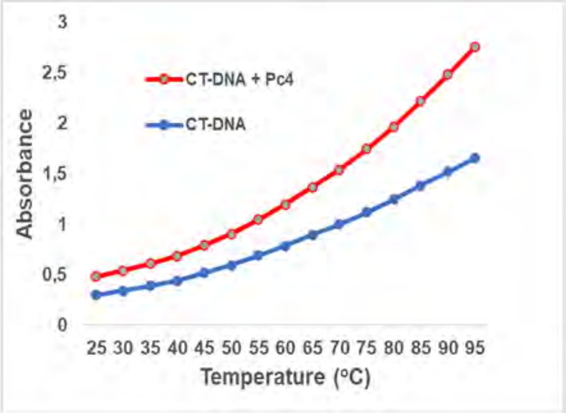

Figure 5. T_m study of the DNA showing impact of the compound on melting temperature of the DNA. The Tm measurements of the DNA (blue line) and DNA + Pc4 (red line).

The agarose gel electrophoresis study for DNA binding

In the literature, the binding activities of the compounds to CT-DNA were studied using agarose gel electrophoresis technique analyzing of the impact of different amounts of the Pd(II) compounds on CT- DNA. In this study, results showed that the intensities of CT-DNA bands obtained for the compounds after interacting with CT-DNA were dropped, as compared with control CT-DNA band. The drop in the intensities of the DNA bands observed after interacting of the compounds with the DNA is thought to be damage deformation of CT-DNA [27].

In addition to above studies, DNA binding activity for Pc4 complex was studied using agarose gel electrophoresis technique. First of all, the migrating of CT-DNA + Pc4 was recorded afterwards GelRed staining as shown in Figure 6. The lane M refers the ladder of DNA, and the lanes 1, 2 and 3 refer the compound Pc4, respectively with varied amounts of the DNA. The amount of DNA surged from the lanes 1 to 3. The concentration of Pc4 was hold fixed at 25 µM, whereas the amounts of DNA was changed from 15 to 25 µM. Then, the intensity of the DNA band was recorded in the absence of Pc4 and also the band intensity of the DNA was monitored in the presence of Pc4. It is clearly seen that in Figure 6, the DNA bands intensities were dropped and the migrating of CT-DNA bands were slightly vanished because of the DNA neutralization. The results demonstrated that Pc4 interacts by the DNA.

CONCLUSION

In the present study, the objective of the study was to explain the binding activity of the metal complex to CT-DNA for potential use of an anticancer medicine. First of all, the zinc (II) phthalocyanine compound was synthesized and analyzed with electronic spectra, FT-IR and NMR instruments according to the reported procedure in literature. The DNA binding activity of the complex was evaluated using with various methods such as absorption spectra, fluorescence titrations, melting point, viscosity

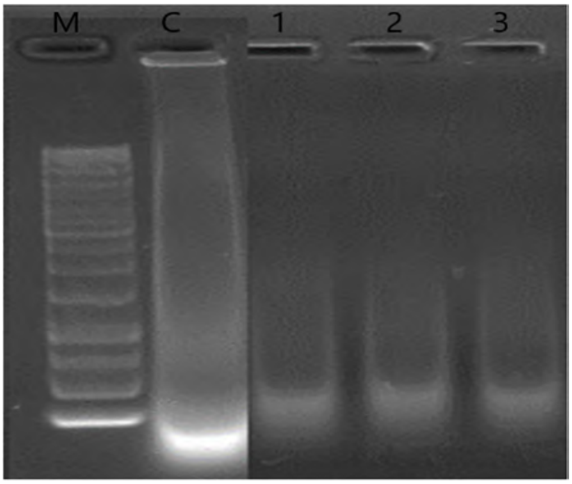

Figure 6. Agarose gel electrophoresis studies for Pc4 complex at pH 7.03 on surging the amount of CT-DNA. Lane M: DNA ladder, Lane C: control CT-DNA, Lanes 1 to 3: (Pc4 (20 µM) + CT-DNA (15, 20, 25 µM), respectively.

and the electrophoresis experiments. The obtained findings from these methods demonstrated that the metal complex binds to the DNA through the intercalative binding mechanisms. In addition to above techniques, the electrophoresis study was also studied to evaluate the DNA binding to mode for this compound. The results from gel electrophoresis method showed that the compound interacts with the DNA. The obtained results demonstrated that the complex can be evaluated as a potential candidate of anticancer medicine due to its binding activity to DNA molecule.

ACKNOWLEDGMENTS

This research was supported by the Commission of Scientific Research Project of Karabük University. Project No: KBÜBAP-18-DS-046.

CONFLICT OF INTEREST

Authors approve that to the best of their knowledge, there is not any conflict of interest or common interest with an institution/organization or a person that may affect the review process of the paper.

AUTHOR CONTRIBUTION

All sections including methodology, the experiments, analysis, writing, review and editing the manuscript was organised and performed by Ali Arslantaş. Mehmet Salih Ağırtaş and Zekeriya Ballı synthesized and characterized the compound.

References

1. Yılmaz F, Ozer M, Kani I, Bekaroglu O. Catalytic activity of a thermoregulated, phase-separable Pd(II)-perfluoroalkyl phthalocyanine complex in an organic/fluorous biphasic system: hydrogenation of olefins. Catalysis Letters 130 (2009) 642-647.
2. Leznoff CC, Lever ABP. Phthalocyanines Properties and Applications, VCH Publisher, New York, 2, 1993.
3. Leznoff CC, Lever ABP. Phthalocyanines Properties and Applications, VCH Publisher, New York, 1, 1989.
4. Parra V, Bouvet M, Brunet J, Rodríguez-Mendez ML, Saja JA. On the effect of ammonia and wet atmospheres on the conducting properties of different lutetium bisphthalocyanine thin films. Thin Solid Films 516 (2008) 9012-9019.
5. Bouvet M. Phthalocyanine-based field-effect transistors as gas sensor. Analytical and Bioanalytical Chemistry 384 (2006) 366-373.
6. Rosenthal I. Phthalocyanines as photodynamic sensitizer. Photochemistry and hotobiology 53 (1991) 859-870.
7. Leznoff CC, Lever ABP. Phthalocyanines, Properties and Applications, VCH Publisher, New York, 1996.
8. Hadjiliadis ND, Sletten E. Metal complex–DNA Interactions, Wiley-Blackwell, New York, 2009.
9. Van Holst M, Grant MP, Aldrich-Wright J. Metallointercalators-Synthesis and Techniques to Probe Their Interactions with Biomolecules, Springer Wien, New York, 2011.
10. Lukyanets EA. Phthalocyanines as photosensitizers in the photodynamic therapy of cancer. Journal of Porphyrins and Phthalocyanines 3 (1999) 424–432.
11. Vummidi BR, Noreen F, Alzeer J, Moelling K, Luedtke NW. Photodynamic agents with anti-metastatic activities. ACS Chemical Biology 8 (2013) 1737–1746.
12. Yildiz BT, Sezgin T, Cakar ZP, Uslan C, Sesalan BS. The use of novel photobleachable phthalocyanines to image DNA. Synthetic Metals 161 (2011) 1720–1724.
13. Amitha GS, Vasudevan S. DNA/BSA binding studies of peripherally tetra substituted neutral azophenoxy zinc phthalocyanine. Polyhedron 175 (2020) 114208.
14. Ali A, Bhattacharya S. DNA binders in clinical trials and chemotherapy. Bioorganic Medicinal Chemistry 22 (2014) 4506–4521.
15. Alam MDF, Varshney S, Khan MA, Laskar AA, Younus H. In vitro DNA binding studies of therapeutic and prophylactic drug citral. International Journal of Biological Macromolecules 113 (2018) 300–8.
16. Palchaudhuri R, Hergenrother PJ. DNA as a target for anticancer compounds: methods to determine the mode of binding and the mechanism of action. Current Opinion in Biotechnology 18 (2007) 497–503.
17. Bağda E, Yabaş E, Bağda E. Analytical approaches for clarification of DNA-double decker phthalocyanine binding mechanism: As an alternative anticancer chemotherapeutic. Spectrochimica Acta Part A: Molecular and Biomolecular Spectroscopy 172 (2017) 199–204.
18. Rescifina A, Zagni C, Varrica MG, Pistarà V, Corsaro A. Recent advances in small organic molecules as DNA intercalating agents: synthesis, activity, and modeling. European Journal of Medicinal Chemistry 74 (2014) 95–115.
19. Ozluer C, Satana Kara HE. In vitro DNA binding studies of anticancer drug idarubicin using spectroscopic techniques. Journal of Photochemistry and Photobiology. B, Biology 138 (2014) 36–42.
20. Williams AK, Dasilva SC, Bhatta A, Rawal B, Liu M, Korobkova EA. Determination of the drug-DNA binding modes using fluorescence-based assays. Analytical Biochemistry 411 (2012) 66–73.
21. Özkay Y, Işıkdağ İ, İncesu Z, Akalın G. Synthesis of 2-substituted-N-[4-(1-methyl-4,5-diphenyl-1H-imidazole-2-yl)phenyl]acetamide derivatives and evaluation of their anticancer activity. European Journal of Medicinal Chemistry 45 (2010) 3320–3328.
22. Uslan C, Sesalan BŞ. The synthesis, photochemical and biological properties of new silicon phthalocyanines. Inorganica Chimica Acta 394 (2013) 353–362.
23. Özgül G, Taştemel A, Özkaya AR, Bulut M. Synthesis, characterization and comparative electrochemistry of beta and alpha tetra-[4-oxy-3-methoxybenzoic acid]-substituted Zn(II), Co(II) and Cu(II) phthalocyanines. Polyhedron 85 (2015) 181-189.
24. Wolfe A, Shimer GH, Meehan T. Polycyclic aromatic hydrocarbons physically intercalate into duplex regions of denatured DNA. Biochemistry 26 (1987) 6392–6396.
25. Liu X-W, Shen Y-M, Li Z-X, Zhong X, Chen Y-D, Zhang S-B. Study on DNA binding behavior and light switch effect of new coumarin-derived Ru (II) complexes. Spectrochimica Acta Part A: Molecular and Biomolecular Spectroscopy 149 (2015) 150–156.

26. Barton JK, Goldberg JM, Kumar CV, Turro NJ. Binding modes and base specificity of tris(phenanthroline) ruthenium (II) enantiomers with nucleic acids: tuning the stereoselectivity. Journal of American Chemical 108 (1986) 2081–2088.

27. Shoukry AA, Mohamed MS. DNA-binding, spectroscopic and antimicrobial studies of palladium (II) complexes containing 2,20 -bipyridine and 1-phenylpiperazine. Spectrochimica Acta Part A: Molecular and Biomolecular Spectroscopy 96 (2012) 586–593.

Hittite Journal of Science and Engineering, 2022, 9 (1) 27–36
ISSN NUMBER: 2148–4171
DOI: 10.17350/HJSE19030000252

Optimal Design of an In-flight Refueling Door Mechanism

Hasan Akman **Ali Emre Turgut** **Hakan Çalışkan**
Middle East Technical University, Department of Mechanical Engineering, Ankara, Turkey

Article History:
Received: 2021/11/02
Accepted: 2022/03/18
Online: 2022/03/30

***Correspondence to**: Hasan Akman,*
Deparment of Mechanical Engineering,
Middle East Technical University,
Ankara, Turkey
Tel: +90 545 710 19 91
E-Mail:h.akman06@gmail.com

ABSTRACT

In this study, the preliminary design of an in-flight refueling door mechanism is performed. A systematic design methodology is introduced and used in the design of the refueling door mechanism. The design is divided into two sub-functions: door opening and actuation. Nine different mechanism concepts are created for the door opening function and eight different concepts are created for the actuation function. Pugh decision matrix method is used to evaluate and select the most feasible options. Six experienced engineers scored the option set, resultantly two concepts for the door opening and three concepts for the actuation sub-function are selected. Kinematic synthesis of these concepts is performed and used to determine the upper and lower bounds during optimization. Kinematic and force analysis of the concepts are performed and utilized for the constraints and cost function calculations of the optimization algorithm. Multi-objective Genetic Algorithm optimization technique is used to optimize the parameters of the selected mechanisms. The best mechanism for each sub-function is selected and combined to reach the final design. It was shown that through optimization, the required input torque decreased approximately 20% for the door opening mechanism and the required input force decreased approximately 42% for the actuation mechanism when compared to the graphical synthesis results.

Keywords:
Optimal design; Door mechanism; Genetic algorithm; Four-bar linkage; Six-bar linkage; Multi-objective optimization

INTRODUCTION

Aerial refueling is the process of transferring fuel from a tanker aircraft to a receiving aircraft when both aircrafts are flying [1]. The purpose of this operation is to extend the operation time and range of aircrafts. There are mainly two types of refueling systems used in modern aircrafts. One is the probe-and-drogue type [12] and the other is the flying boom type [13]. In probe-and-drogue type refueling system, there is a flexible hose on the tanker aircraft and a probe on the receiving aircraft that is inserted to the hose through the drogue for refueling. In the flying boom type refueling system, there is a rigid telescopic tube that extends from the tanker aircraft to the receiving aircraft and the tube is inserted to a receptacle on the receiving aircraft. In most of the modern aircrafts and in this paper, due to faster fuel transfer, flying boom type refueling system is used.

In the flying boom type refueling system, there is a receptacle that receives the fuel and this receptacle is protected by the in-flight refueling door. Before refueling, the door, mostly made in two parts, opens symmetrically so that the telescopic tube engages with the receptacle on the receiving aircraft. Different door opening mechanisms in different contexts have been studied in the literature. One of them was the swing plug door [2]. It had a four-bar mechanism that opened laterally and occupied small space when fully opened. The same mechanism was also used for luggage door mechanisms on commercial vehicles [3]. It was mentioned that the parallel-hinged system has a narrow and safe trajectory and takes up less space when fully open. Several different door hinge mechanisms have been designed for different applications such as cabinet doors [14] and garage doors [4]. Another multi-link door mechanism was the invisible hinge [5]. The design allowed the door to open up to 180° and did not show the hinge externally when the door is in the closed position. Toropov and Robertis [6] proposed an analytical approach for the design of invisible hinge mechanisms.

To obtain symmetric motion [15] as in the case of two-part refueling doors, different types of mechanisms are used. Gripper mechanisms are one of the examples of this type of mechanism. Lanni and Ceccarelli used an industrial two-finger gripper, which was powered and controlled by one actuator. A prismatic joint and revolute joint were combined to actuate the gripper mechanism symmetrically [7]. Another two-finger gripper mechanism was introduced by Nuttall and Breteler [8]. One inverted-crank mechanism was used in a piston-cylinder arrangement, and two four-bar mechanisms were used to transmit the motion to two sides of the gripper.

Different methodologies have been employed in the design of mechanisms. In [16] different mechanisms are created based on degree of freedom requirements and evaluated systematically based on the functional requirements. Automatic synthesis of three degrees of freedom closed-loop mechanisms are performed based on contracted graphs and topological graphs in [17, 18]. In [19] functional requirements, structural requirement, and design constraints are considered. Atlas of mechanism is used to find the compatible kinematic structure in a systematically.

The aim of this study is to synthesize an optimal in-flight refueling door mechanism for a flying boom type refueling system with a systematic design methodology as in [16, 17, 18]. The mechanism should provide the required clearance when refueling door is open, should close firmly in its place and should occupy as small space as possible.

Different studies have been performed to optimize mechanism with Genetic Algorithm [20, 21]. In this study, a design methodology is introduced to synthesis mechanism for different problems and optimize these mechanisms with Genetic Algorithm. Therefore, contribution of this study is developing a design methodology, which is combination of a systematic way of mechanism synthesis and optimization with using Genetic Algorithm.

METHOD

Design Methodology

In this paper, a systematic design methodology is proposed and followed in the design of the in-flight refueling door mechanism as illustrated in Fig. 1.

First, the problem is defined, and the main function is subdivided into sub-functions. Following that concepts are created for each sub-function. Then, the concepts are evaluated based on the evaluation criteria by experienced designers such that two or three best mechanisms are selected for each sub-function. Kinematic synthesis for each mechanism is performed and these results are used to determine the upper and lower boundaries of design parameters for the optimization. Following that, position and force analysis of each concept is performed and used during optimization for the constraints and cost function. Each concept is then optimized using Genetic Algorithm (GA) method [20, 21]. Finally, based on the optimization results, the best mechanism for each sub-function is selected and then combined to form the final design.

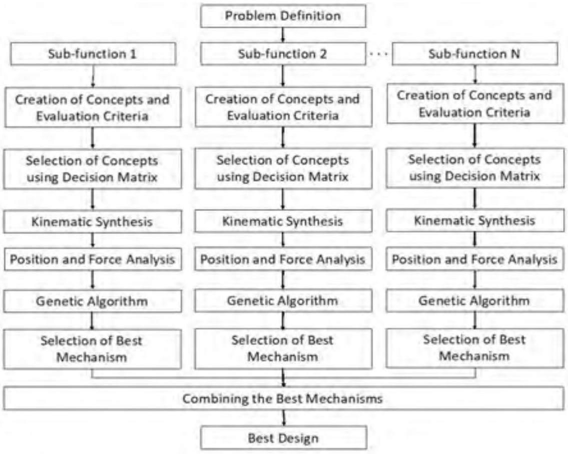

Figure 1. The systematic design methodology.

Design of the Refueling Door Mechanism

In this paper, the problem is to design an in-flight refueling door mechanism for a flying boom type refueling system. The design of the door actuation mechanism is performed based on the design methodology presented. The main function is divided into two sub-functions: door opening, and actuation as shown in Fig. 2. The door might open later-ally or 180° and the actuation might be via a rotary actuator or a linear actuator. Different concepts are created for each sub-function they are evaluated by weighted decision matrix method. The selected concepts are synthesized using graphical methods [9-10]. After synthesis of the mechanisms, position and force analyses are performed. Each mechanism is then optimized using multi-objective GA method. The best concepts for each sub-problem is combined to form the final design.

THEORY/CALCULATION

Conceptual Design

In the conceptual design, different concepts are created for the door opening and actuation sub-functions.

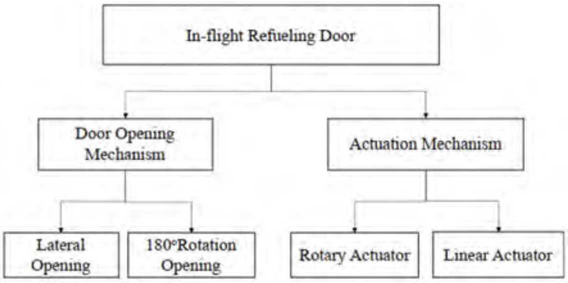

Figure 2. In-flight refueling door sub-functions and different ways of satisfying these functions

Door Opening Mechanism Concepts

Due to aerodynamic effects and space limitations, the door is designed such that it has two parts and opens symmetrically outwards. For the sake of convenience, only one part of the door and its opening mechanism is shown here. Nine different concepts are developed (only five of these concepts are depicted in Fig. 3); some opening the door laterally and some opening 180°. These concepts are: D1: A four-bar mechanism. The door opens laterally, and it is rigidly connected to the coupler link (Fig. 3a). D2: A Watt I type six-bar mechanism. The door opens laterally (Fig. 3b). D3: A Stephenson III type six-bar mechanism (Fig. 3c). The door opens laterally. D4: A four-bar mechanism. The door opens up to 180° and connected to the follower link. D5: A four-bar mechanism. The door opens 180° and connected to the coupler link (Fig. 3d). D6: A Watt I type six-bar mechanism. The door opens up to 180°. D7: A Watt I type six-bar mechanism. The door opens up to 180°. D8: A Watt II type six-bar mechanism. The door opens up to 180°. D9: An invisible hinge mechanism [5, 6]. Revolute and sliding joints are used. The door opens up to 180° (Fig. 3e).

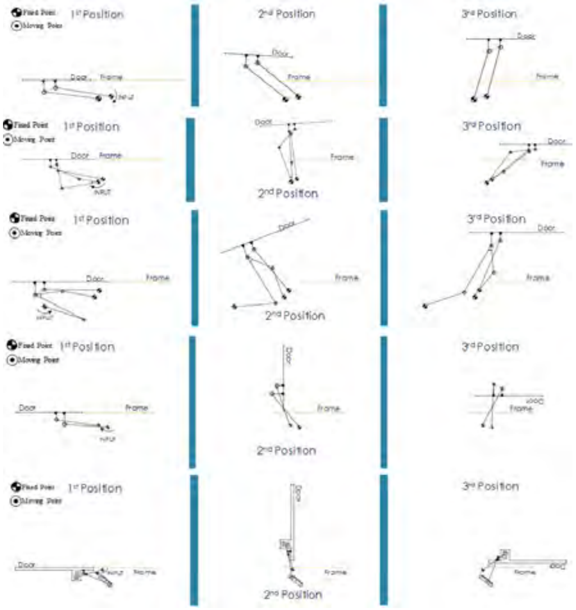

Figure 3. Optional concept sets for door opening mechanism. Only five concepts are shown. (a) D1, (b) D2, (c) D3, (d) D5 and (e) D9.

Actuation Mechanism Concepts

Eight different concepts (one with rotary actuator and the rest with linear actuators) are developed for the actuation mechanism (five of these concepts are depicted in Fig.4). Some of these concepts are designed to be 1-DOF and the others are 2-DOF.

Those optional concepts are A1: A slider-crank mechanism actuated by two linear motors. The followers are connected to the door opening mechanism (Fig. 4a). A2: A planar mechanism actuated by single linear motor as in [7]. The followers are connected to the door opening mechanism as in A1. The slider-crank is in the form of piston-cylinder arrangement. A3: A planar mechanism actuated by a linear motor formed by two four-bar and an inverted slider crank mechanism as in [8]. The slider-crank is arranged as in A2. The followers of the four-bar mechanism are connected to the door opening mechanism and cranks are used to transmit the motion as in A2 (Fig. 4b). A4: A planar mechanism actuated by a single linear motor formed by a Watt II type six-bar and an inverted slider-crank mechanism. The six-bar mechanism transmits the motion to the other side to provide symmetrical motion. The followers are connected to the door opening mechanism as in A1 (Fig. 4c). A5: A planar mechanism actuated by a single linear motor

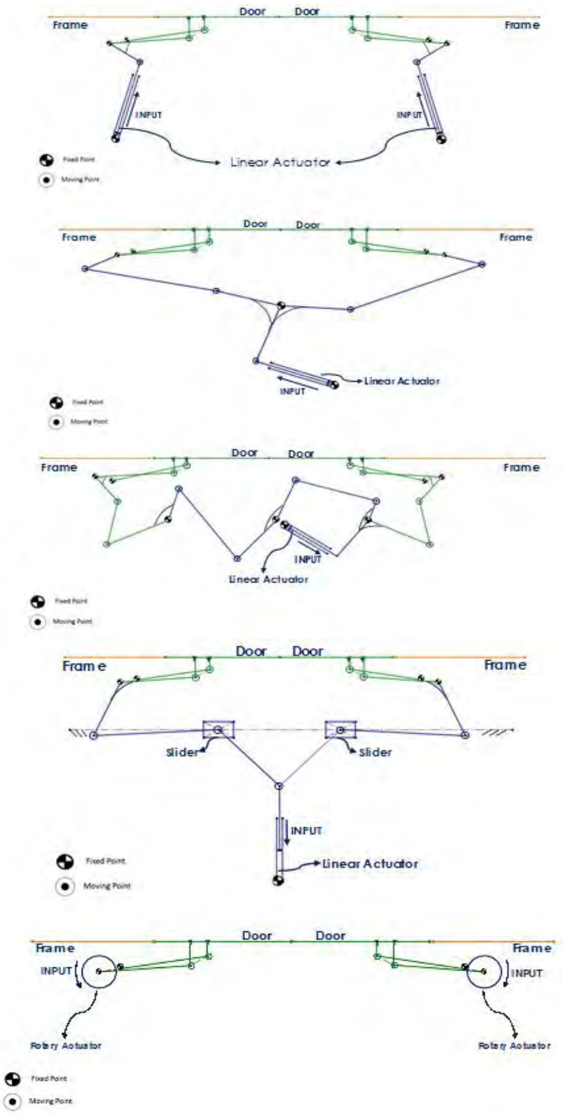

Figure 4. Optional concept sets for the actuation mechanism. Only five concepts are shown. All concepts are integrated to D5 for demonstration without the loss of generality. (a) A1, (b) A3, (c) A4, (d) A6, (e) A8.

Table 1.Weighted decision matrix of the door opening concepts. Simplicity, maintainability, simplicity of assembly, reliability, rigidity, mobility and design flexibility, space utilization, and force characteristics are used as the evaluation criteria. Weighting factors are given in the second column. The other columns represent the average score of six engineers for the corresponding evaluation criteria.

Evaluation Criteria	Wgh.	D1	D2	D3	D4	D5	D6	D7	D8	D9
Simplicity	0.161	8.7	6.0	5.5	7.5	8.1	5.3	5.1	4.7	3
Maintain.	0.125	8.8	5.3	6.3	7.8	8.2	5.7	5.3	4.6	3.3
Simp. of Assembly	0.089	8.8	5.3	5.7	8.3	8.1	5.1	5.2	5.2	4.0
Reliability	0.143	8.8	7.0	6.7	8.7	7.9	5.8	6.3	6.0	4.6
Rigidity	0.125	8.2	5.9	6.1	7.0	6.8	5.8	5.5	5.5	3.8
Mob./Flex.	0.089	5.3	7.7	7.4	5.7	5.8	7.6	7.8	7.2	6.3
Space Util.	0.107	2.1	3.9	8.4	4.7	2.8	8.3	9.4	1.0	10
Force Cha.	0.161	9.1	9.9	1.0	6.1	7.7	10	7.8	2.4	9.8
TOTAL	1	**7.8**	6.5	5.6	7.0	**7.1**	6.7	6.5	4.5	5.6

formed by a four-bar, a Watt II type six-bar, and an inverted slider-crank mechanism. The symmetrical motion is obtained by the six-bar mechanism as in A4. The followers of the four-bar and six-bar mechanisms are connected to the door opening mechanism. A6: A planar mechanism actuated by a single linear motor formed by two double slider-crank mechanisms. Symmetrical motion is provided by the two sides of the slider-crank mechanisms. The output links of the slider-crank mechanism is connected to the door opening mechanism (Fig. 4d). A7: A planar mechanism actuated by two motors using a rack-pinion arrangement. Two motors are synchronously driven. A8: Two rotary actuators are directly coupled to the door opening mechanism (Fig. 4e).

Evaluation of Concepts

The door opening and actuation concepts are evaluated separately based on different evaluation criteria. Weighting factors of these evaluation criteria are determined according to problem needs. These weighting factors can be changed for different problems. The evaluation is performed by six experienced engineers based on a value scale from 0 to 10.

Table 2.Weighted decision matrix of the actuation concepts. Simplicity, maintainability, cost, long life, simplicity of assembly, reliability, rigidity, design flexibility and space utilization are the design criteria. Weighting factor is given in the second column. The following columns show the average scores of six engineers for the corresponding evaluation criteria.

Evaluation Criteria	Wgh.	A1	A2	A3	A4	A5	A6	A7	A8
Simplicity	0.148	8.5	8	7	5	5.2	5.2	6.3	9
Maintain.	0.115	7.8	7.3	7	5.2	5.3	4.7	4.2	8
Cost	0.098	6.5	6.5	7.4	5.5	5.5	4.7	3.2	6.2
Serv. Life	0.131	8.2	7	7.7	5.7	5.7	4.8	4.5	7.3
Simp. of Assembly	0.082	8.2	7.8	7.3	4.8	4.8	4.5	4.8	8.8
Reliability.	0.131	8.2	7.2	7.2	6	6	4.8	5.2	8.5
Rigidity.	0.115	8.2	6.5	6.8	5.2	5.2	5.5	5.5	9
Flex.	0.082	7.3	6.5	6.7	6	6	5.7	6	8
Space Util.	0.098	7.3	5.7	6.3	5.2	5.2	4.7	7.3	9.2
TOTAL	1	**7.9**	7	**7.1**	5.4	5.4	4.9	5.2	**8.2**

The criteria for the door opening concepts are simplicity, maintainability, simplicity of assembly, reliability, rigidity, mobility and design flexibility, space utilization, and force characteristics. After the evaluation, shown in Table 1, D1 and D5 are selected as the best concepts.

The evaluation criteria for the actuation concepts are simplicity, maintainability, cost, long life, simplicity of assembly, reliability, rigidity, design flexibility and space utilization. After the evaluation, as shown in Table 2, A1, A3, and A8 are chosen to be the best concepts.

Kinematic Synthesis and Analysis

Kinematic synthesis, kinematic analysis and force analysis of all the best concepts D1, D5, A1 and A3 are performed (kinematic synthesis and analysis have not been performed for A8 since it only consists two rotary actuators directly coupled to the driving link of the door mechanism). Since the procedure is the same for all the mechanisms, only the kinematic synthesis and the analysis of concept D1 are presented in this paper.

Kinematic Synthesis of D1

D1, shown in Fig. 5, is designed using two position graphical synthesis method [9].

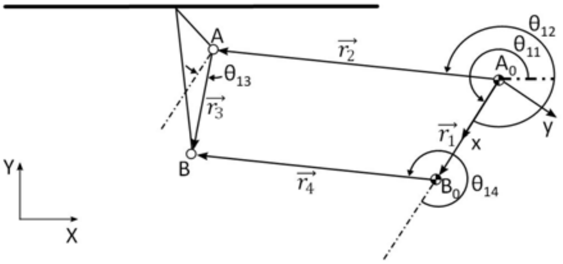

Figure 5. Schematic drawing of concept D1.

First, the initial and final positions of the door are selected then two moving points are determined as A1, A2, B1, and B2. Then these points are connected, and two perpendicular lines are drawn at the mid-points of A1A2 and B1B2 as shown in Fig. 6. Two fixed pivot points, A0 and B0 are selected at any place on the perpendicular lines. The mechanism is then synthesized joining A0, B0, B1 and A1. The parameters found after the synthesis are shown in Table 3.

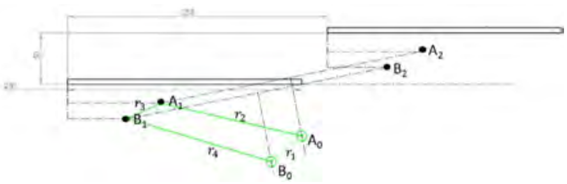

Figure 6. The two-point synthesis of concept D1

Table 3.Calculated parameters for concept D1.

1	2	3	4	5	6
r_1 (mm)	r_2 (mm)	r_3 (mm)	r_4 (mm)	Q_{12}(deg)	Q_{11}(deg)
39.05	142.24	35.32	146.65	-52.73	219.81

Kinematic Analysis of D1

Freudenstein's equation is used to perform the kinematic analysis. The loop closure equation in complex notation is given by:

$$r_2 e^{i\theta_{12}} + r_3 e^{i\theta_{13}} - r_4 e^{i\theta_{14}} - r_1 = 0 \tag{1}$$

By solving Eq. (1), the unknown joint variables are found as:

$$\theta_{13} = 2 \cdot atan\left(\frac{-B + \sigma\sqrt{B^2 - 4AC}}{2A}\right) \tag{2}$$

$$\theta_{14} = 2 \cdot atan\left(\frac{r_2 \sin\theta_{12} + r_3 \sin\theta_{13}}{r_2 \cos\theta_{12} + r_3 \cos\theta_{13} - r_1}\right) \tag{3}$$

where

$$A = (K_1 + K_2 \cos\theta_{12} - K_3 + \cos\theta_{12}) \tag{4}$$

$$B = (-2 \cdot \sin\theta_{12}) \tag{5}$$

$$C = (K_1 + K_2 \cos\theta_{12} + K_3 - \cos\theta_{12}) \tag{6}$$

$$K_1 = \frac{r_4^2 - r_1^2 - r_2^2 - r_3^2}{2 r_3 r_2} \tag{7}$$

$$K_2 = \frac{r_1}{r_3}, K_3 = \frac{r_1}{r_2}, \sigma = -1 \tag{8}$$

Eq. (2) and (3) are used to find the joint variables for every crank angle.

Force Analysis of D1

In the refueling applications high accelerations are not required, furthermore link masses are relatively small. Therefore, inertial forces are ignored, and quasi-static force analysis is performed to calculate the required driving force. An approximate value is taken for the external force and the same external force is applied to all the door opening mechanisms. The free-body diagram of each link is drawn (not shown), and unknown forces are found. The system is assumed to be in equilibrium under the action of the external force, F, and the driving torque, T_{input} as shown in Fig. 7.

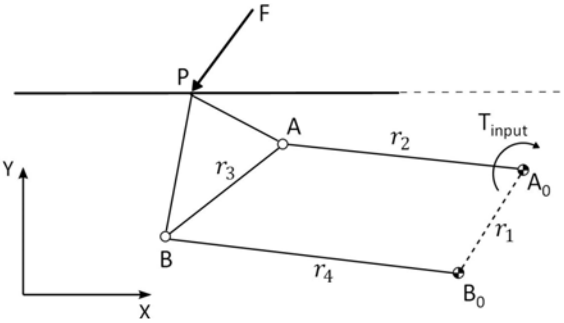

Figure 7. External force and the driving torque acting on D1.

The equilibrium equations for each link are not presented here (refer to [11] for details). Only the final results are given. In matrix form to find the forces:

$$[x] = [A]^{-1} \cdot [b] \tag{9}$$

where

$$[x] = \begin{bmatrix} F_{23x} \\ F_{23y} \\ F_{43} \\ T_{input} \end{bmatrix} \tag{10}$$

$$[A] = \begin{bmatrix} 1 & 0 & \cos(\theta_{11} + \theta_{14}) & 0 \\ 0 & 1 & \sin(\theta_{11} + \theta_{14}) & 0 \\ r_3 \sin(-\gamma) & r_3 \sin(\frac{\pi}{2} - \gamma) & 0 & 0 \\ -r_2 \sin(\pi - \theta_{11} - \theta_{12}) & -r_2 \sin(\frac{3\pi}{2} - \theta_{11} - \theta_{12}) & 0 & 0 \end{bmatrix} \tag{11}$$

$$[b] = \begin{bmatrix} -F \cos(\theta_f) \\ -F \sin(\theta_f) \\ -M - F\frac{r_3}{2}\sin(\theta_f - \gamma) \\ 0 \end{bmatrix} \tag{12}$$

The variable vector, [x] can be calculated using the known [A] matrix and [b] to find the unknown forces and the required driving torque.

Kinematic Synthesis of A1

An iterative graphical approach [10] is used to synthesize the concept A1, as shown in Fig. 8.

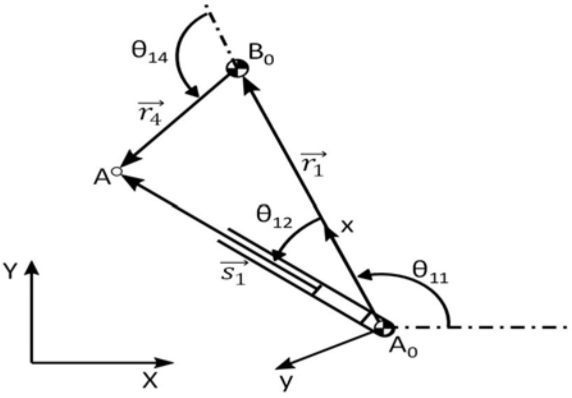

Figure 8. Schematic drawing of Concept A1.

The required rotation of the output link should be equal to the rotation of the drive link of the door opening/closing mechanism. Therefore, without loss of generality concept D1 is used for the synthesis of A1. The required driving link rotation is calculated as -131.96°. After using the graphical synthesis as in Sect. 4.1, the parameters of A1 are found as in Table 4.

Table 4.Calculated parameters for concept A1.

1	**2**	**3**	**4**	**5**
r_1 (mm)	r_4 (mm)	s_1 (mm)	Q_{11}(deg)	Δ_{stroke} (mm)
230.00	70.00	174.00	132.50	123.70

Kinematic Analysis of A1

Freudenstein's equations are used to perform the kinematic analysis of A1. The loop closure equation in complex form is given by:

$$s_1 e^{i\theta_{12}} - r_1 - r_4 e^{i\theta_{14}} = 0 \tag{13}$$

Solving the loop closure equation yields:

$$\theta_{12} = 2 \cdot \operatorname{atan}\left(\sigma\sqrt{-\frac{C}{A}}\right) \tag{14}$$

$$\theta_{14} = \operatorname{atan}\left(\frac{s_1 \sin\theta_1}{s_1\cos\theta_1 - r_1}\right) \tag{15}$$

where all the required variables are defined in Eq. 4-8.

Force Analysis of A1

Quasi-static force analysis is performed to find the required driving force. The freebody diagram of each link is drawn (not shown, refer to [11]), and all the unknown forces acting on the links are calculated. The external torque is assumed to be acting from the door opening mechanism as shown in Fig. 9.

The forces can be calculated as in Eq. 9 using:

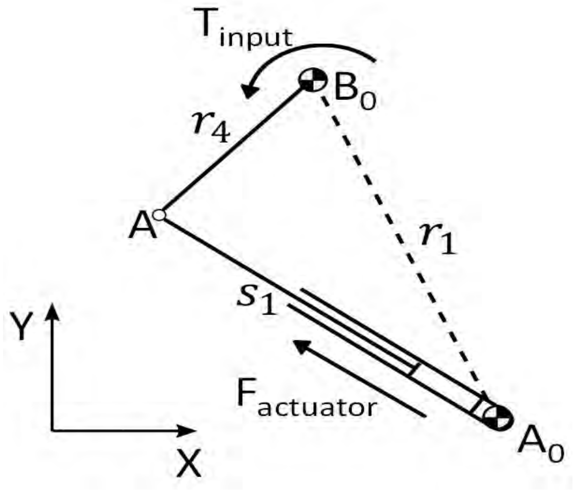

Figure 9. External torque and input force acting on A1

$$[x] = \begin{bmatrix} F_{14x} \\ F_{14y} \\ F_{34} \\ F_{actuator} \\ F_{12x} \\ F_{12y} \end{bmatrix} \tag{16}$$

$$[A] = \begin{bmatrix} 1 & 0 & \cos(\theta_{11}+\theta_{12}) & 0 & 0 & 0 \\ 0 & 1 & \sin(\theta_{11}+\theta_{12}) & 0 & 0 & 0 \\ 0 & 0 & r_4\sin(\theta_{12}-\theta_{14}) & 0 & 0 & 0 \\ 0 & 0 & 1 & -1 & 0 & 0 \\ -1 & 0 & -\cos(\theta_{12}+\theta_{11}+\pi) & 1 & 0 & 0 \\ 0 & 1 & -\sin(\theta_{12}+\theta_{11}+\pi) & 0 & 0 & 0 \end{bmatrix} \tag{17}$$

$$[b] = \begin{bmatrix} 0 \\ 0 \\ -T_{input} \\ 0 \\ 0 \\ 0 \end{bmatrix} \tag{18}$$

Optimization of the Mechanisms

All the door opening (D1, D5) and actuation mechanisms (A1, A3, A8) are optimized using the GA method with MATLAB software using the parameters shown in Table 5. These GA parameters are determined by using trial-error method after several iterations. Best results are obtained by using GA parameters, which are given in the Table 5. Different parameters can be used for different problems.

Table 5.GA parameters used during optimization

Population Size	Maximum Generation	Crossover Function	Crossover Fraction	Mutation Function
2250	500	Heuristic 1.2	0.8	Uniform 0.1

Only the optimization of D1 and A1 are presented in this paper (refer to [11] for the rest).

Optimization of D1

The door opening/closing mechanism, D1 is optimized based on a cost function and several geometric constraints

Variables: r1, r2, r3, r4, θ_{12}, initial, Δ_θ. Δ_θ is the angle per step and the other variables are shown in Fig. 5.

Cost Function: (a) A laterally opening and closing door is desired, therefore the first cost function is:

$$f(1) = \left|\theta_{3,initial} - \theta_{3,final}\right| \cdot G \tag{19}$$

(b) In order to minimize the input torque, the second cost function is defined as:

$$f(2) = \max(T_{input}) \cdot G \tag{20}$$

Where G is a parameter set to 1 if the constraints are satisfied, if not it is set to a very large number to increase the cost and penalize the solution.

Constraints: (a) The first constraint is related to the initial orientation of the mechanism given as:

$$175^\circ \geq \theta_{11} + \theta_{1,2,initial} \geq 165^\circ \tag{21}$$

$$absolute(\theta_{12,initial} - \theta_{13,initial}) > 5^\circ \tag{22}$$

(b) The second constraint is related to minimum clearance being greater than 200mm when the door is open. It is defined as:

$$fr_2 \cdot \cos(\theta_{11} + \theta_{12,final}) - r_2 \cdot \cos(\theta_{11} + \theta_{12,initial}) - 200mm > 0 \tag{23}$$

(c) The third constraint is related to the maximum allowable space envelope that is a rectangle having a width of 300mm and a height of 100mm. The point A0 is fixed in space. The constraint about the initial position of the fixed point B0 is given by:

$$r_1 \cdot \sin(\theta_{11}) > -50mm \tag{24}$$

Constraints related to the initial and final position of point A to prevent collisions are:

$$r_2 \cdot \sin(\theta_{11} + \theta_{12,initial}) < 30mm \tag{25}$$

$$120mm > r_2 \cdot \sin(\theta_{11} + \theta_{12,final}) > 70mm \tag{26}$$

Constraints related to initial and final position of point B to prevent collisions are:

$$r_1 \cdot \sin(\theta_{11}) + r_4 \cdot \sin(\theta_{11} + \theta_{14,initial}) < 30mm \tag{27}$$

$$r_1 \cdot \cos(\theta_{11}) + r_4 \cdot \cos(\theta_{11} + \theta_{14,initial}) > -180mm \tag{28}$$

$$170mm > r_1 \cdot \sin(\theta_{11}) + r_4 \cdot \cos(\theta_{11} + \theta_{14,initial}) > 70mm \tag{29}$$

The upper and lower boundaries of the variables are given in Table 6.

Table 6.GA parameters used during optimization.

	1	2	3	4	5	6	7
	r_1 (mm)	r_2 (mm)	r_3 (mm)	r_4 (mm)	Q_{12} (deg)	Q_{11} (deg)	Δ_θ (deg)
Minimum	20	100	30	100	-65	180	-2.90
Maksimum	100	200	125	200	65	230	-1.60

At each iteration step of the optimization, Eq. (2-3) are used to find the unknowns, θ_{13}, θ_{14} then Eq. (9) and Eq. (10-12) are used to find the forces. The input variable θ_{12}, k at every iteration, k is calculated as:

$$\theta_{12,k} = \theta_{12,initial} + \Delta_\theta \cdot (k-1) \tag{30}$$

where k=2, 3…, 50.

Results: The computation time of the optimization is 637s (Core i7-4700HQ, 2.40GHz CPU) and the maximum required input torque is calculated as 24.48Nm (20% decrease with respect to the graphical synthesis). The parameters of the mechanism are found as in Table 7.

Table 7.Parameters of D1 after optimization

1	2	3	4	5	6	7
r_1 (mm)	r_2 (mm)	r_3 (mm)	r_4 (mm)	Q_{12}(deg)	Q_{11}(deg)	Δ_θ (deg)
42.2	119.89	36.57	139.39	-63.31	228.92	-2.40

An MSC ADAMS model is created to verify the calculation of the input torque as shown in Fig. 10. The error is found to be less than 0.0016%.

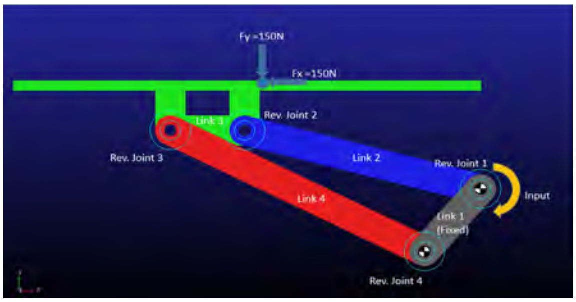

Figure 10. MSC ADAMS model of the optimized D1.

Optimization is also performed for D5 (not shown). Maximum input torque is selected as the selection criteria and it is found that maximum torque for D5 is 43% greater than D1, as shown in Figure 11. Therefore, for the door opening mechanism the best concept is D1.

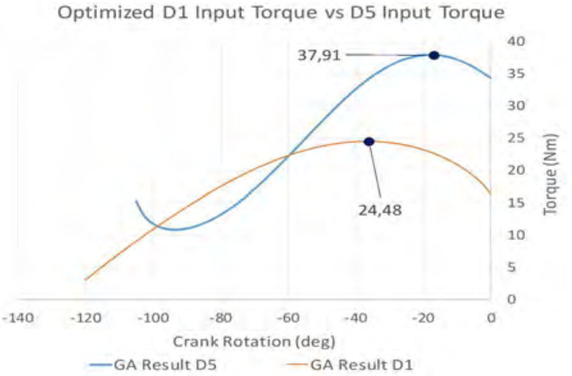

Figure 11. Input torques for the optimized D1 and D5 mechanisms versus the crank angle calculated using MSC ADAMS software.

Optimization of A1

The mechanism A1 is optimized based on the cost function and the constraints. In the optimization of A1, without loss of generality, D1 is used as the door opening/closing mechanism.

Variables: r1, r4, s0, θ_{11}, Δ_{stroke}. Δ_{stroke} is the stroke per step and the other variables are shown in Fig. 8.

Cost function: (a) The mechanism should be able to rotate the crank of the door opening/closing mechanism to the required degree, $(\Delta_{\theta_{12}})_{Design1}$, calculated before.

The first cost function is:

$$f(1) = abs(abs(\theta_{14,initial} - \theta_{14,final}) - (\Delta_{\theta_{12}})_{Design1})G \tag{31}$$

(b) In order to decrease the input force, the second cost function is defined as:

$$f(2) = \max(F_{actuator}) \cdot G \tag{32}$$

Constraints: (a) The first constraint is related to the transmission angle given as:

$$140° \geq \mu \geq 20° \tag{33}$$

(b) The second constraint is related to the space envelope defined as a rectangle with a width of 600mm and a height of 100mm. The pivot, A0, of the door opening mechanism is fixed in space and the following constraints are obtained:

$$r_1 \cdot \sin(\theta_{11}) < 300mm \tag{34}$$

$$r_1 \cdot \cos(\theta_{11}) < 170mm \tag{35}$$

$$s_{1,final} \cdot \sin(\theta_{11} + \theta_{12,final}) - r_1 \cdot \sin(\theta_{11}) < 45 \tag{36}$$

The upper and lower boundaries of the variables are shown in Table 8.

Table 8.Upper and lower boundaries of variables for A1.

	1	4	5	6	7
	r_1 (mm)	r_4 (mm)	s_0(mm)	Q_{11}(deg)	Δ_{stroke} (mm)
Minimum	50	30	50	50	1
Maksimum	300	130	250	200	3.2

At each iteration, θ_{13} and θ_{14} are found using Eq. (14-15) and the forces are found using Eq. (9) and Eq. (16-18). The input variable, $s_{1,k}$ is calculated at every iteration, k as:

$$s_{1,k} = s_0 + \Delta_{stroke} \cdot (k-1) \tag{37}$$

Where, k=2,3…,50.

Results: The computation time of the optimization is 193s (Core i7-4700HQ, 2.40GHz CPU) and the maximum required input force is found to be 313.18N (42% less than the graphical synthesis). The variables are found as in Table 9. Simulation of the synthesized mechanisms A1 and D1 in MS Excel are shown in Figure 12.

Table 9.Optimized variables of A1

1	2	3	4	5
r_1 (mm)	r_4 (mm)	s_0(mm)	Q_{11}(deg)	Δ_{stroke} (mm)
249.99	78.39	189.94	131.44	2.65

An MSC ADAMS model, shown in Fig. 13, is created to verify the calculation of the input force and the error is found to be less than 0.1%. Optimization is also performed for A3 and A8 (not shown). Power is used as the selection criteria since it is the determining factor for the size of the actuator so that it must be minimized to decrease the size and weight of the actuator. The other point is when power is used, mechanisms with linear actuators (A1, A3) and rotary actuators (A8) can be com-pared. The door opening time is assumed to be 5s and the required instantaneous power is calculated for the optimized A1, A3, and A8 mechanisms. The results are depicted in Fig. 14. A8 requires the highest power, whereas the power requirement of A1 and A3 are almost the same. To select the best alternative, simplicity and rigidity are considered as the evaluation criteria and A1 is selected as the best alternative.

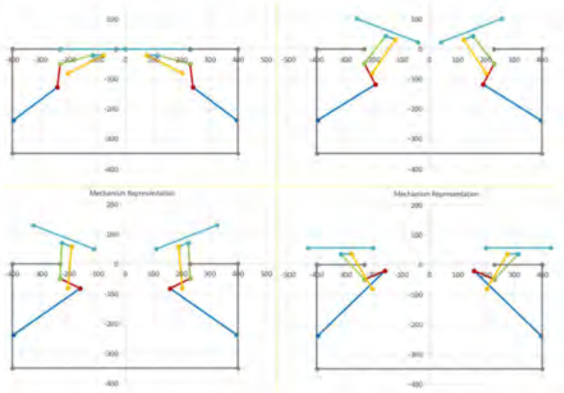

Figure 12. Simulation of concept A1 combined with D1 using MS Excel.

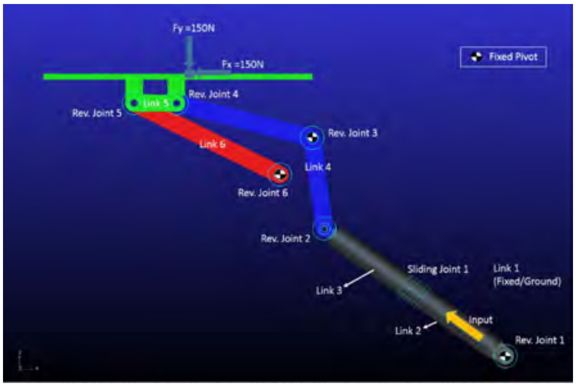

Figure 13. MSC ADAMS model of concept A1 and D1.

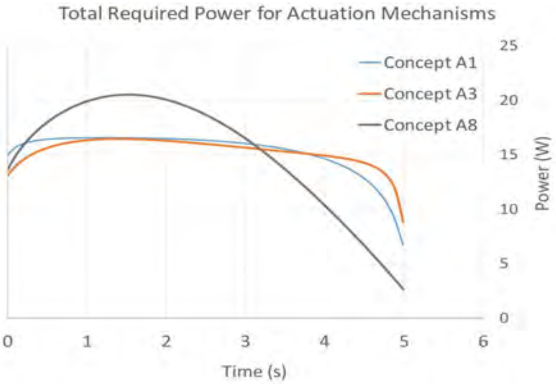

Figure 14. The required power versus time for the optimized A1, A3 and A8 mechanisms calculated with MSC ADAMS software.

DISCUSSION AND CONCLUSION

In this paper, the preliminary design of an in-flight refueling door actuation mechanism for flying boom type refueling system is presented. A systematic design methodology is followed. The main function is divided into two sub-functions:

door opening and actuation sub-functions. Different concepts are developed for each sub-function based on the requirements and constraints. A heuristic approach is used for evaluating the concepts based on the evaluation criteria. After the evaluation process, two concepts are selected for the door opening/closing mechanism, and three concepts are selected for the actuation mechanism. Kinematic synthesis for one concept for each sub-function is performed by using graphical methods to obtain suitable mechanisms. In addition, the obtained results are used to determine the upper and lower boundaries of design parameters for the optimization process. Thereafter, position analysis is executed by using Freudenstein's equation to check the motion of the synthesized mechanisms. Additionally, force analysis is performed to obtain the required actuation force and joint forces of the concepts. Finally, chosen concepts are optimized by using the multi-objective Genetic Algorithm. Before the optimization process, the lower and upper boundaries of design parameters, objective functions, and constraints are specified. Then, for each sub-problem concept, the optimization process is performed, and optimized concepts are compared with each other to select the best concept. In this study, Concept D1 and Concept A1 are chosen as the best concepts. After determining the best concepts for each sub-problem, these concepts are combined to obtain the preliminary design of the in-flight refueling door actuation system mechanism.

As a future work, aerodynamic analysis can be performed to estimate the external force more precisely. The effect of inertial forces can be taken into consideration in the force analysis. Based on the force analysis, detailed design of the mechanism can be performed, and a prototype can be built to validate the design.

NOMENCLATURE

Δ_θ : Angle per step of the Door Concepts
Δ_{stroke}: Stroke per step
r_i : Link Lengths
θ_{ij} : Link Angles
μ : Transmission Angle
T : Torque
F : Force
M : Moment

CONFLICT OF INTEREST

Authors approve that to the best of their knowledge, there is not any conflict of interest or common interest with an institution/organization or a person that may affect the review process of the paper.

AUTHOR CONTRIBUTION

All sections including conceptualisation, methodology, software, analysis, writing, review and editing were equally organised and performed by Hasan Akman, Ali Emre Turgut and Hakan Çalışkan.

REFERENCES

1. Aerial refueling. (2003, May 31). Wikipedia. https://en.wikipedia.org/wiki/Aerial_refueling
2. W. Alyafie, "Automatic Door System of Bus Door," 2012. [Online]. Available: https://www.slideshare.net/WaleedAlyafie/automatic-door-of-bus-door.
3. B. Baykus, E. Anli, and I. Ozkol, "Design and Kinematics Analysis of a Parallel Mechanism to be Utilized as a Luggage Door by an Analogy to a Four-Bar Mechanism," vol. 2011, no. April, pp. 411–421, 2011.
4. N. D. Thang, "Mechanism." [Online]. Available: https://www.youtube.com/user/thang010146/about.
5. J. Soss, "Hinge," US1484093A, 1924. Available: https://patents.google.com/patent/US1484093A/en
6. J. A. M. Eng, A. Toropov, and R. Ad, "Kinematics of Invisible Hinge," J. Appl. Mech. Eng., vol. 6, no. 4, pp. 4–11, 2017.
7. C. Lanni and M. Ceccarelli, "An Optimization Problem Algorithm for Kinematic Design of Mechanisms for Two-Finger Grippers," Open Mech. Eng. J., vol. 3, no. 1, pp. 49–62, 2009.
8. A. J. G. Nuttall and A. J. Klein Breteler, "Compliance Effects in a Parallel Jaw Gripper," Mech. Mach. Theory, vol. 38, no. 12, pp. 1509–1522, 2003.
9. G. N. Sandor and A. G. Erdman, "Advanced Mechanism Design", Volume 2., Prentice-Hall International, Inc., London, 1984, pp. 76–90.
10. L. G. Reifschneider, "Teaching Kinematic Synthesis of Linkages without Complex Mathematics," J. Ind. Technol., vol. 21, no. 4, pp. 17–32, 2005.
11. Akman H. (2019). A functional design methodology with genetic algorithm optimization to a door actuation mechanism. MS. Thesis, Middle East Technical University.
12. Dai, Xunhua, et al. "Hose-drum-unit Modeling and Control for Probe-and-drogue Autonomous Aerial Refueling." IEEE Transactions on Aerospace and Electronic Systems (2019).
13. Yin, Haipeng, et al. "Pilot-Induced Oscillation Analysis for Receiver in Flying-Boom Aerial Refueling via Mission-Oriented Evaluation." 2019 IEEE 10th International Conference on Mechanical and Aerospace Engineering (ICMAE). IEEE, 2019.
14. Wang, Qiansheng, et al. "Configuration Synthesis of Side Door Latch Power Release Mechanism." 2019 3rd International Conference on Electronic Information Technology and Computer Engineering (EITCE). IEEE, 2019.
15. Pedrammehr, Siamak, Mohammad Reza Chalak Qazani, and Saeid Nahavandi. "A novel axis symmetric parallel mechanism with coaxial actuated arms." 2018 4th International Conference on Control, Automation and Robotics (ICCAR). IEEE, 2018.
16. Freudenstein, F., and Maki, E. R. "The creation of mechanisms according to kinematic structure and function." Environment and Planning B: Planning and Design 6.4 (1979): 375-391.
17. Ding, Huafeng, et al. "Automatic structural synthesis of the whole family of planar 3-degrees of freedom closed loop mechanisms." Journal of Mechanisms and Robotics 5.4 (2013).
18. Yang, Wenjian, Huafeng Ding, and Andrés Kecskeméthy. "Automatic synthesis of plane kinematic chains with prismatic pairs and up to 14 links." Mechanism and Machine Theory 132 (2019): 236-247.
19. Chen, Dar-Zen, and Wei-Ming Pai. "A methodology for conceptual design of mechanisms by parsing design specifications." (2005):

1039-1044.

20. Kunjur, Arun, and Sundar Krishnamurty. "Genetic algorithms in mechanism synthesis." Journal of Applied Mechanisms and Robotics 4.2 (1997): 18-24.

21. Cabrera, J. A., A. Simon, and M. Prado. "Optimal synthesis of mechanisms with genetic algorithms." Mechanism and machine theory 37.10 (2002): 1165-1177.

Hittite Journal of Science and Engineering, 2022, 9 (1) 37–44
ISSN NUMBER: 2148–4171
DOI: 10.17350/HJSE19030000253

Headspace Gas Chromatography-Mass Spectroscopy Analysis and Antibacterial Tests of Commercial Hand Sanitizers

Simge Varlik[1] Gulsen Bayrak[2] Isik Percin Demircelik[2] Aybuke A. Isbir Turan[1]
[1]Turkish National Police Academy, Institute of Forensic Sciences, Ankara, Turkey
[2]Hacettepe University, Department of Biology, Ankara, Turkey

Article History:
Received: 2021/11/21
Accepted: 2022/03/16
Online: 2022/03/30

***Correspondence to**: Simge Varlik,*
Turkish National Police Academy, Institute of Forensic Sciences, Ankara, Turkey.
E-Mail: simgeakademi@gmail.com
Phone: +90 (505) 483 78 14
Fax:

ABSTRACT

As of late 2019, with the rapid and alarming spread of the SARS-Cov-2 (Covid-19) virus from the coronavirus family, serious measures had to be taken all over the world. The efforts to prevent this global epidemic have started with the legal measures taken by the countries in this regard and the warnings of the World Health Organization (WHO) that the epidemic should be taken seriously. In this process, the success of the use of masks and the use of alcohol-based hand sanitizer in preventing the disease has been evaluated and approved by scientists. In terms of the effectiveness of hand sanitizers, it is seen that the main components are ethyl alcohol and isopropyl alcohol, which are alcohol derivatives and they are considered as active ingredients due to their antibacterial and antiseptic effect . In this study, 11 commercially purchased hand sanitizer active and additional ingredients were identified and listed by headspace gas chromatography-mass spectroscopy (HS/GC-MS) and their antibacterial activities were studied. Hand sanitizers containing alcohol derivatives were used in the study. As a result of this study, it was observed that 4 out of 11 commercial hand sanitizers were not suitable for the final concentration values of hand sanitizer determined by the World Health Organization (accepted as 80%(v/v) for alcohol derivatives). Apart from this, hand sanitizers numbered 5 and 9 did not show antibacterial properties against *Escherichia coli* and hand sanitizers numbered 1 and 10 did not show antibacterial properties against *Staphylococcus aureus*. This situation shows that the standards of hand sanitizers should be controlled with much more stringent rules.

Keywords:
Alcohol; Antibacterial; GC-MS; Hand sanitizer; Headspace

INTRODUCTION

Hand hygiene is very important in reducing the incidence of infectious diseases. Considering that both respiratory and digestive system infections are transmitted through the mouth, it is inevitable that the microorganisms taken from the contact areas reach our respiratory and digestive systems with our hands. Studies have proven the effectiveness of hand sanitizers on microorganisms [1].

As of late 2019, it was necessary to take serious measures all over the world, as a result of the rapid spread of the SARS-Cov-2 (Covid-19) virus from the Coronavirus family. Within the scope of preventive measures, the World Health Organization (WHO) has reported that alcohol-based hand sanitizers have a very important role in preventing surface contamination. In addition to the antibacterial properties of alcohol-based hand sanitizers, its success in antiviral effectiveness has been evaluated and approved by scientists. In this sense, WHO has set some standards in 2010 in order to direct the production of commercial hand sanitizers around the world. These standards were revised and reorganized in 2020. Accordingly, the formulas containing ethanol and isopropyl alcohol after the preparation stages are shown in Table 1. It has been determined that hand sanitizers have an optimum effect at the specified concentrations [2].

Hand sanitizers containing ethanol and/or isopropanol cause less irritation and skin dryness compared to disinfection with soap and water, in addition to effectiveness of hand sanitizers on live pathogens. It is seen that the increase in the use of hand sanitizers, especially by healthcare workers, prevents the transmission of pathogens [3].

An alcohol-based hand sanitizer may contain one or more types of alcohol, with or without other excipients and moisturizers, to be applied to the hands to destroy microorganisms and temporarily stop their growth [4]

Table 1. Hand sanitizer final concentration formulas determined by WHO

FORMULA 1	FORMULA 2
Final concentration	**Final concentration**
Ethanol (80%)(v/v)	Isopropyl alcohol (75%)(v/v)
Glycerol (1.45%) (v/v)	Glycerol (1.45%) (v/v)
Hydrogen peroxide (0.125%) (v/v)	Hydrogen peroxide (0.125%) (v/v)

Globally, governments determine their own regulations regarding the volume fraction of alcohol in hand sanitizers, other ingredients to be added, and packaging and handling. The concentration of alcohol-containing hand sanitizers determined by WHO [5] has been accepted by many countries with legal regulations (Table 1). While ethanol or isopropyl alcohol, one of the active ingredients in the formulation, can be 75% or more by volume, an average of 80% is targeted. In addition, the US Food and Drug Administration (FDA) and the Canadian Ministry of Health made it necessary to add denaturants such as denatonium benzoate, sucrose octaacetate and isopropanol to the formulation in order for alcohol to lose its drinkable character [6].

Disinfectants with an alcohol concentration below 60% are not effective, but also pose a risk since they are not virulent [7]. The control of disinfectant contents in Turkey is within the scope of the "Biocidal Products Regulation" and is regulated by the "Regulation on the Usage Procedures and Principles of Biocidal Products" determined by the Ministry of Health. Biocidal products are defined as “active substances and preparations that contain one or more active ingredients, put on sale ready to use, have a controlling effect on any harmful organism chemically or biologically, or that limit its movement, remove, render it harmless, or destroy it”. Therefore, hand sanitizers are included in this group [8]. Moreover, within the scope of this regulation, the lists of approved chemicals that can be found in the content of the products have also been determined within this framework [8]

Headspace Gas Chromatography-Mass Spectroscopy

Pragst et al. (2001) published an article on the determination of ethyl esters in human hair due to chronic alcohol intake by GC-MS technique. Accordingly, it is possible to determine this ethyl ester and alcohol, since it can remain in the body for 24 hours after ingestion. In this way, alcoholic or social drinkers can be distinguished from each other and the causes of death can be clarified [9].

Bouche et al. (2002) studied the quantitative determination of n-propane, iso-butane and n-butane molecules taken into the body with lighter gas and passed into the blood by headspace GC-MS. Accordingly, they demonstrated that the headspace GC-MS technique is a sensitive, automated and fully validated technique [10]. Stambuli et al. (2004) developed a new analytical technique with headspace GC-MS (HS/GC-MS) for the determination of trace amounts of triacetone triperoxide (TATP) in post-explosion samples. According to this; have determined the optimum parameters and have determined TATP lower than 1 nanogram level [11]. Wang et al. (2008) published a review article on the advantages of HS/GC-MS gas chromatography. This article contains several examples of environmental, clinical, forensic, biological, food, powder and pharmaceutical analyzes between 2002 and 2008 [12]

Joshi et al. (2011) carried out the content determination of smokeless powder using HS/GC-MS. Nitroglycerin was determined as the main component, while 2,4-dinitrotoluene was detected at 44% [13]. Desharnais et al. (2012) used HS-GC-MS for cyanide detection in postmortem biological matrices. This method has been validated and used in forensic cases, burning victims and mass suicides [14]. Wu et al. (2012) conducted a study on the thermal decomposition of triacetone triperoxide (TATP), which is a potential explosive and can be easily synthesized under laboratory conditions, and used the GC-MS device in their study. As a result; They also proved from the GC-MS results that the synthesis of TATP with sulfuric acid would be more dangerous than the synthesis with hydrochloric acid, just as dangerous as TNT [15]. Almog et al. (2013) stated that this type of explosive, which is obtained from the combination of urea and nitric acid and looks like sugar, is used by terrorists. They used the GC-MS technique for the determination of trace amounts of urea nitrate from post-explosion debris during the attack. The aim of the study is to prevent the determination of urea and ammonium nitrate by acting as a nitronium cation when they come together, to prevent the formation of nitronium cation by creating a reaction step by including alko groups in the reaction and being able to easily determine urea nitrate from post-explosion debris with the help of GC-MS [16]. Lennert and Bridge (2018) carried out the determination and classification of smokeless gunpowder in their article using GC-MS technique. In this study, it is aimed to determine the smokeless gunpowder samples in the combustion or unburned residues after firing or explosion by GC-MS and DART-TOFMS techniques. According to this; Analysis of 34 smokeless gunpowder samples was made and it was stated that determination can be made with a fast visualization technique with GC-MS [17].

GC-MS device is a high selectivity, fast and sensitive device used to characterize alcohol and impure components. It is a preferred method because it is quantitatively reproducible, provides a database, and is easy to analyze [18]. For this reason, a chromatography device was preferred in this study.

HS/GC-MS method, which is used to detect alcohol from hand sanitizer samples, is a widely used method in recent years because it is used to detect volatile compounds in solid and liquid samples and mostly does not require any preliminary preparation [19]. The reason why it was preferred in this study is that it is considered as a suitable method for alcohol determination, and it responds in a short time and with high accuracy in solid-liquid phase compounds.

MATERIAL AND METHODS

HS/GC-MS Analysis

A total of 11 commercial hand sanitizers were used in this study. Hand sanitizers were chosen on the basis of being easily accessible and widespread. No price criteria were specified in the selection . They were purchased from accessible markets, pharmacies and e-shopping platforms, and provided between September-October 2020. No dilution with MeOH was made, as it may cause incorrect assessments of the amount of isopropyl alcohol/ethyl alcohol and the area covered by the amount of alcohol in the hand sanitizer will be determined (percent-%-v/v). 12 vials were prepared by absorbing 10 µL sample into each 20 mL autosampler vial with cellulose paper (One of the vials was a control sample. It is not shown in the table).

In this study, Agilent 5977B GC/MSD and Agilent 7697A Headspace Sampler in Forensic Chemistry Laboratories established within the Directorate of Forensic Sciences Institute of the Turkish National Police Academy were used. After making general adjustments with MSD-Mass Hunter program, comparisons were made with MSD Data Analysis and Quantitative Data Analysis methods. The parameters determined as a method in the GC-MS device are given in Table 2, Table 3 and Table 4 below.

Table 2 shows the values selected for the inlet parameters. Accordingly, the heater was kept at 250 °C for complete evaporation, the pressure was set to 10.121 psi, and the septum purge flow was set to 3 mL/min. Inlet mode is set to “Split” and split ratio is set to 50:1. The column flow was determined as 1.3 mL/min. Column pressure and constant flow are created automatically. Temperature values and durations are given in the table (Table 3) created for temperature parameters. The initial temperature was determined as 40 °C. In the next stage, it was increased up to 100 °C at 5 °C intervals. (from the 1st minute to the 15th minute, for 2 min) In the 2nd stage, it was increased up to 200 °C at 20 °C intervals (from the 15th minute to the 22nd minute for 2 minutes).

In the HS/GC-MS parameters (Table 4), the oven temperature, loop temperature, and transfer line temperature were set in increments of 10 °C, respectively (100 °C, 110 °C, 120 °C, respectively).

Table 2. Inlet Parameter for GC-MS

Heater	250
Pressure	10.121 psi
Total Flow	69.23 mL/min
Septum Purge Flow	3 mL/min
Inlet Mode	
Split Ratio	50:1
Split Flow	65 mL/min
Columns	
Flow	1.3 mL/min
Pressure	10.121 psi
Constant Flow	1.322 mL /min

Table 3. Temperature Parameter for HS/GC-MS

	Rate °C/min	**Value °C**	**Hold Time min**	**Run Time min**
(Initial)		40	1	1
Ramp 1	5	100	2	15
Ramp 2	20	200	2	22

Table 4. Headspace Parameter for HS/GC-MS

HS Parameter		
Name	**Setpoint**	**Actual**
Oven Temperature	100 °C	100 °C
Loop Temperature	110 °C	110 °C
Transfer Line Temperature	120 °C	120 °C
Vial Pressure	--	1.390 psi
Vial Flow	--	-0.02 mL/min
Carrier Pressure	External Supply	13. 595 psi

Antibacterial Experiment

In this study, antibacterial experiments were carried out in Molecular Biology Laboratory, Department of Biology, Hacettepe University, Beytepe, Ankara. The antibacterial properties of 11 hand sanitizer were examined by agar disk diffusion assay.

Staphylococcus aureus (*S. aureus*) is among the bacteria that is the most common cause of infection in skin surface damage [20]. *Escherichia coli* (*E. coli*), on the other hand, has become the most widely understood and studied microorganism in microbiology in terms of use, ease of production and durability, as well as being a very common microorganism [21] Since *E. coli* is Gram (-) and *S.aureus* is Gram (+) bacteria, the antimicrobial activity of hand sanitizers will be evaluated. Therefore, these two strains were considered sufficient in this study.

In this study *E. coli* (ATCC 25922) and *S. aureus* (ATCC 25923) were used as bacterial strains for the agar disk diffusion assay. First of all, *E. coli* and *S. aureus* were inoculated into 15mL LB (Luria Bertani) medium in order to obtain a bacterial cell suspension from bacterial strains and incubated for 24 hours at 37 °C. At the end of the incubation period, bacterial cell suspensions adjusted to 0.5 McFarland (1.5×10^8 CFU/mL) by diluted with PBS. 100 µL bacterial suspensions was taken and inoculated into LB agar plates. Whatman papers has been cut with the help of a 9 mm diameter cutter and sterilized under UV light. 100 µL commercial hand sanitizers were taken with sterile pipette tip and quickly soaked to sterile whatman papers and placed on LB agar plates. As the control, antibiotic discs containing 10 µg ampicillin were also placed on LB agar plates. Subsequently, LB agar plates were left to incubate for 24 hours at 37 °C and zone diameters were measured at the end of the incubation period [22].

RESULTS AND DISCUSSION

In this study, it was aimed to determine the active ingredients (ISA and/or ethanol as active ingredient) of 11 commercial hand sanitizers in terms of volume (% v/v) by HS/GC-MS; and aimed to investigate their antibacterial activities. The amounts of alcohol, which are the active ingredients of the samples, were verified and it was determined whether they reached the limits set by WHO (75% for isopropyl alcohol (ISA), 80% for ethyl alcohol according to the World Health Organization). In addition, its antibacterial properties have been demonstrated using two bacterial strains (Gram-negative *E. coli* and Gram-positive *S. aureus*, were selected) Since there are samples in which isopropyl alcohol and/or ethanol are used together in the hand sanitizer content, the total amount of alcohol was determined and the limit value was accepted as 80% alcohol by volume [6]. According to the analysis, it was seen that the amount of isopropyl alcohol/ethanol in the hand sanitizers differs and 7 of them are above the 80% (v/v) value determined by the World Health Organization (WHO).

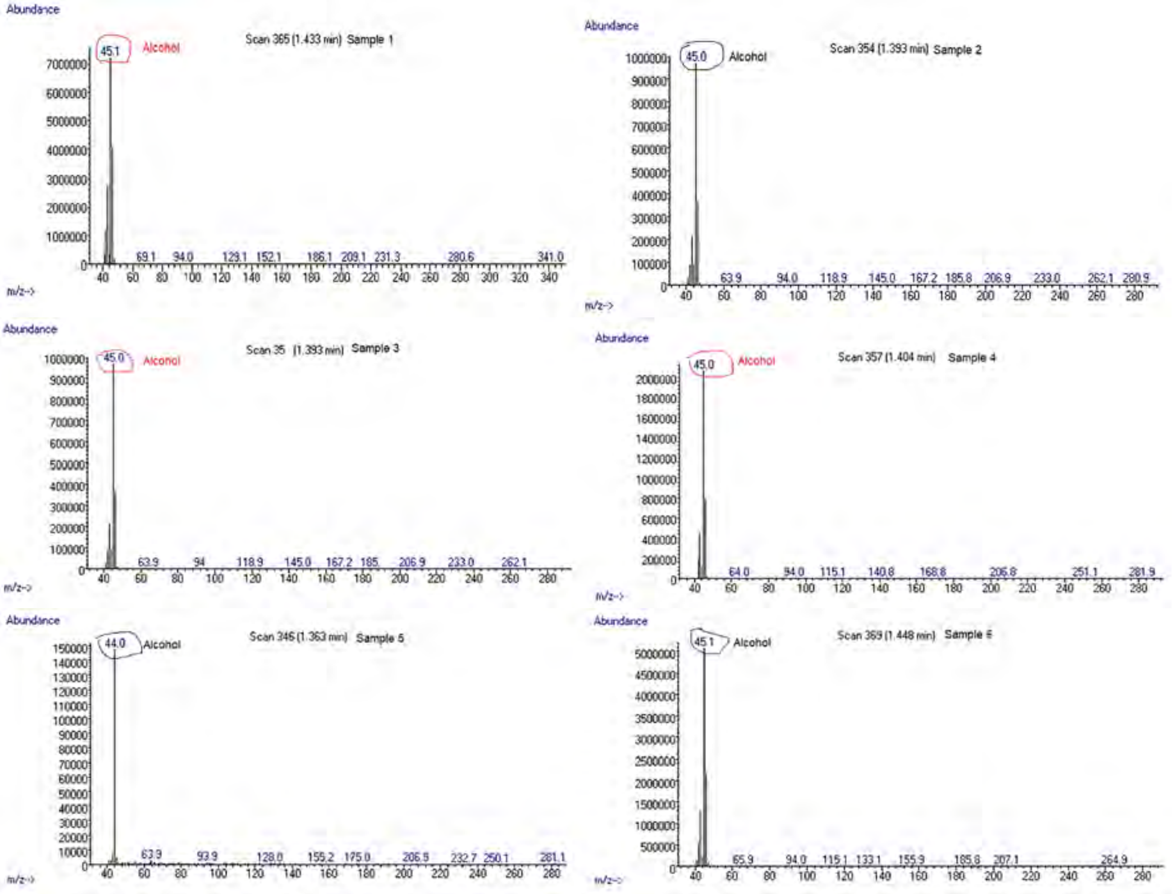

Figure 1. HS/GC-MS chromatograms and alcohol (ISA/ethanol) peaks of samples (S1-11)

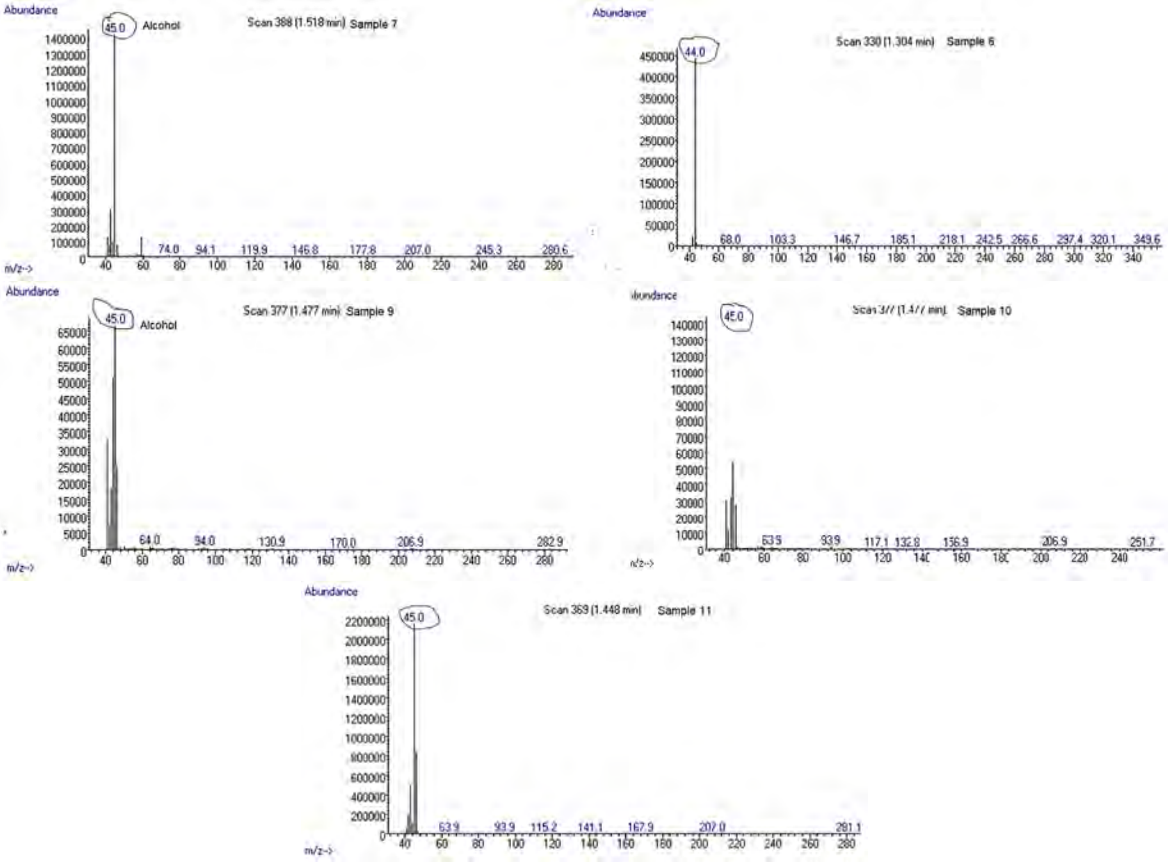

Figure 1. Continued.

The active ingredients in hand sanitizers usually destroy microorganisms. Also, inactive ingredients are added to disinfectants for reasons such as adding fragrance, protecting the health of the applied skin, and adjusting the disinfectant viscosity. Table 5 contains information on the active ingredients (alcohol derivatives) and additional ingredients found in commercial hand sanitizers. While ethanol and isopropyl alcohol are used as active ingredients in the samples, water, carbomer, glycerin, fragrance agent etc. are frequently used as additional ingredients [8].

Also, HS/GC-MS chromatograms and active ingredient (ISA-ethanol) peaks of 11 hand sanitizer samples are shown (Figure 1). Quantifer ion (m/z) of ethanol and isopropyl alcohol has a peak value of 45 [23]. In this context, it was shown that each example has had the active compound.

It has shown the retention time, percentage volume and match factor values of the total alcohol (isopropyl alcohol and/or ethanol) amounts obtained as a result of GC-MS/HS analyzes of commercial hand sanitizers for 11 samples (control group is not reflected in the table) in Table 5. The shown variables represent the ethyl alcohol/isopropyl alcohol ratio component (% v/v) based on data scanned in the SWGDRUG 3.5.L Library. Retention time (Rt, min) has shown the retention time of the substance, match factor (MF) shows the match rate in the library. Measurements were made 3 times and the average of the volumetric area and Match Factor (MF) values were reflected in the table (Table 6).

Based on the data in the Table 6, a graph was created including the percentage amounts of alcohol in the total mixture and standard deviation values. SSR and SSReg values were obtained by calculating the ANOVA (One-way analysis of variance, $P < 0.05$) (Figure 2). According to the value, difference between the observations and the predicted values are small and unbiased.

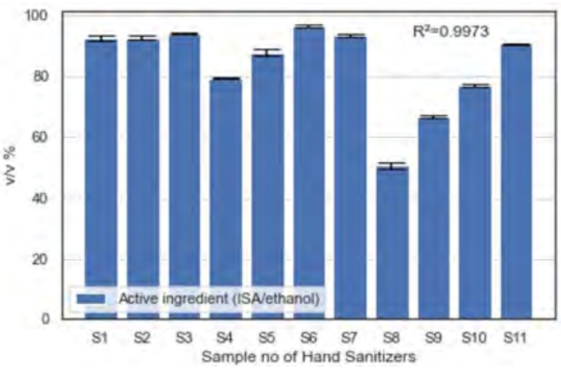

Figure 2. Alcohol amounts obtained as a result of HS/GC-MS Analysis of commercial hand sanitizers (ISA and ethanol, v/v%)

Table 5. Active ingredient (alcohol derivative) and additional ingredient information of hand sanitizer samples

Sample No	Active Ingredient (alcohol derivative)	Additional Ingredient
S1	Ethanol	water, carbomer, glyserin, triethanolamine
S2	Ethanol	water, carbomer, glyserin, fragrance agent
S3	Isopropyl Alcohol	water, butane-1.3-diol, lanolinpoly (oxyethylene)-75, fragnance
S4	Isopropyl Alcohol	water, butane, isobutane, propane, tocopheryl acetate, benzalkonium chloride, panthenol, glyserin
S5	Isopropyl Alcohol	water, lanolinpoly (oxyethlyene)-75, fragnance
S6	Isopropyl Alcohol	water, carbomer, chlorhexidine digluconate, fragnance, glycerin, *Aloe barbadensis*, clay, sodium hydroxide
S7	Isopropyl Alcohol	water, glycerin, purified water, fragnance
S8	Isopropyl Alcohol	water, ,glycerin, polysobate 20,carbomer,triethanolamine, fragnance
S9	Isopropyl Alcohol	water, butylene glycol, carbomer, triethanolamine, perfume, polysorbate 60, DL-Panthenol
S10	Isopropyl Alcohol	purified water, fragnance
S11	Isopropyl Alcohol	glycerin, hydrogen peroxide, purified water USP

Table 6. Total alcohol (v/v%) obtained as a result of GC-MS/HS Analysis of commercial hand sanitizers (isopropyl alcohol and/or ethyl alcohol)

Sample	Rt (min)	Area% (v/v)	MF (Match Factor)
S1	1.444	92.51	84,6
S2	1.428	92.63	81.5
S3	1.428	94.01	80.3
S4	1.421	79.26	82.5
S5	1.421	87.70	82.3
S6	1.428	96.28	85.7
S7	1.419	93.36	81.0
S8	1.426	50,36	94.3
S9	1.430	66.48	83.0
S10	1.426	76.70	83.1
S11	1.428	90.50	82.2

Table 7. Agar disc diffusion assay results for antibacterial properties of hand sanitizers (zone diameters, mm)

Bacterial strain	Ampicillindisc (10µg)	S1	S2	S3	S4	S5	S6	S7	S8	S9	S10	S11
S. aureus	19	0	15	14	11	12.5	17	13	14	15	0	12
E. coli	19	12	19	11	15	0	13	15	11	0	14	15

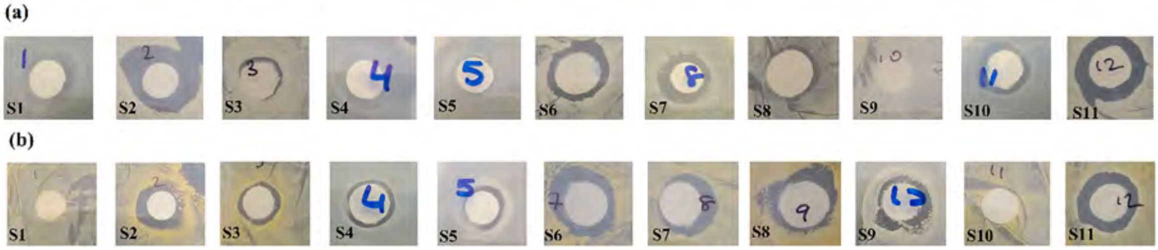

Figure 3. Inhibition zone of sample 1 to 11 for (a) *E. coli* and (b) *S. aureus.* (For all samples, sample numbers of were given at the bottom of left corner. Apart from this, the numbers written with acetate pen on the figures do not reflect the figure numbers).

The antibacterial properties of hand sanitizers were evaluated with the agar disc diffusion assay. Agar disc diffusion assay results were given in Table 7 also zone inhibition of hand sanitizers was given in Figure 3. Based on the results, it was seen that sample 5(S5) and sample 9(S9) were not shown antibacterial properties against *E. coli.* It was seen that S1 and S10 were not shown antibacterial properties against *S. aureus.* By looking at the formed zone diameters, it was concluded that the antibacterial properties of S6 and S2 were high for both *S. aureus* and *E. coli.* It was determined that there was plant content (*Aloe barbadensis*) in the S6 sample both in the label information and as a result of the analysis (Table 5). In a study on the antibacterial effect of *Aloe barbadensis*, it has been shown that the antibacterial effect was stronger against both gram-positive and gram-negative bacteria at different concentration levels in samples using *Aloe barbadensis*, compared to those not used [24]. In this context, it can be said that plant agent (*Aloe barbadensis*) increases the antibacterial activity in S6. Likewise, it can be said that the fragrance agent found in S2 (fragrance could not be detected in HS/GC-MS) may be a herbal ingredient that increases antibacterial activity.

It has been stated from company that S5 was effective for *E. coli* (NCTC 1038) strain and *S. aureus* (ATCC6538) strain. However, the zone diameter was formed only for S. *aureus.* In our study, non-resistant bacterial strain *E. coli* (ATCC 25922) was used however, in all repeated agar disc diffusion assays, no zone diameters were formed for S5 in *E. coli.*

It was stated that S11 had antibacterial properties for *E. coli* (ATCC10536) and *S. aureus* (ATCC6538). From the results of the agar disc diffusion assay S11 has created zone against both *E. coli* (ATCC 25922) and *S. aureus* (ATCC 25923) strains. It was expected from hand sanitizers to show their antibacterial properties the shortest possible time and in the most effective way [25]. Based on this information, it is expected that the effects of sanitizers against bacteria strains in agar plates have been observed before the alcohol has evaporated.

Also, According to Table 5 about contents of hand sanitizers, it was seen that samples had contained ethanol or isopropyl alcohol as the main antibacterial agent. As a result of the repeated zone inhibition experiments, the inhibition zone has not been seen in S1-S10 for *S. aureus*, and S5-S9 for *E. coli.* It was possible that the bacterial concentration was intense, so these hand sanitizers could not show the antibacterial effect. Since the same protocol was applied for all samples in the experiment, equal bacterial concentration was cultivated and zone inhibition experiments with diluted bacterial concentration were not repeated for these samples.

CONCLUSION

The use of hand sanitizers, which became widespread with the Covid pandemic, has aroused our curiosity about how much antibacterial effect they have shown. First of all, the alcohol content of hand sanitizers was investigated by HS/GC-MS analysis and their antibacterial activity were investigated on *S. aureus*, one of the most common disease-causing bacteria, and *E. coli*, one of the most frequently studied strains. Then, by these strains the zone inhibition experiments were performed.

As a result of this study, it was seen that S4 out of S11 commercial hand sanitizers were not suitable for the final concentration values of hand sanitizers determined by the World Health Organization (accepted as 80%(v/v) for alcohol derivatives). Apart from this, it has been seen that S5 and S9 did not show antibacterial properties against *E. coli*, S1 and also, sample S10 did not show antibacterial properties against *S.aureus*. This results have showed that the control of the standards of hand sanitizers should be controlled with much more stringent rules. The present study needs to be supported by more samples of hand sanitizers.

CONFLICT OF INTEREST

Authors approve that to the best of their knowledge, there is not any conflict of interest or common interest with an institution/organization or a person that may affect the the review process of the paper.

AUTHOR CONTRIBUTION

Aybuke A. Isbir Turan and Simge Varlik worked with GC-MS analysis data. Isik Percin Demircelik and Gulsen Bayrak performed antibacterial analyzes. Gulsen Bayrak and Simge Varlik revised the article. All authors contributed to the finalization of the article.

References

1. Gold NA, Mirza TM, Avva U. Alcohol sanitizer. StatPearls Publishing. Treasure Island (FL) (2020).
2. Nyamwweya NN, Abuga KO. Alcohol-based hand sanitizers - A multidimensional perspective. Preprints. (2020).
3. Hilburn J, Hammond BS, Fendler EJ, Groziak PA. Use of alcohol hand sanitizer as an infection control strategy in an acute care facility. American Journal of Infection Control 31(2) (2003) 109-116.
4. Jing JLJ, Pei YIT, Bose RJC, McCarthy JR, Tharmalingam N, Madheswaran T. Hand sanitizers: a review on formulation aspects, adverse effects, and regulations. International Journal of Environmental Research and Public Health. 17(9) (2020) 3326.
5. WHO. Guide to local production: WHO-recommended handrub formulations (PDF). April (2010). Retrieved 27 February 2020.
6. Thomson E, Bullied A. Production of ethanol-based hand sanitizer in breweries during the COVID-19 crisis, Technical Quarterly 57 (2020) 47-52.
7. WHO. Guidelines on hand hygiene in health care, Part I, Chapter 10, pp.28, 2019.
8. Regulation on the usage procedures and principles of biocidal products, Regulation Number 30821, Official Gazette, July 4, 2019. https://www.resmigazete.gov.tr/eskiler/2019/07/20190704-2.htm
9. Pragst F, Auwaerter V, Sporkert F, Spiegel K. Analysis of fatty acid ethyl esters in hair as possible markers of chronically elevated alcohol consumption by headspace solid-phase microextraction (HS-SPME) and gas chromatography-mass spectrometry (GC-MS). Forensic Science International 121(1-2) (2001) 76-88 .
10. Bouche MP, Lambert WE, Van Bocxlaer JF, Piette MH, De Leenheer AP. Quantitative determination of n-propane, isobutane and n-butane by headspace GC-MS in intoxications by inhalation of lighter fluid. Journal of Analytical Toxicology 26 (2002) 35-42.
11. Stambouli A, El Bouri A, Bouayoun T, Bellimam MA. Headspace-GC/MS detection of TATP traces in post-explosion debris, Forensic Science International 146 (2004) 191-194.
12. Wang Y, McCaffrey J, Norwood DL. Recent advances in headspace gas chromatography. Journal of Liquid Chromatography Related Technologies 31 (2008) 1823-1851.
13. Joshi M, Rigsby K, Almirall JR. Analysis of the headspace composition of smokeless powders using GC-MS, GC-μECD and ion mobility spectrometry. Forensic Science International 208 (2011) 29-36.
14. Desharnais B. Huppé G. Lamarche M, Mireault P, Skinner CD. Cyanide quantification in post-mortem biological matrices by headspace GC-MS. Forensic Science International 222 (1-3) (2012) 346-351.
15. Wu SH, Chi JH, Wu YT, Huang YH, Chu FJ, Horng JJ. Thermal hazard analysis of triacetone triperoxide (TATP) by DSC and GC/MS. Journal of Loss Prevention in the Process Industries 25(2012) 1069-1074.
16. Almog J, Espino D, Tamiri T, Sonenfeld D. Trace analysis of urea nitrate in post-blast debris by GC/MS. Forensic Science International 224 (2013) 80-83.
17. Lennert E, Bridge C. Analysis and classification of smokeless powders by GC-MS and DART-TOFMS. Forensic Science

International 292 (2018) 11-22.

18. Bedner M, Murray J, Urbas AA, MacCrehan WA, Wilson, WB. Comparison of measurement methods for alcohol-based hand sanitizers, NIST Interagency/Internal Report (NISTIR), National Institute of Standards and Technology, Gaithersburg, 2021.
19. Topçu G, Barla A, Gören AC, Bilsel G, Tümen G. Analysis of the essential oil composition of Sideritis albiflora using direct thermal desorption and headspace GC-MS techniques. Turkish Journal of Chemistry , 29 (2005) 525- 529.
20. Zhao X, Guo B, Wu H, et al. Injectable antibacterial conductive nanocomposite cryogels with rapid shape recovery for noncompressible hemorrhage and wound healing. Nature Communications 9 (2018) 2784.
21. Blount ZD. The natural history of model organisms: the unexhausted potential of E. coli. Microbiology and Infectious Disease. eLife (2015) 1-12.
22. Özkahraman B, Tamahkar E, İdil N, Kılıç-Suloglu A, Perçin, I. Evaluation of hyaluronic acid nanoparticle embedded chitosan–gelatin hydrogels for antibiotic release. Drug Development Research (2020).
23. Abrigo, N., Ruzicka, C., Faustino, P. et al. Development and validation of a headspace GC-MS method to evaluate the interconversion of impurities and the product quality of liquid hand sanitizers. AAPS Open 8 (1) (2022) 1-13.
24. Das S, Das A, Bhavya T, Rama Nivashini S. Molecular characterisation and antibacterial activity of Aloe barbadensis miller on textiles. The Journal of the Textile Institute (2019) 1-7.
25. Traoré O, Allaert FA, Fournet-Fayard S, Verrière JL, Laveran H. Comparison of in-vivo antibacterial activity of two skin disinfection procedures for insertion of peripheral catheters: Povidone iodine versus chlorhexidine. Journal of Hospital Infection 44(2) (2000) 147-150.

Hittite Journal of Science and Engineering, 2022, 9 (1) 45–56
ISSN NUMBER: 2148–4171
DOI: 10.17350/HJSE19030000254

Investigation of the Interaction of the Tank Structures Exposed To Earthquake with the Soil

Asuman Isil Carhoglu
Suleyman Demirel University, Department of Civil Engineering, Isparta, Turkey

Article History:
Received: 2021/11/19
Accepted: 2022/02/28
Online: 2022/03/30

***Correspondence to**: Asuman Işıl Çarhoğlu, Suleyman Demirel University, Civil Engineering, Isparta, TURKEY*
E-Mail: isilcarhoglu@sdu.edu.tr
Phone: +90 246 211 12 15

ABSTRACT

Liquid storage tanks storing liquids such as gasoline and LNG are very important structures. These tructures can be damaged because of the loss of strength that may occur due to external influences. It is known that a considerable amount of damage occurred in tank structures, which are one of the industrial structures, happened during the earthquakes occurred in the past. Determining the behavior of the buildings which are under the effect of an earthquake is very important in order to prevent damage to the building during a possible earthquake. The behavior of structures built on soft soils is considerably different from that of structures constructed on a rigid soil. For this purpose, in this study, a steel tank structure was modeled by considering the different soil profiles. During modelling, an elastic spring method was used for the soil while the finite element method was used for the tank and the basic interaction of the soil and foundation structure which are exposed to earthquake loads were examined. Dynamic analyzes were carried out using the time history method by taking into consideration 11 earthquake records having the different properties. According to the results of the displacement and stress values obtained; It was observed that the values obtained in the earthquakes, whose peak ground acceleration and ground velocity are large, are higher than other earthquakes. It was seen that as the soil resistance increases, the strength of the structure increases during earthquakes.

Keywords:
The structure-soil-interaction; Liquid storage tank structures; Time history analysis; Earthquake; Spring stiffness

INTRODUCTION

Earthquakes with different characteristics have occurred all over the world for years and cause loss of life and property. Some of the largest earthquakes in the world are 1995 Kobe earthquake, 1906 San Francisco Earthquake (M = 7.9), 1989 Loma Prieta (M = 6.9), 2018 Anchorage Alaska Earthquake (M = 7.1), 2014 South Napa, California Earthquake (M = 6.0) and 2004 Northern Sumatra (M = 9.0) [1]. Up until today, many devastating earthquakes have occurred in Turkey located on an active fault line. Some of these earthquakes are 1998 Adana Ceyhan Earthquake (M_w= 6.3), 1999 Kocaeli Earthquake (M_w = 7.4), 1999 Düzce Earthquake (M_w = 7.2), 2002 Afyon-Sultandağı Earthquake ((M_w = 6.3), 2003 Bingöl Earthquake (M_w = 6.4) and 2011 Van Earthquake (M_w = 6.3) [2]. The magnitude of Kocaeli earthquake was 7.4 and it occurred at an area which was quite busy in terms of industry. This earthquake occurred in the North Anatolian fault which has a length of 1500 km and its depth of focus in the southeast of Izmit is 7 km, its depth of focus in the east of Istanbul is 80 km [1,3,4]. This strong earthquake caused great damage at Tüpraş refinery in Izmit. Many Naptha tanks were damaged in Tüpraş refinery, and 2 elevated liquid oxygen tanks collapsed at the Habas plant [3].

It is important for earthquake engineering to examine the fluid-structure-soil interaction of structures such as off-shore, suspension bridges and liquid storage tanks. The interaction of liquid-structure-soil shows variation depending on the features of the structures. For this reason, it is necessary to model such structures correctly. The liquid storage tank is widely used in industry and nuclear plants for the purpose of storing different liquids such as oil and liquefied natural gas [5]. Liquid storage tanks are exposed to earthquakes. The rigidity of the tank structures will decrease due to the low strength values that will occur in the soils during the earthquake. Therefore, it is of great importance to examine the soil structure interaction since substantial damages will occur in the structures. When the past earthquakes are analyzed, it is observed that shell buckling occurs in structures built on a flexible foundation. It is seen that the effect of the foundation in tank structures exposed to the earthquake is of great significance and it is necessary to examine the soil structure interaction. Inertia forces may occur in the system of the liquid structure system due to seismic effects forming on the bottom of the tank during the earthquake [6].

The Structure-soil interaction is known as the effect of the movements occuring in the soil due to the structure and the effect of the movement occuring in the structure due to soil as a result of the effects such as earthquakes. Kinematic and inertial interaction are involved in structure-soil interaction. Horizontal and vertical displacements occur on the soil during an earthquake. If the foundation is very rigid, kinematic interaction occurs when the ground motion will be prevented by changing the properties of the wave motion on the soil [7]. When examining the seismic performance in the buildings, it is seen that one of the most important factors related to the extension of the building period is rotation that occurs in the foundation [8,9]. The effects such as collapse and rotation occurring in the soil are ignored by assuming with the fixed base in the analysis performed for the purpose of determining the behavior of the structures exposed to the earthquakes. However, since the rigidities of soft soil are less than the hard soil, the periods of constructions built on the soft soil are longer than those of the hard soil. As the soil stiffness decreases, the structure period increases and therefore the great changes happen in the values such as deformation, displacement, base shear force and stress occuring in the structure.

Mezaini M. determined the design forces to be formed in the cylindrical tank were determined by using the SAP 2000 Program by taking account of the different soil conditions and foundation geometry. When the results were examined, it was seen that there were differences in the design forces [10]. Kianoush [5] performed the analyses by modeling as shallow and tall with the finite elements method the concrete rectangular tank structure exposed to the four ground motions in order to examine the liquid structure interaction. The base shear, moment and sloshing values were determined and compared by depending on the frequency properties of earthquakes for different soil situations [5]. Bhattacharya [11] investigated the changes in the system of the structure-soilfoundation with the increasing of the lateral natural period by considering the concrete frame structures with the different span and height. Soils with different features were designed using an elastic spring model. The changes in the values of the natural period and base shear force were examined [11]. Dutta [12] made analyses as elastic and inelastic for frame structures in low-rise different features by modelling as elastic spring the soil for the purpose of examining the soil-structure-interaction. Ghandil [13] obtained the values of the lateral displacement and the story shear force by considering nonlinear soil-structure interaction analysis of structures with different floor numbers by taking account of the different soil properties. Elasto-plastic Mohr-Coulomb model were used ELM and NFM methods during soil modeling. Meng [14] compared the values of the natural frequencies, displacement, base shear force and overturning moment of the liquid storage tanks to obtain their soil-structure interaction [14]. Dutta[15] examined the soil-structure interaction for the elevated tank structures. Zhao [16] was performed the earthquake analysis by designing a steel nuclear power plant structure with the finite element method. Time history analysis method was made in the analyzes. Dynamic analyzes were made by considering different baffle types, heights and lengths of the structure. Analyzes were performed for Kobe and El Centro earthquakes for 0, 0.2, 0.6, 0.9 and 1 height ratios of the nuclear plant. The maximum acceleration values at the top of the tank for earthquake conditions are determined according to the different height ratio. However, the comparisons were made by obtaining the displacement and stress values. Zhao [17] examined the seismic analysis of tank structures. An Arbitrary Lagrangian Eulerian (ALE) algorithm has been used to examine the liquid structure interaction. The ratio of water height to tank height and the ratio of water mass to total mass parameters are taken into account. Pressure, stress, frequency and overturning moment values of water are obtained and compared. Nicolici [18] were designed the liquid-filled containers in order to examine liquid structure interaction. Time history analysis was performed to examine the interaction between the tank wall and the liquid. The liquid effect is modeled by the mass spring method. A bidirectional FSI approach was used to examine the effect on the wall due to the water effect. In the analysis results, the values of impulsive, convective pressure, the wave height of liquid and base reaction are determined and examined. Patel [19] examined in the dynamic interaction of the fluid-structure-soil. The interaction of the fluid-structure studied by using the added mass approach of Westergaard. The fluid in the tank was dealt with as water. Hard, medium and soft soils was utilized as soil profiles by examining the interaction structure-fluid-soil. Soil was modelled as spring. In the results of the time history analysis, The values of the displacement and base shear force were obtained and compared. Seleemah [20] were performed the seismic analysis of the isolated tanks by using 3D-BASIS-ME, SAP2000 programs. Tank structures were modeled as shell element. The convective mass of the liquid and rigid mass was located in the center of tank and base of tank respectively and link element indicating rigidity was settled in the horizontal direction by modelling fluid. The values of the displacement obtained from isolated tanks were compared by using 3D-BASİS-ME and SAP 2000 programs. Livaoğlu [21] examined in interaction of the fluid-structure-soil by utilizing the mechanical and finite element methods for ten tank structures on the different soil features. The values of base shear, displacement and overturning moment were obtained. Livaoğlu [22] carried out the seismic behaviour of the structure of elevated tank on different soils. The fluid in the tank was modeled with spring mass model belonging to Housner. Impulsive mass and convective mass were used for added mass approach. These masses were attached to the finite element. The water was dealt with as the fluid in the container. According to the analysis results, it was seen that the important changes in the earthquake behavior of tanks occured depending on the soil properties. At the same time, it was determined that the displacement and impulsive modes were more bigger than torsional modes.

In this study, The behavior of a tank structure under the effect of earthquake was investigated. For this reason, A tank structure and soil were designed by assuming different soil properties. The selected soil properties have different mechanic properties and the soil was designed with the equivalent elastic spring method [23]. Lineer time history analyses were performed with Sap 2000 by addressing eleven ground motion records [24].

IDEALIZATION OF THE LIQUID STORAGE TANK-SOIL SYSTEM

Idealization of The Liquid Storage Tank System

Determining the behaviors of buildings exposed to earthquake effects is an issue that should be addressed in terms of earthquake engineering. Since the seismic behaviour of tank structure is studied by taking into consideration the soil-structure interaction, the liquid storage tank have been designed as shell element through the use of SAP 2000 Programme [24]. The tank structure, with radius of 20 m and height of 14 m, was designed as shell. The elasticity module of the tank steel was measured as 2.1 10^{11} N/m^2, the unit volume weight was 7.69 kg / m^3, and the unit volume weight of the liquid was 807.9 kg/ m^3 [25]. The three-dimensional view of the tank is shown in Fig. 1.

The liquid in the tank is modeled using a mass-spring system. According to the Housner mass-spring system; The total mass of the liquid in a tank exposed to the earthquake is divided into two as M_o and M_1. A part of the liquid moves together with the tank wall during the earthquake as the tank walls move. This mass, called M_o, is rigidly connected to the tank wall at the h_0 height, as shown in Fig. 1. Oscillations occur in the rest of the water due to the movement of the tank wall, and this oscillating force is shown as M_1. Oscillating M_1 mass is attached to the tank walls with the help of a spring. In this way, hydrodynamic pressure forces are created by using the mass-spring model. In equation 1-5, R: The radius of the cylindrical tank, h: the water depth of the cylindrical tank, M: total mass, M_0: the mass at the ho height, M_1: the mass at the h_1 height. M_0 impulsive mass and M_1 sloshing mass are obtained from Equations 1 and 2. The values of h_0 and h_1 are found by Equations 3 and 4 in order to determine the dynamic pressure forces. The spring constant that connects the sloshing mass to the tank wall is obtained by Equation 5 [26, 27, 28].

$$M_0 = M\frac{\tanh 1.7R/h}{1.7R/h} \tag{1}$$

$$M_1 = M(0.6)\frac{\tanh 1.8h/R}{1.8h/R} \tag{2}$$

$$h_0 = \tfrac{3}{8}h\left\{1+\propto\left[\tfrac{M}{M_1}\left(\tfrac{R}{h}\right)^2-1\right]\right\} \tag{3}$$

$$h_1 = h\begin{bmatrix} 1-0.185\left(\dfrac{M}{M_1}\right)\left(\dfrac{R}{h}\right)^2 \\ -0.56\beta\dfrac{R}{h}\sqrt{\left(\dfrac{MR}{3M_1h}\right)^2-1} \end{bmatrix} \tag{4}$$

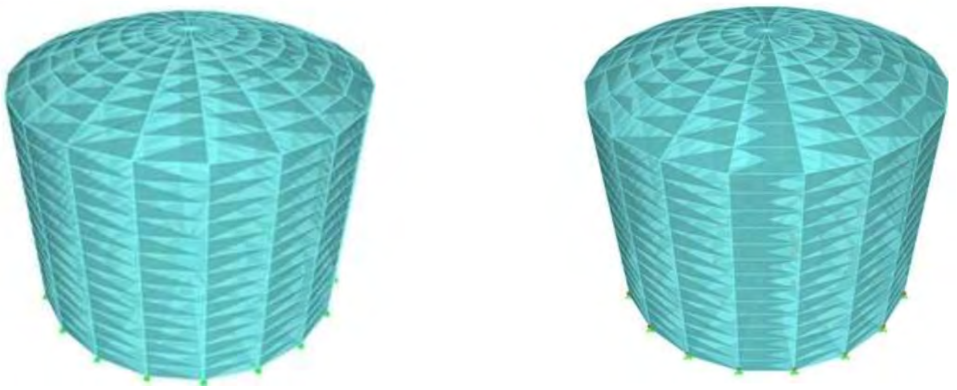

a) The structure with fixed support.

b) The structure that the soil is spring.

Figure 1. The view of the steel tank structure.

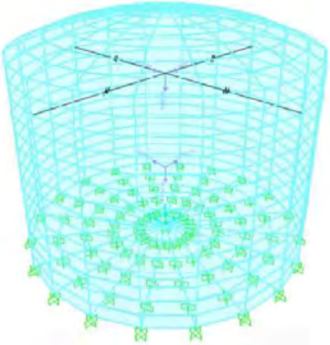

Figure 2. The structure of tank and mass-spring system of the fluid.

$$k_1 = 5.4\frac{M_1^2}{M}\frac{gh}{R^2} \tag{5}$$

Tank structure and the fluid in the tank are shown in Fig. 2. Impulsive mass and sloshing mass are determined by using Equation 1 and Equation 2. These masses are located in the h_1 and h_2 heights. The springs showing rigidity are connected to the tank wall. The spring constant connecting the sloshing mass to the tank wall is obtained by Equation 5 [26, 27, 28].

Idealization of Soil Model

The soil, foundation and structure are taken into consideration in order to examine the soil-structure-interaction. Equation of motion for cylindrical foundations is shown in Equation 6. $X, \dot{X}, \ddot{X}, m, c, k$ show displacement, velocity, acceleration, mass, effective damping and stiffness respectively. Determining the impedance function K(w) of a rigid massless foundation is important in terms of studies regarding structure soil interactions. The harmonic and steady state response of a foundation, with a mass of zero, was founded. Dynamic impedance is known as the ratio between steady state force and displacement [23].

Dynamic impedance is shown in Equation 7. That is to say;

$$m\ddot{x} + c\dot{x} + kx = P(t) \tag{6}$$

$$K_v = \frac{R_v(t)}{v(t)} \tag{7}$$

In which; $R_v(t)$ is harmonic vertical force, $v(t)$: harmonic settlement of the foundation.

The dynamic force and displacement that occurs at the system exposed to the harmonic loads. Equation 7 is divided into two components and one of them is in the phase, another of them is 90 out of phase.

$$K_a(\omega) = K_{a1}(\omega) + iK_{a2}(\omega) \qquad A = v, h, r, h_r, t; i = \sqrt{-1} \tag{8}$$

In Equation 8, these real and imaginary components are functions of vibration frequency. Real components depend on the stiffness and inertia of soil. Imaginery components depend on radiation and damping of material.

Harmonic excitation;

$$P(t) = P_0 \exp(i\omega t) \tag{9}$$

Steady state response;

$$x(t) = x_0 \exp(i\omega t) \tag{10}$$

Equation 11 is obtained by placing in Equation 7 of Equation 9 and Equation 10.

$$\left(K\text{-}mw^2\right) + ic\omega = \frac{P(t)}{x(t)} \tag{11}$$

Equation 12 is obtained from Equation 7 and Equation 11.

$$K = \left(\bar{K}\text{-}mw^2\right) + ic\omega \tag{12}$$

Equation 13 and Equation 14 are obtained when comparing Equation 8 with Equation 12;

$$K_1 = \bar{K}\text{-}m\omega^2 \tag{13}$$

$$K_2 = c\omega \tag{14}$$

While the first (real) part which indicates stiffness and inertia forces of the system depends on the frequency, the second (imaginary) part indicates energy loss in the system and also depends on the frequency [23]. Stiffness and damping coefficients can change depending on the frequency of the foundation soil system. Dynamic impedance factor depending on the frequency is found in equation 15 [23].

$$K = \bar{K}\left(k + i\omega c_s\right) \tag{15}$$

Viscous damping ratio is calculated by Equation 15.

$$\beta = \frac{C}{C_{Cr}} = \frac{C}{2K/\omega_n} \tag{16}$$

In Equation 17, K indicates impedance function, k stiffness and c damping.

$$K = \bar{K}(k + i a_0 c) \tag{17}$$

Dimensionless frequency factor is calculated by equation 18. In this equation, the angular frequency is indicated by w, radius for the circular foundation by B and shear wave velocity by V_s.

$$a_0 = \frac{\omega B}{V_S} \tag{18}$$

Spring system equivalent having 6 degrees of freedom is used to examine the soil-structure interaction. In the Gazetas soil model, the soil is modeled with springs and 3 translations and 3 rotations are created. The spring stiffness values $K_x, K_y, K_z, K_{\varnothing x}, K_{\varnothing y}, K_{\varnothing z}$ are calculated by using the equations in the literature. Here, r indicates the radius of the

Table 1. Equivalent lumped parameters for circular foundation [23].

Direction	*Spring Stiffness*
Vertical	$K_z = \frac{4Gr_z}{(1-\vartheta)}$
Horizontal	$K_x = \frac{32\ (1 - \vartheta)Gr_x}{(7-8\vartheta)}$
Rocking	$K_{\varnothing x} = \frac{8Gr_{\varnothing_x}{}^3}{3(1-\vartheta)}$
Rocking	$K_{\varnothing y} = \frac{8Gr_{\varnothing_y}{}^3}{3(1-\vartheta)}$
Torsion	$K_{\varnothing z} = \frac{16Gr_{\varnothing_y}{}^3}{3}$

Table 2. Characteristics of material in soils.

Soil	*Modülüs of Elasticity (MPa)*	*Unit volume weight (KN/m³)*
Soil 1	*Fixed support*	
Soil 2	*400*	*24*
Soil 3	*80*	*20*
Soil 4	*40*	*18*
Soil 5	*25*	*18*

Table 3. The properties of earthquakes [30]

Earthquake Number	*Earthquake Name*	*Year*	*Vs30 (m/s)*	*Focus Depth (km)*	*Earthquake Magnitude*	*Soil Class*	*Station Name*
1	*Imperial Valley-06*	*1979*	*205.78*	*24.6*	*6.53*	*D*	*Calipatria Fire Station*
2	*Imperial Valley-06*	*1979*	*205.63*	*3.95*	*6.53*	*D*	*El Centro Array #5*
3	*Victoria, Mexico*	*1980*	*471.53*	*14.37*	*6.33*	*C*	*Cerro Prieto*
4	*Morgan Hill*	*1984*	*729.65*	*14.84*	*6.19*	*C*	*Gilroy - Gavilan Coll.*
5	*N. Palm Springs*	*1986*	*344.67*	*4.04*	*6.06*	*D*	*North Palm Springs*
6	*Whittier Narrows-01*	*1987*	*245.06*	*20.79*	*5.99*	*D*	*Downey - Birchdale*
7	*Loma Prieta*	*1989*	*380.89*	*8.5*	*6.93*	*C*	*Saratoga - Aloha Ave*
8	*Northridge-01*	*1994*	*380.06*	*8.44*	*6.69*	*C*	*LA - Sepulveda VA Hospital*
9	*Kobe, Japan*	*1995*	*312*	*0.27*	*6.90*	*D*	*Takarazuka*
10	*Northwest China-03*	*1997*	*240.09*	*17.73*	*6.10*	*D*	*Jiashi*
11	*Parkfield-02, CA*	*2004*	*522.74*	*4.08*	*6.00*	*C*	*Parkfield - Cholame 2E*

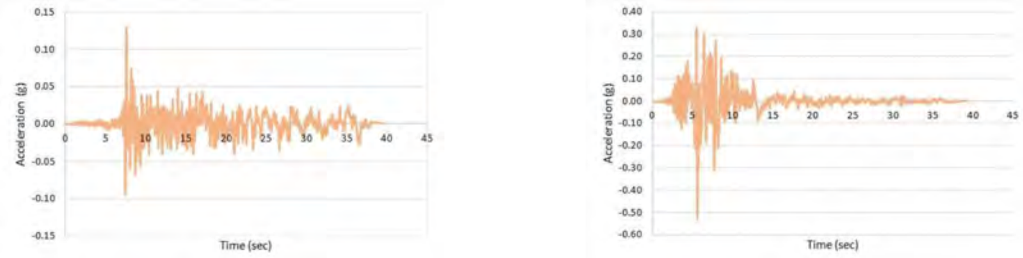

Earthquake Number 1

Earthquake Number 2

Earthquake Number 3

Earthquake Number 4

Figure 3. The acceleration values depending on time.

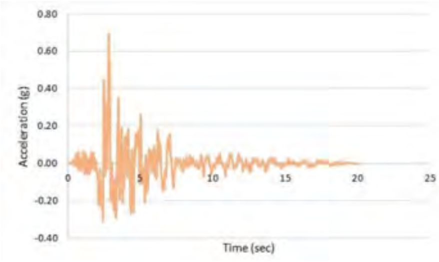

Earthquake Number 5

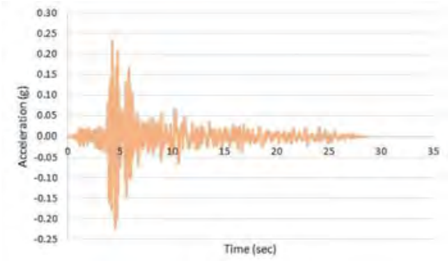

Earthquake Number 6

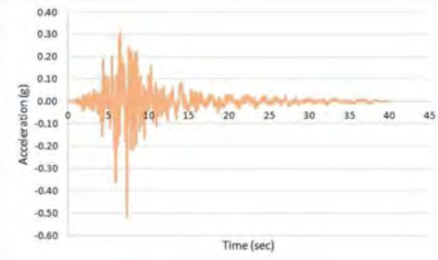

Earthquake Number 7

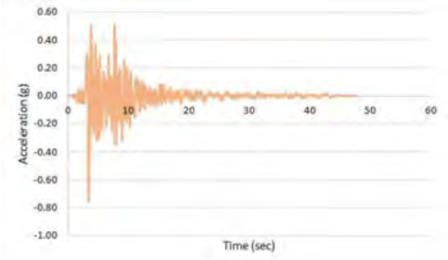

Earthquake Number 8

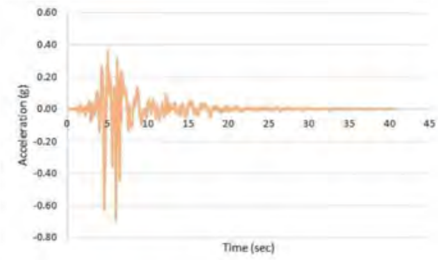

Earthquake Number 9

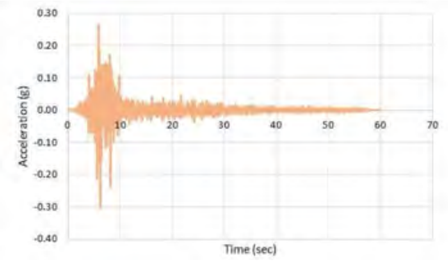

Earthquake Number 10

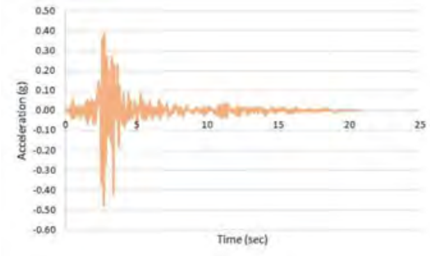

Earthquake Number 11

Figure 3. The acceleration values depending on time (continued).

circular foundation, G indicates the shear modulus of soil, , ϑ indicates poisson rate. The stiffness formulas for circular foundations and the material properties of soil is available in Table 1 and Table 2 respectively [23].

Seismic Risk Evaluation of Tank Structure

In order to perform seismic analysis of steel tank building, the time history method was used by considering fixed base and 4 different soil profiles. In this study, the effect of soil–foundation-structure interaction of tank buildings is examined by using ground motions of eleven earthquakes which occurred in the past and have different properties. The effective ground velocities of the earthquakes used in the analysis range from 205.63 m/s to 729.65 m/s, the magnitude of their range from 5.99 to 6.93 and the depth of focus their range from 0.27 km to 24.6 km. The characteristics of earthquakes and acceleration values depending on time are shown in Table 3 and Fig. 3 respectively.

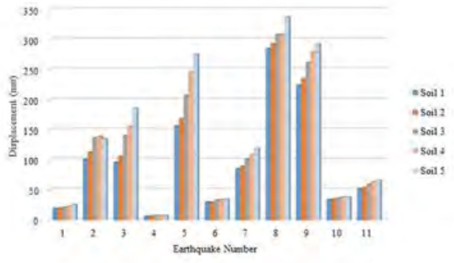

Figure 4. The values of displacement for all earthquakes and soil situations.

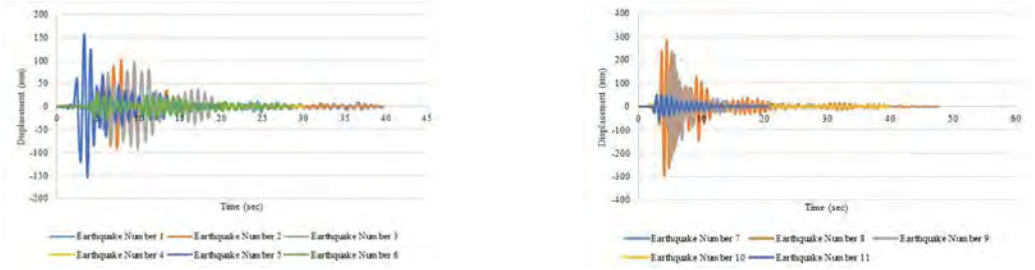

(a) Soil Type 1

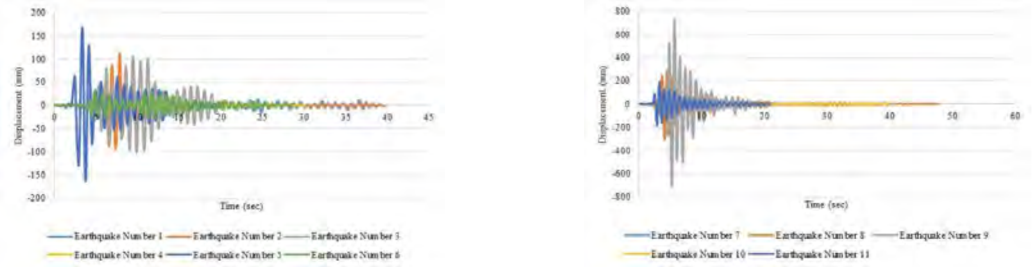

(b) Soil Type 2

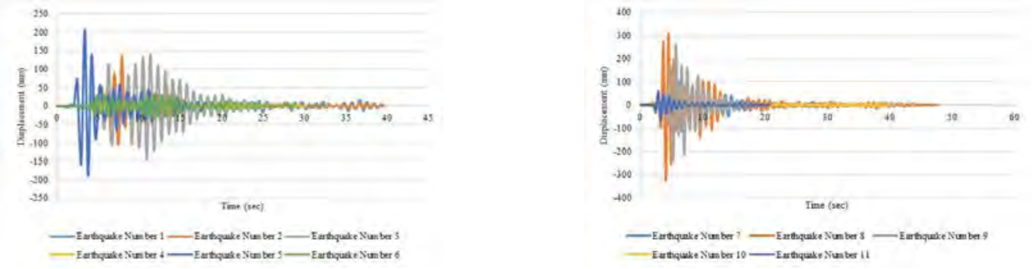

(c) Soil Type 3

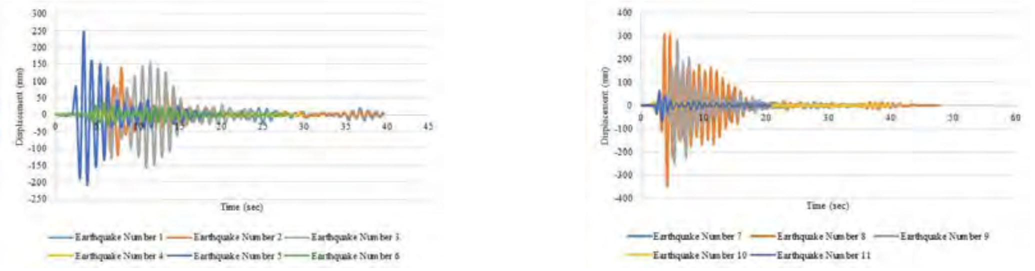

(d) Soil Type 4

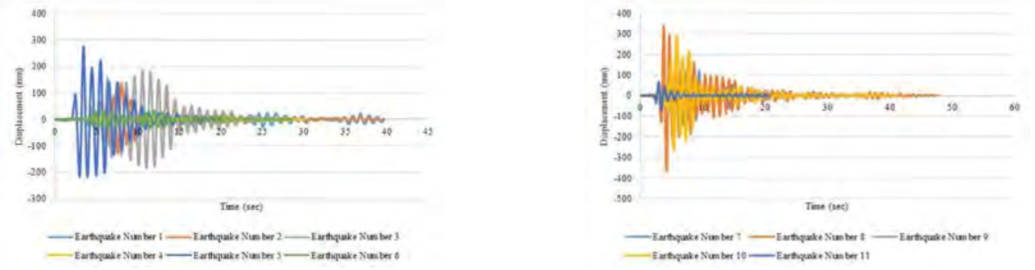

(e) Soil Type 5

Figure 5. The values of displacement depend on time for all earthquakes a) Soil Type 1 b) Soil Type 2 c) Soil Type 3 d) Soil Type 4 e) Soil Type 5.

As it is shown in Table 3, Magnitudes of 1 numbered Imperial Valley-06 (Calipatria Fire Station) Earthquake and 2 numbered Imperial Valley-06 (El Centro Array #5) earthquake are 6.53. While the peak ground acceleration of the 1 numbered Imperial Valley-06 (Calipatria Fire Station) Earthquake is 0.129g, the peak ground acceleration of the 2 numbered Imperial Valley-06 (El Centro Array #5) earthquake is 0.529g, and the ground speed is 205.78 m/s in the 1 numbered Imperial Valley-06 (Calipatria Fire Station) earthquake and is 205.63 m/s in the 2 numbered Imperial Valley-06 (El

Centro Array #5) earthquake. In view of 2 earthquakes, the focus depth of 2 numbered Imperial Valley-06 (El Centro Array #5) earthquake, which has high peak ground acceleration, has the lower than 1 numbered Imperial Valley-06 (Calipatria Fire Station) earthquake. As is seen in the Figure 2, duration of earthquakes and the values of the peak ground acceleration are different. As a result of time history analysis, displacement, stress and base shear force values were obtained and compared for eleven different earthquake conditions for each soil type.

Earthquakes were selected in accordance with TBDY 2018 [29]. The earthquake magnitudes, fault distances, local ground conditions were taken into account during earthquake selection. C and D were chosen as the soil class, and the magnitude of the earthquakes were selected between 5.99 and 6.93. 11 earthquake records having different effective ground acceleration values were used by taking from Pacific Earthquake Engineering Research Center [30].

The earthquake whose focus depth among the selected earthquakes is the smallest is 9 numbered Kobe earthquake and the earthquake whose focus depth is the largest is 1 numbered Imperial Valley-06. The distance to the fault of the center where the earthquake was recorded must be less than 10 km in order to be able to be a near fault. and the velocity pulse duration must be greater than 1.0 second, the ratio of the maximum velocity value to the maximum acceleration value must be greater than 0.1 second. [31,32,33].

RESULTS AND DISCUSSION

Determining seismic behavior of tanks is of great significance for decreasing damages which may occur in the course of the earthquake. For this purpose, a steel tank structure is designed by considering 4 soil conditions having different features and fixed support. While determining the behavior of the tank structure under the earthquake effect, dynamic analyzes were carried out with the time history method by considering the earthquakes 1979 Imperial Valley-06 (Calipatria Fire Station), 1979 Imperial Valley-06 (El Centro Array 5), Victoria, Mexico 1980, Morgan Hill 1984, N. Palm Springs 1986, Whittier Narrows-01 1987, Loma Prieta 1989, Northridge-01 1994, Kobe 1995, Northwest China-03 1997, Parkfield-02 2004.

Since the highest displacement values occur at the top of the tank, the displacement values at the top point are taken. The displacement values obtained as a result of the analysis are shown in Fig. 4. The lowest displacement values are obtained in fixed support for all earthquake conditions. The values of the largest displacement were obtained in 8 numbered Northridge-01 earthquake as 285.4372 mm, 292.7811 mm, 308.4658 mm, 308.63 mm, 337.8845 mm respectively for soil 1, soil 2, soil 3, soil 4 and soil 5. The smallest displacement values were obtained in 4 numbered Morgan Hill 1984 earthquake respectively 6.00 mm, 6.00 mm, 7.33 mm, 7.27 mm and 7.46 mm for soil 1, soil 2, soil 3, soil 4 and soil 5.

The change of displacement values depending on time for all earthquakes is shown in Figure 5. The displacement values increase with the increase in tank height. The variation depending on time is shown by taking the highest values in the top point of the tank. When analyzed in terms of earthquakes, it is seen that the displacement values are the highest in Northridge-01 earthquake, of which magnitude, peak ground velocity and focus depth are respectively 6.69, 380.06 cm/s and 8.44 km. Ankastre mesnet durumunda; 285.4372 mm yer değiştirmenin en büyük değeri elde edilmiştir. In the case of fixed support, the highest value of the displacement was obtained as 285.4372 mm. The smallest displacement value is obtained in Morgan Hill 1984 earthquake which has a magnitude of 6.19. Bu depremin yer hızı, odak derinliği sırasıyla 729.65 cm/s ve 14.84 km'dir. The ground speed, focal depth of this earthquake are respectively 729.65 cm/s ve 14.84 km. The smallest displacement value obtained is 6.00 mm. The magnitudes of 1 numbered Imperial Valley-06 (Calipatria Fire Station) and 2 numbered Imperial Valley-06 (El Centro Array #5) Earthquakes are the same, but their values of peak ground acceleration are different. The peak ground speed, depth of focus of the 1 numbered Imperial Valley-06 (Calipatria Fire Station) earthquake are respectively 205.78 cm/s, 24.6 km, while the peak ground speed and depth of focus of 2 numbered Imperial Valley-06 (El Centro Array #5) earthquake are 205.63 cm/s and 3.95 km respectively. It is seen that the values obtained from the 1 numbered Imperial Valley-06 (Calipatria Fire Station) earthquake are lower than the values obtained from 2 numbered Imperial Valley-06 (El Centro Array #5) earthquake. Peak ground velocity and focus depth of 9 numbered Kobe earthquake are 312 cm/s and 0.27 km, respectively, and it is seen that the values obtained from 9 numbered Kobe earthquake are lower than 8 numbered Northridge-01 (1994) earthquakes. The highest value of displacement obtained by using 9 numbered Kobe earthquake is 224.1925mm.

When considering the soils, the displacement graph depending on time is available in Fig. 6. It is seen that the lowest displacement values in the structure are obtained in the case of fixed support for all earthquakes. It is seen that the highest values are obtained in the case of Soil 5. The displacement value of 337.8845 mm in soil 5, 292.7811 mm in soil 2 and 285.4372 mm in the fixed support condition are obtained in 8 numbered earthquake having the highest peak ground acceleration and ground velocity. While the displacement value obtained as 6.00 mm and 6.00 mm in fixed support and in the case of soil 2, respectively, in 4 numbered Morgan Hill (1984) Earthquake, of which peak ground acceleration is the lowest, it was respectively obta-

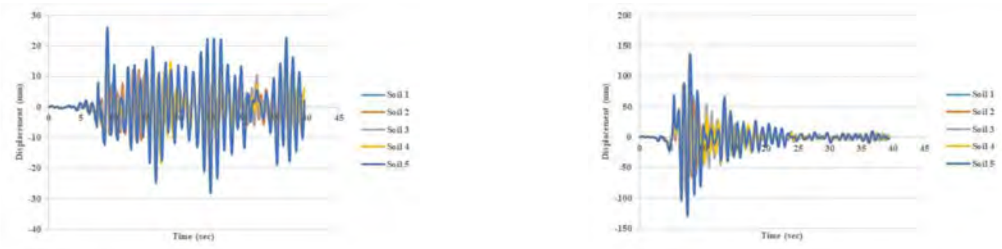

(a) Earthquake Number 1

(b) Earthquake Number 2

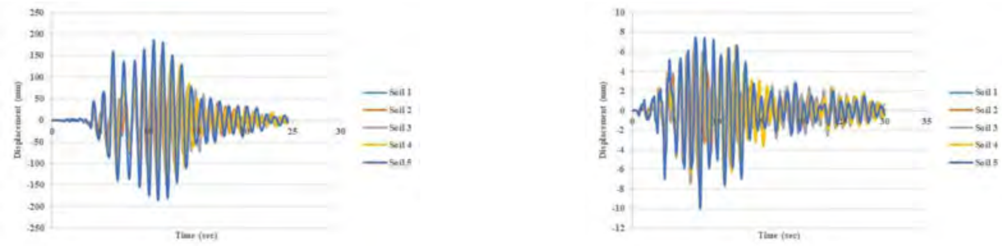

(c) Earthquake Number 3

(d) Earthquake Number 4

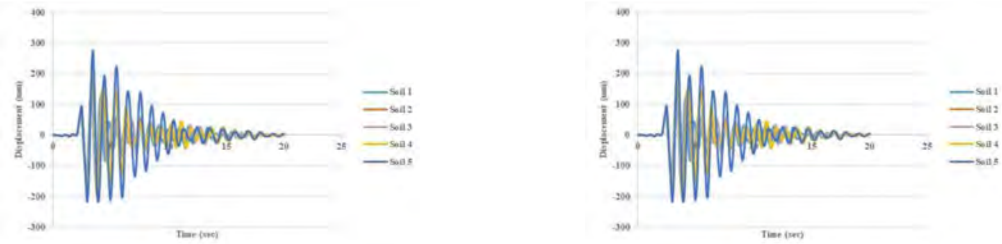

(e) Earthquake Number 5

(f) Earthquake Number 6

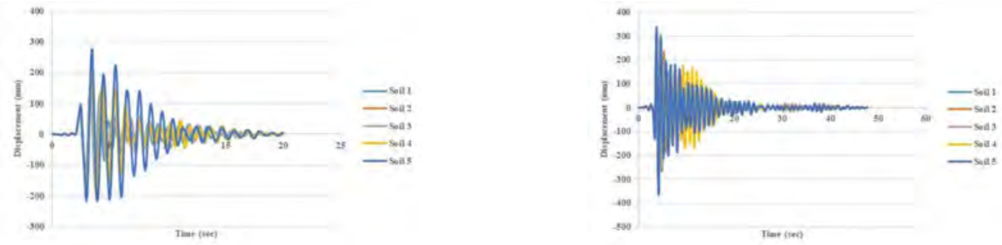

(g) Earthquake Number 7

(h) Earthquake Number 8

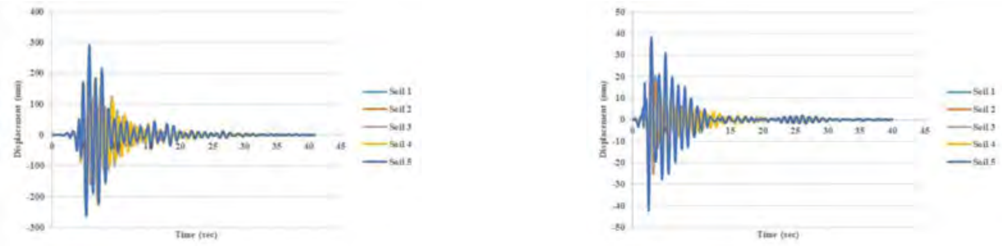

(i) Earthquake Number 9

(j) Earthquake Number 10

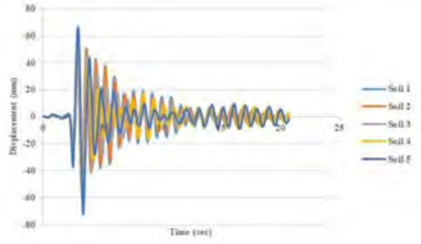

(k) Earthquake Number 11

Figure 6. The values of displacement depend on time a) Earthquake numbered 1, b) Earthquake numbered 2, c) Earthquake numbered 3, d) Earthquake numbered 4, e) Earthquake numbered 5, f) Earthquake numbered 6, g) Earthquake numbered 7, h) Earthquake numbered 8, i) Earthquake numbered 9, j) Earthquake numbered 10, k) Earthquake numbered 11 .

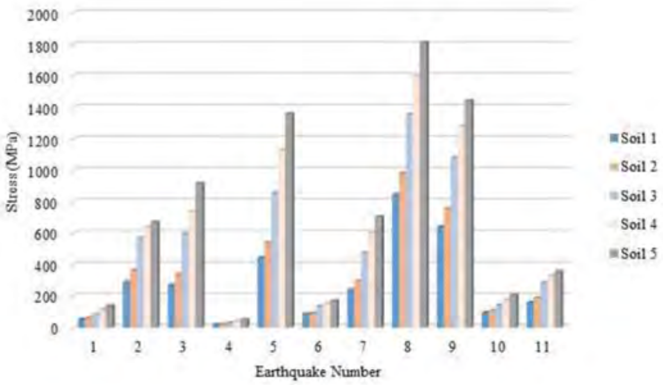

Figure 7. The values of stress for all earthquakes and soil situations.

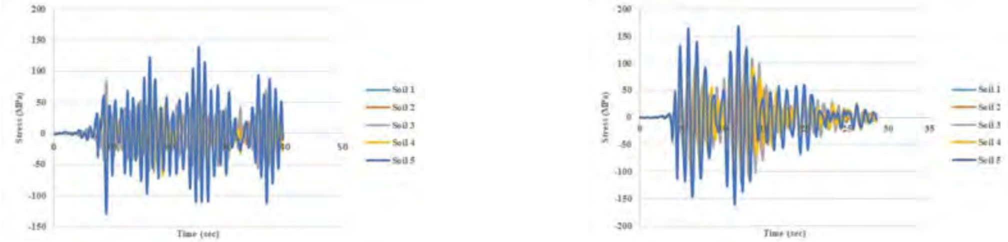

(a) Earthquake Number 1

(b) Earthquake Number 2

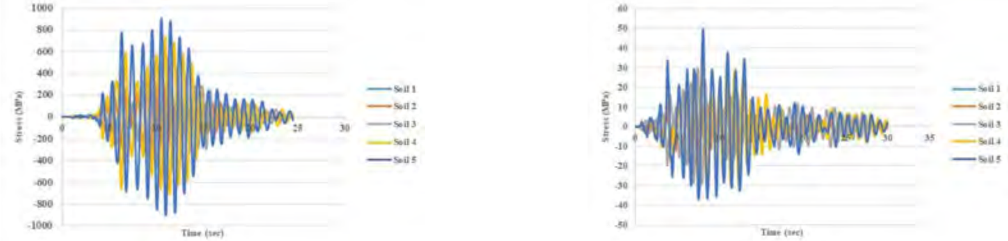

(c) Earthquake Number 3

(d) Earthquake Number 4

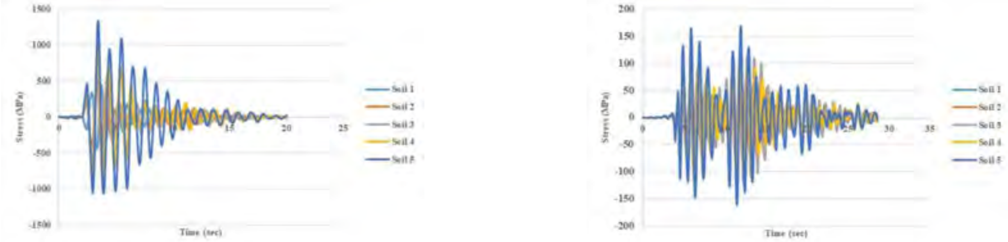

(e) Earthquake Number 5

(f) Earthquake Number 6

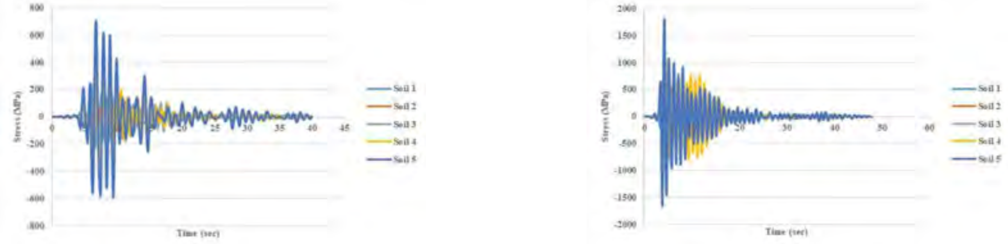

(g) Earthquake Number 7

(h) Earthquake Number 8

Figure 8. The values of stress depend on time a) Earthquake numbered 1, b) Earthquake numbered 2, c) Earthquake numbered 3, d) Earthquake numbered 4, e) Earthquake numbered 5, f) Earthquake numbered 6, g) Earthquake numbered 7, h) Earthquake numbered 8, i) Earthquake numbered 9, j) Earthquake numbered 10, k) Earthquake numbered 11.

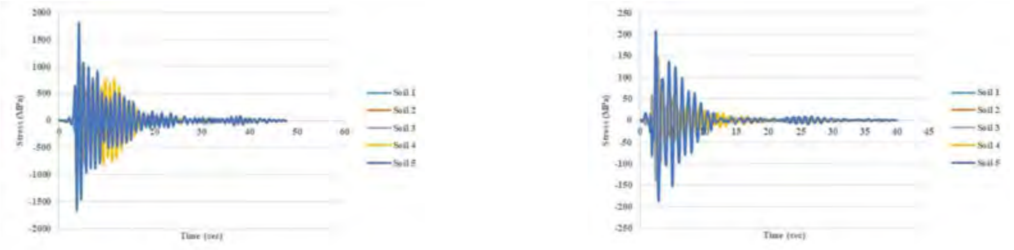

(i) Earthquake Number 9

(j) Earthquake Number 10

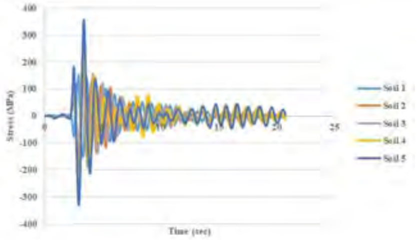

(k) Earthquake Number 11

Figure 8. The values of stress depend on time a) Earthquake numbered 1, b) Earthquake numbered 2, c) Earthquake numbered 3, d) Earthquake numbered 4, e) Earthquake numbered 5, f) Earthquake numbered 6, g) Earthquake numbered 7, h) Earthquake numbered 8, i) Earthquake numbered 9, j) Earthquake numbered 10, k) Earthquake numbered 11 (continued).

ined as 7.33mm,7.27mm, 7.45mm for the cases of soil 3,4 and 5. This value was obtained as 19.1135 mm, 19.1135mm, 21.04114mm, 22.77467mm, 26.07037mm for the cases of soil 1,2,3,4 and 5, respectively, at 1 numbered earthquake. When the 2 numbered earthquake was examined, the displacement values are obtained as 101.4455 mm, 112.8003 mm, 136.8489 mm, 138.6545mm, 135.2876 mm in cases of soil 1,2,3, 4 and 5, respectively. It is seen that the values obtained in the case of fixed support of the soil and in the case of 400 Mpa, where the elasticity module of the soil is the highest, are very similar and that the displacement values increase with the decrease of the modulus of elasticity and strength.

The values of the maximum stress and the stress depending on time are respectively seen in Fig. 7 and Fig. 8. The highest stress values were obtained as 846.265 MPa, 982.413 MPa, 1355.734 Mpa, 308.63 Mpa, 337.8845 MPa respectively in the cases of soil 1,2,3,4 and 5 at 8 numbered Northridge-01 earthquake. The smallest values of stress were obtained as 20.162 MPa, 20.162 MPa, 30.747 MPa, 40.903 MPa, 49.55 MPa respectively in the cases of soil 1,2,3,4 and 5 at 4 numbered Morgan Hill Earthquake. The ground speed of the Morgan Hill earthquake is 729.65 m/s, its focal depth is 14.84 km, its effective ground speed is 0.115 g, and it has the highest ground velocity and the smallest effective ground acceleration within11 earthquakes. The smallest displacement and stress values were obtained from this earthquake.

CONCLUSION

Examining of structure-soil-interaction of industrial structures such as tanks, silos and cooling towers to be built on weak grounds is very important in terms of structural safety. This study aims to evaluate the interaction of soil-foundation-structure having different parameters. The tank structures constructed on different soils must have required strength to stand the external loads such as earthquakes. For this purpose, the stiffness values of soils having different strengths were determined by using formulas related to elastic springs in the literature. Tank constructed on the soil designed as elastic spring was modeled with finite element methods and the dynamic analyses were performed by applying 11 time-dependent acceleration values.

The damage occuring because of the earthquakes having high peak ground acceleration and ground velocity values, are bigger compared to other earthquakes. It is seen that the effect of an earthquake having low focus depth, is higher and the damage to the structure is also bigger. When the varies of displacement and stress values depending on the time are examined, it is seen that the displacement and stress values are at the highest level at earthquake whose the value of the peak ground acceleration is at the highest level. While the highest values among these earthquakes were occurred in 8 numbered Northridge-01 earthquake, which has the highest peak ground acceleration and ground velocity values, it is followed by 9 numbered Kobe, 5 numbered N. Palm Springs, 2 numbered Imperial Valley-06 (El Centro Array #5), 3 numbered Victoria, Mexico, 7 numbered Loma Prieta, 11 numbered Parkfield-02, CA, 10 numbered Northwest China-03, 6 numbered Whittier Narrows-01, 1 numbered Imperial Valley-06 (Calipatria Fire Station) , 4 numbered Morgan Hill. The ground velocity of 4 numbered Morgan Hill earthquake has the highest and the its effective ground acceleration is the lowest. The smallest displacement and stress values were obtained in the 4 numbered Morgan Hill earthquake and the highest values were obtained in the 8 numbered Northridge-01 earthquake.

When considering different soil conditions, it is seen that the values of the displacement and stress obtained are very similar for the case in which the elasticity module of the soil is 400MPa and in the case where the soil is fixed supported. When all earthquake records were examined, it was seen that the smallest values were obtained in the case of the fixed soil and the obtained values in the soil 2, soil 3, soil 4 and soil 5 conditions respectively followed by the obtained values in fixed soil situation. It is also seen that the obtained values increase as the soil strength decreases.

CONFLICT OF INTEREST

Authors approve that to the best of their knowledge, there is not any conflict of interest or common interest with an institution/organization or a person that may affect the review process of the paper.

References

1. USGS Circular 1193. Implications for Earthquake Risk Reduction in the United States from the Kocaeli Turkey Earthquake of August 17, 1999; 2000.
2. Palanci M, Kayhan AH, Demir A. A statistical assessment on global drift ratio demands of mid-rise RC buildings using code-compatible real ground motion records. Bulletin of Earthquake Engineering. 16 (11) (2018) 5453-5488.
3. Yazici G, Cili F. Evaluation of the liquid storage tank failures in the 1999 Kocaeli Earthquake. In Proceedings of the 14th World Conference on Earthquake Engineering, Beijing, China, pp. 12-17, 2008 January.
4. Saatcioglu M, Mitchell D, Tinawi N, Gardner NJ, Gillies AG, Ghobarah A, Anderson, DL, Lau D. The August 17, 1999, Kocaeli (Turkey) earthquake - damage to structures. Can. J. Civ. Eng. 28 (2001) 715-737.
5. Kianoush M, Ghaemmaghami A. The effect of earthquake frequency content on the seismic behavior of concrete rectangular liquid tanks using the finite element method incorporating soil-structure interaction. Eng. Struct. 33 (7) (2011) 2186-2200.
6. Chung MA, Larkin TJ. Nonlinear Foundation Response of Liquid Storage Tanks under Seismic Loading. Proceedings of New Zealand Society for Earthquake Engineering Annual Conference. 2008.
7. Kramer SL. Geotechnical earthquake engineering. Prentice Hall, Upper Saddle River; 1996.
8. Veletsos AS, Meek JW. Dynamic behaviour of building foundation systems. Earthq. Eng Struct Dyn. 3 (1974) 121–38.
9. Scarfone R, Morigi M, Conti R. Assessment of dynamic soil-structure interaction effects for tall buildings: A 3D numerical approach. Soil Dynamics and Earthquake Engineering. 128 (2020) 105864.
10. Mezaini N. Effects of soil-structures interactions on the analysis of cylindrical tanks. ASCE Practice Periodical on Structural Design and Construction. 11 (1) (2006) 50–57.
11. Bhattacharya K, Dutta SC. Assessing lateral period of building frames incorporating soil-flexibility. Journal of Sound and Vibration. 269 (3-5) (2004) 795-821.
12. Dutta CH, Bhattacharya K, Roy R. Response of low rise buildings under seismic ground excitation incorporating soil structure interaction. Soil Dyn. Earthq. Eng. 24 (2004) 893–914.
13. Ghandil M, Behnamfar F. A near-field method for dynamic analysis of structures on soft soils including inelastic soil-structure interaction. Soil Dynamics and Earthquake Engineering. 75 (2015) 1–17.
14. Meng X, Li X, Xu X. Earthquake Response of Cylindrical Storage Tanks on an Elastic Soil. J. Vib. Eng. Technol. 7 (2019) 433-444.
15. Dutta S, Mandal A, Dutta SC. Soil–structure interaction in dynamic behavior of elevated tanks with alternate frame staging configurations. Journal of Sound and Vibration, 227 (4-5) (2004) 825-853.
16. Zhao C, Chen J, Wang J, Yu N, Xu Q. Seismic mitigation performance and optimization design of NPP water tank with internal ring baffles under earthquake loads. Nuclear Engineering and Design, 318 (2017) 182-201.
17. Zhao C, Chen J, Xu Q. FSI effects and seismic performance evaluation of water storage tank of AP1000 subjected to earthquake loading. Nuclear Engineering and Design. 280 (2014) 372-388.
18. Nicolici S, Bilegan RM. Fluid structure interaction modeling of liquid sloshing phenomena in flexible tanks. Nuclear Engineering and Design, 258 (2013) 51-56.
19. Patel CN, Sharma, K, Patel HS. Modeling of Soil-Structure Interaction as Finite Element Using Using SAP2000. 2011.
20. Seleemah, AA, El-Sharkawy M. Seismic analysis and modeling of isolated elevated liquid storage tanks. Earthquake and Structures, 2 (4) (2011) 397-412.
21. Livaoğlu R, Doğangün A. Simplified seismic analysis procedures for elevated tanks considering fluid–structure–soil interaction. Journal of fluids and structures, 22 (3) (2006) 421-439.
22. Livaoglu, R. and Dogangün A. Seismic behaviour of cylindrical elevated tanks with a frame supporting system on various subsoil. Indian Journal of Engineering & Materials Sciences 14 (2007) 133-145.
23. Gazetas G. Analysis of machine foundation vibrations: state of the art. International Journal of Soil Dynamics and Earthquake Engineering. 2 (1) (1983) 2-4.
24. Habibullah and Wilson. SAP 2000 User Manual, Computer Program, Computers and Structures. Berkeley, USA.1998.
25. Roder HM. Liquid Densities of Oxygen, Nitrogen, Argon and Parahydrogen (Metric Supplement), Cryogenic Division, Institute for Basic Standards (U.S.). National Bureau of Standards, Technical Note 361; 1974.
26. Housner GW. The dynamic behavior of water tanks. Bulletin of the seismological society of America, 53 (2) (1963) 381-387.
27. Housner GW. Dynamic pressures on accelerated fluid containers. Bulletin of the seismological society of America, 47 (1) (1957) 15-35.
28. Jacobsen LS. Impulsive hydrodynamics of fluid inside a cylindrical tank and of fluid surrounding a cylindrical pier. Bulletin of the Seismological Society of America, 39 (3) (1949) 189-204.
29. TBDY, Türkiye Bina Deprem Yönetmeliği, Ankara,2018.
30. Pacific Earthquake Engineering Research (PEER) Center, https://ngawest2.berkeley.edu/
31. Akkar S, Yazgan U, Gülkan P. Drift estimates in frame buildings subjected to near-fault ground motions. Journal of Structural Engineering, 131 (7) (2005) 1014-1024.
32. Kayabalı, K. Geoteknik Deprem Mühendisliği, Gazi Kitabevi, Ankara, 2003.
33. Özmen A. Yakın ve uzak fay hareketlerine maruz tarihi yığma bir köprünün sismik performansının değerlendirilmesi, Fırat Üniversitesi, Fen Bilimleri Enstitüsü, 2019.

Hittite Journal of Science and Engineering, 2022, 9 (1) 57–63
ISSN NUMBER: 2148–4171
DOI: 10.17350/HJSE19030000255

Fabrication and Characterization of ZnO Nanosheet on a Silver-metalized Polyimide Substrate

Alper Cetinel
Ege University, Department of Physics, Izmir, Turkey

Article History:
Received: 2021/07/19
Accepted: 2022/02/07
Online: 2022/03/30

***Correspondence to**: Alper Cetinel, Ege University, Department of Physics, 35030, Bornova, Izmir, Turkey.*
E-Mail: alper.cetinel@ege.edu.tr
Phone: +90 (232) 311 2372

ABSTRACT

ZnO nanosheets were fabricated on a silver-metalized polyimide (PI/Ag) substrate using electrochemical deposition. FE-SEM, XRD, UV–Vis absorption, and I-V measurements were employed to examine the structural, optical and electrical properties of silver-metalized PI film and ZnO deposited PI/Ag film. For a comparison, PI/Ag film was also investigated without ZnO layer. FE-SEM analysis indicated that a silver film layer, consisted of spherical Ag nanoparticles, and the ZnO nanosheets were synthesized on PI substrate by electroless and electrochemical deposition, respectively. Moreover, the growth mechanism of the Ag film and ZnO nanosheets was also discussed. The characterization of X-ray diffraction verified that the ZnO nanosheets had a hexagonal phase and grew along the [002] direction. The optical absorbance spectra of bare PI, PI/Ag, and PI/Ag/ZnO showed a broad absorption peak around 300 nm. The electrical properties of the PI/Ag and PI/Ag/ZnO samples were studied by current-voltage (I-V) measurements in the dark environment at room temperature (300 K). The I-V measurements suggested that the samples presented ohmic characteristics. The results revealed that the deposition of ZnO on PI/Ag substrate improved the electrical conductivity compare with bare PI/Ag.

Keywords:
ZnO nanosheet; Polyimide; Silver; Electrochemical deposition; SEM; XRD; Characterization

INTRODUCTION

As flexible optoelectronic materials develop increasingly common, there is a significant demand for flexible conducting electrodes, which are crucial parts for optoelectronic devices [1–3]. Polymer-based materials are the most widely used candidates for flexible substrate due to their benefits of high flexibility, low-cost and easy processability [4]. Among them, polyimide (PI) are the most promising flexible substrate materials thanks to their high heat resistance, superior mechanical properties and high radiation resistivity [5–7]. Though, the adhesion of passive metals, such as silver, nickel, copper, to polymers is very weak [8]. To enhance the surface adhesion of polyimide, many techniques are usually carried out such as chemical deposition methods, sputtering deposition methods, electrochemical deposition, and electroless deposition [4]. Among them, electrochemical and electroless depositions allow the growth of metal nanostructures on polymeric films, without changing the properties of the films [9]. Moreover, these methods are variable owing to uncomplicated materials, light reaction conditions, and applicability to non-conductive surfaces.

Silver has the highest conductivity (10^7 S/m) among noble metals and also has outstanding reflectivity at longer wavelengths [1]. The PI/silver film could present many advantages in flexibility and elasticity [9, 10]. Akamatsu et al. [11] reported that polyimide films have been prepared in silver nitrate solution by the electroless method. The metalized polyimide was obtained through both excellent conductivity and reflectivity [11]. However, the chemical stability of the flexible polyimide substrate is reduced considerably, as a result of the catalysed decay of polyimide chains (carbon bonds) by silver, hence, limit their practical applications. To passivate PI surface, carbon nanotube and metal nanoparticles (NPs), such as Pt, Ni and Cu were used up to now [12–15]. In addition, there are several reports on the use of ZnO on PI substrate [1, 16-20]. In recent years, the formation of ZnO seed and/or buffer layers on polymer substrates has been commonly used to fabricate ZnO nanorod or nanosheet layers on substrates [20]. Although the seed/buffer layers are useful for producing ZnO nanostructures, there are some challenges concerning device functionality. The most important issue is the production cost. Compared to other production methods, the electrochemical deposition method is a simple, fast, low-cost process. Moreover, it provides the ability to tailor size, shape, and morphology of the nanostructures deposited under a set of well controlled synthesis parameters. To the best of our knowledge, there are no reports so far about the electrochemical deposition of ZnO nanosheet on a silver-metalized polyimide (PI/Ag) substrate.

In this study, as the first step, the surface of polyimide was chemically adjusted applying potassium hydroxide (KOH) to produce potassium polyamate. Then silver nanostructures were formed on polyimide substrate via the electroless deposition. In final step, ZnO nanosheet layer has been prepared on silver metalized PI substrate by electrochemical deposition without using any seed/buffer layer. The structural, optical, and electrical analyses were performed with a field emission scanning electron microscopy (FE-SEM), X-ray diffraction (XRD), ultraviolet–visible (UV–Vis) absorption and I-V measurements.

MATERIAL AND METHODS

All chemicals employed in this research were purchased from Sigma-Aldrich® and Polyimide substrate was obtained from DuPont (Kapton HN, 75 µm thick). The details of the procedure used for the PI surface adjustment shown in Figure 1. First, A PI substrate was cleaned with acetone and isopropanol, and washed with distilled water. Then, the PI substrate was immersed into a 5 M KOH solution at 50 ⁰C for 5 min. As a result of this process, potassium polyamate was formed on the PI surface via cleavage of their imide rings [11, 21, 22]. Then, surface metallization of PI film was carried out by dipping of PI film in 5 mM silver nitrate ($AgNO_3$) and 0.17 M glucose solution for 15 min at room temperature (Electroless deposition). An ion-exchange process occurred between K^+ ions in PI film and silver ions during the electroless deposition.

PI/Ag sample was annealed at 300 ⁰C for 30 min in vacuum furnace. After thermal treatment, ZnO nanosheets were obtained by electrochemical deposition technique. The deposition solution contained of an aqueous solution of 0.05M $Zn(NO_3)_2.6H_2O$ and 0.05 M $C_6H_{12}N_4$. The pH and temperature were selected as 5.1 and 80 ⁰C, respectively. The anode and cathode electrode were a PI/Ag film and platinum wire, respectively. ZnO nanosheets were deposited on PI/Ag at a constant current density of 0.5 mA/cm² for 30 minutes. After the deposition, PI/Ag/ZnO was washed with distilled water. Figure 2 shows the digital images of the samples obtained after electroless and electrochemical deposition. Surface morphologies of PI/Ag and PI/Ag/ZnO samples were examined with FE-SEM (QuantaFEG). X-ray diffraction (XRD) patterns were obtained from a

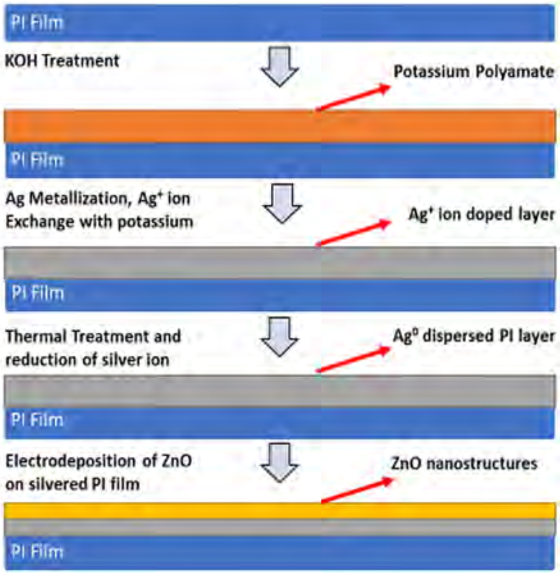

Figure 1. Schematic representation of the surface modification of the polyimide film and electrochemical deposition of ZnO on PI/Ag film.

Panalytical Empyrean XRD system using a CuK_α radiation (λ = 0.15418 nm). The absorption spectra of samples were obtained using a Perkin Elmer Lambda 950 (UV/Vis/NIR) spectrophotometer within the range of 200-800 nm. The forward and reverse bias I-V measurements were performed using Keysight B2901A source meter (SMU) in dark at room temperature (300 K).

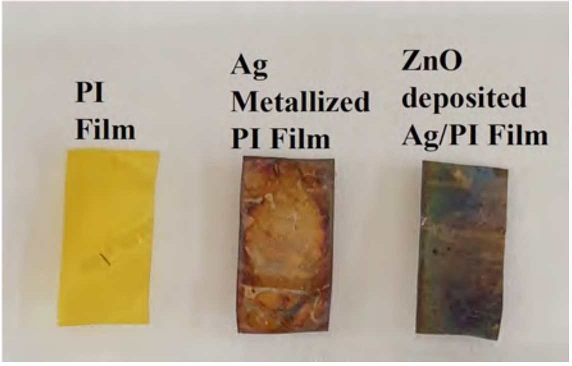

Figure 2. Digital images of the surface morphologies of the PI films before and after metallization of Ag and ZnO deposited, respectively.

RESULTS AND DISCUSSION

SEM Analysis

As illustrated in Figure 1, before forming homogeneous ZnO nanostructures, PI film was embedded in $AgNO_3$ solution to form the Ag film on top of the PI surface to increase the chemical and electrical stability. Then, ZnO layer was formed on the PI/Ag substrate. Ag layer acts as a nucleation site for the ZnO layer growth. The Ag particles forming after the metallization of PI film and ZnO deposited PI/Ag sample were characterized using the secondary electron mode in FE-SEM to provide topographical and elemental information. Figure 3 (a) shows a top surface FE-SEM image of PI/Ag. As seen in Figure 3 (a), the layer of Ag particles developed on PI film after the electroless deposition. Moreover, the Ag layer is homogeneous with respect to morphology and nanoparticle diameter. The average diameter of spherical Ag nanoparticle is about 200 nm. It has also found that smaller spherical silver nanoparticles coalesce and form silver nanorods that grow upwards from the surface (Figure 3 (a)). The growth process of Ag structures could be described by diffusion-limited aggregation (DLA) model [23]. Initially, Ag^+ ions take electrons to create silver particles on the PI which was treated with KOH. As the reaction continue, the further silver particles are produced at the same time. At the end of process, Ag film (nanorod and spherical particles), formed by agglomerated Ag nanoparticles, is obtained on the PI surface.

Figure 3 (b) demonstrates the FE-SEM image of ZnO structures grown on PI/Ag at 80 ºC and indicates that obtained structures consist of sheet-like structure. As seen in Figure 3 (b), the ZnO nanosheets are linked to each other and produce networks on the Ag nanoparticles. The average thickness of the ZnO nanosheets are in the range of 500-1000 nm with the typical diameter of 1–5 µm. Mostly the ZnO nanosheets are combined to form flower-shaped patterns. Recent studies reveal that the influence of deposition parameters such as current density, solution temperature and pH values, on the growth of ZnO nanostructures are significant [24]. The SEM analysis results are consistent with the works conducted by Aydemir et al. [24] and Yang et al. [25]. To explain growth of ZnO nanosheet via electrochemical deposition, the possible chemical reactions that take place are as shown below [25]:

$$NO_2^- + H_2O + 2e \rightarrow NO_2^- + 2OH^- \quad (1)$$

$$Zn^+ + 2OH^- \rightarrow Zn(OH)_2 \quad (2)$$

$$Zn(OH)_2 \rightarrow Zn + H_2O \quad (3)$$

In the case of the growth of ZnO nanosheet layer on PI/Ag, at the initial stage of deposition, smaller ZnO nanoparticles were formed on PI/Ag film. It is important to note that the formation of ZnO nanoparticles is critical because it requires nucleation spots for nanosheet creation. Then, a lot of ZnO nuclei produced and combined. As the process continues, the individual groups ultimately expand into nanosheets. Accumulations of smaller particle groups would subsequently establish larger clusters, which has promoted the formation of the sheet-like structure [25].

The composition of the prepared samples was studied further by conducting EDAX analysis. Figure 4 shows the EDAX profiles of the PI/Ag and PI/Ag/ZnO samples. During the electroless deposition PI substrates in the $AgNO_3$ solution, ion-exchange is estimated to occur between K^+ and Ag^+ ions. EDAX spectra in Figure 4 a,b indicate that Ag and O are detected but also a negligible detection of K. The slightly low K atomic percentage is attributed to above-mentioned immersion process. It is also estimated that oxygen is formed because of the formation of a carboxylate function with K+ counter ions. Figure 4 c,d shows the EDAX spectra of PI/Ag sample after deposited ZnO. It is revealed that K^+ is no more detected while ZnO is detected. At the surface of the PI/Ag, ion-exchange could be occurred between K+ and Zn^{2+} ions during the electrochemical deposition on the surface of PI/Ag substrate. Furthermore, increase of the oxygen atomic percentage is probably due to the imide cycle hydrolysis.

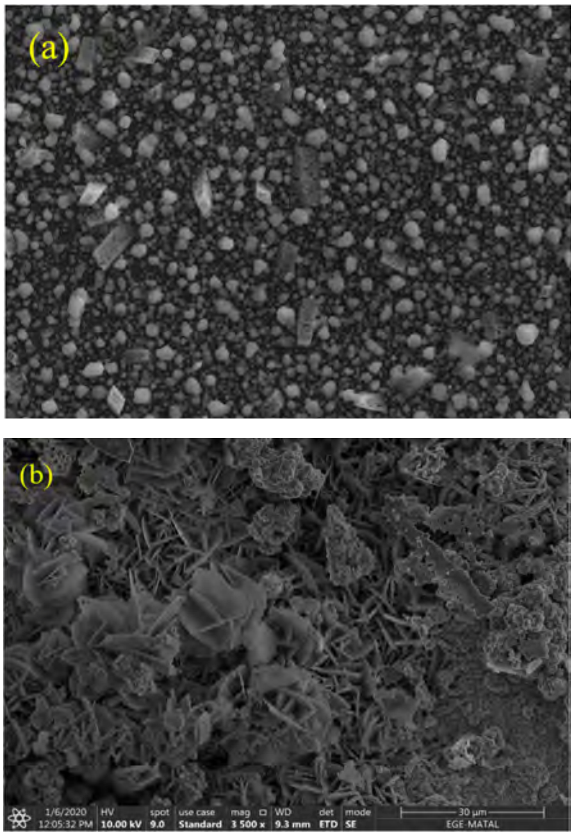

Figure 3. (a) FE-SEM image of silver nanostructures on PI substrate after electroless deposition (b) FE-SEM image of ZnO nanosheet on PI/Ag substrate after electrochemical deposition.

XRD Analysis

X-Ray diffraction was presented to examine and identify the purity of phase and the structure of the samples. Figure 5 represents the XRD patterns of silver metalized PI film and ZnO deposited PI/Ag sample. The XRD patterns of silver metalized PI film indicated that the obtained structure of Ag nanoparticle is face-centered cubic (FCC). As shown in Figure 5 (a), XRD analysis of PI/Ag

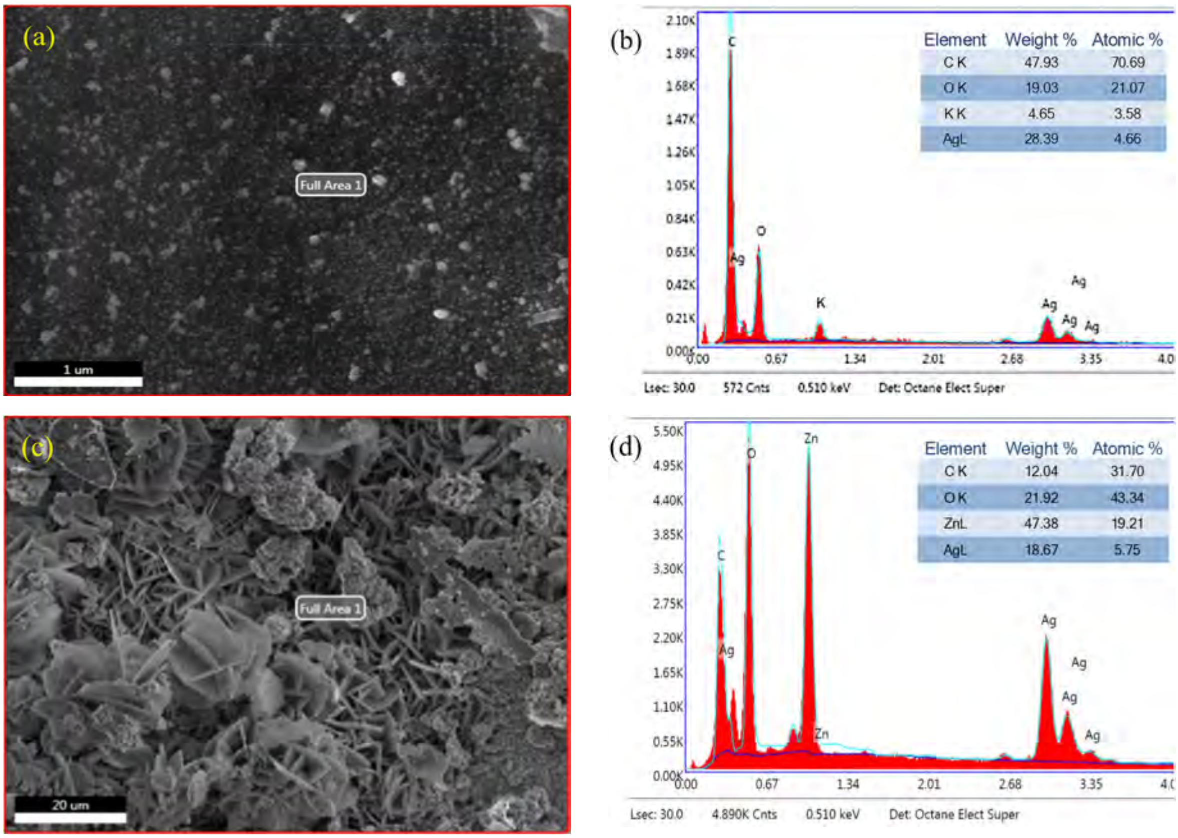

Element	Weight %	Atomic %
C K	47.93	70.69
O K	19.03	21.07
K K	4.65	3.58
AgL	28.39	4.66

Element	Weight %	Atomic %
C K	12.04	31.70
O K	21.92	43.34
ZnL	47.38	19.21
AgL	18.67	5.75

Figure 4. (a)-(b) EDAX analysis of silver nanostructures on PI substrate after electroless deposition, (c)-(d) EDAX analysis of ZnO nanosheet on PI/Ag substrate after electrochemical deposition.

sample reveals that three diffraction peaks at 2θ values of 38°, 44°, and 62° are attributed to the (111), (200), and (220) planes of the FCC structure of silver, which is consistent with the JCPDS file no. 4-0781 [22, 25]. Despite the Ag diffraction peaks, the peak observed at 20° belongs to the PI substrate [18]. XRD analysis clearly shows that Ag nanoparticles have a preferred orientation along the [111] direction.

Figure 5 (b) indicates the XRD pattern of the ZnO nanosheets obtained on PI/Ag. The peaks at 2θ values of 32°, 34°, 36°, and 47° correspond to (100), (002), (101), and (102) planes of the wurtzite structure of ZnO (JCPDS No. 36-1451) [25]. As seen in Figure 5 (b), the XRD pattern of the PI/Ag/ZnO demonstrates axis orientation along (002). It is clearly understood that the growth pattern is along the c-axis. XRD analysis of PI/Ag/ZnO indicates that the grown ZnO nanosheets represent a hexagonal wurtzite crystalline structure [16,24,25]. As seen in Figure 5 (b), apart from the (002) plane, additional small peaks in the XRD pattern of the PI/Ag/ZnO sample confirms the existence of the polycrystalline ZnO.

The average crystallite size of the PI/Ag and PI/Ag/ZnO samples along (111) and (002) planes was estimated using Scherrer formula (Eq. 4), using full width at half maximum (FWHM) [26],

$$D=\frac{0.9\lambda}{\beta\cos\theta} \tag{4}$$

where D, λ, β and θ are the crystallite size, the wavelength of incident X-ray (1.5418 Å), FWHM of the (111) and (002) peaks and the diffraction angle, respectively. From the Scherrer equation, the average crystallite size of Ag nanoparticles for the PI/Ag and PI/Ag/ZnO samples are about 30.5 and 26.8 nm, respectively. The average crystallite size of ZnO nanosheet along (002) planes calculated from Scherrer equation is about 41.5 nm.

Optical Measurements

The optical absorption spectra of Ag and ZnO embedded PI film are demonstrated in Figure 6. The absorption spectra of bare PI film are also added for reference. As seen in Figure 6, the absorption edge of PI film is at 230-260 nm range. After Ag and ZnO deposition, the absorption edge is shifted to the longer wavelengths. The absorption spectra of Ag and ZnO embedded PI film are shown in the range of 200–400 nm, and the absorption was reduced above 400 nm. In the spectrum of the PI/Ag/ZnO, the absorption peak appeared about 300 nm, is the

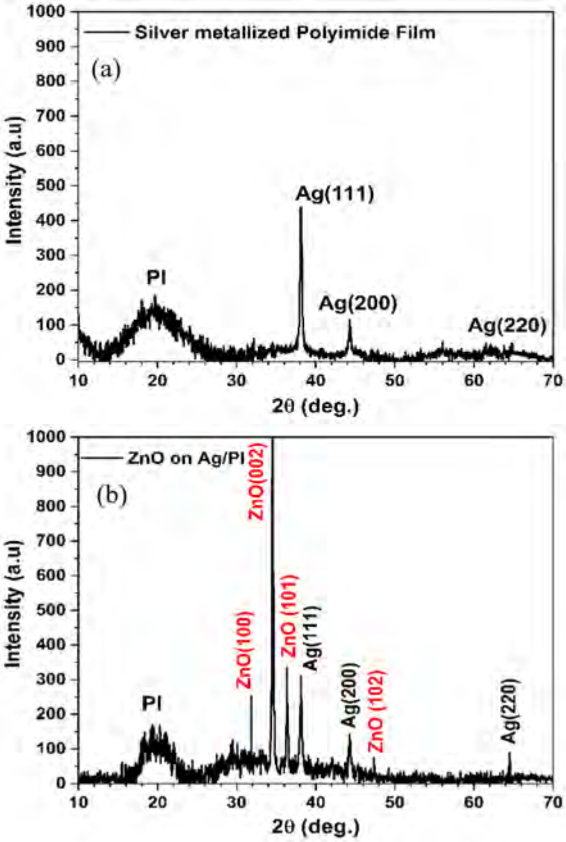

Figure 5. (a) XRD patterns of PI/Ag, (b) XRD patterns of PI/Ag/ZnO.

characteristic peak correspond to the exciton absorption of ZnO. It should be noted that for the sample of PI/Ag, there is not observed any absorption peak at about 400 nm, corresponding to the surface plasmon resonance (SPR) in silver nanostructures, because of the formation of discontinuous but interconnected Ag nanorods layer [23, 27].

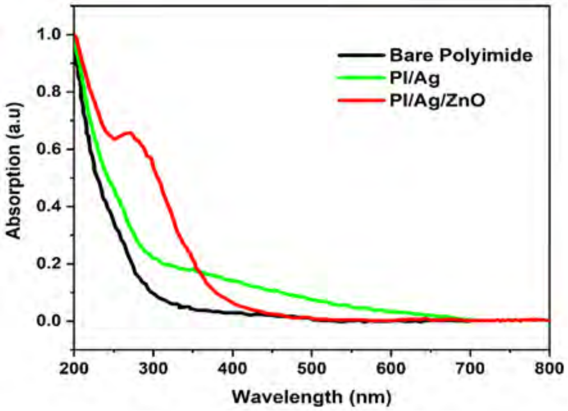

Figure 6. Optical absorption spectra of the bare PI film, PI/Ag and PI/Ag/ZnO samples.

I-V Measurements

The electrical properties of the all samples were investigated by measuring the current-voltage (I-V) characteristic at room temperature (300 K) and in the dark environment. These measurements were made using Keysight B2901A Source Meter (SMU) in the bias range of -5V to + 5V. Figure 7 shows I-V plots of silver metalized PI film and ZnO deposited PI/Ag sample.

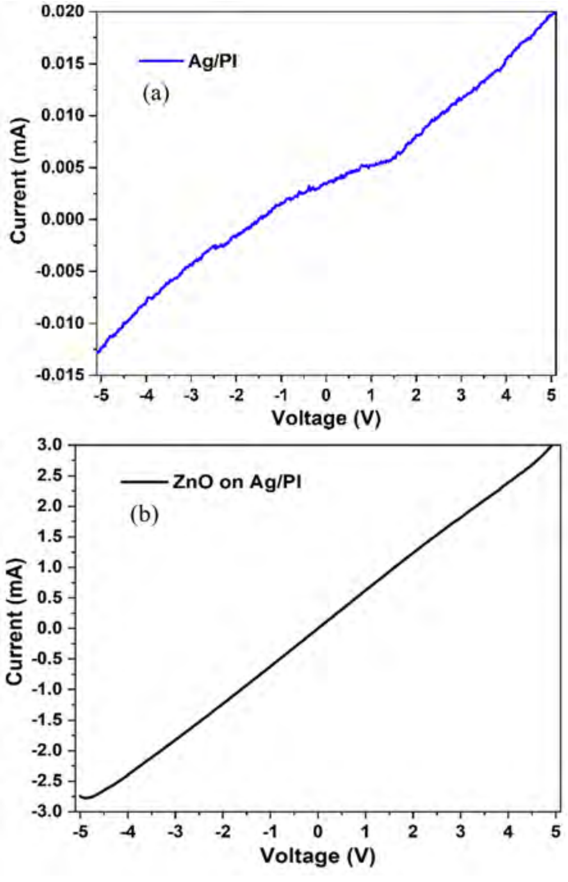

Figure 7. Dark current versus voltage characteristic of the samples at room temperature (a) PI/Ag, (b) PI/Ag/ZnO.

As seen in Figure 7, these structures exhibit non-rectifying property and show an ohmic characteristic. Low sheet resistance and linear I-V behaviour are vital for the efficiency and reliability of flexible semiconductor devices, and their synthesis and characterization are considerable efforts in circuit fabrication [19]. Therefore, the bulk resistance (R) of the samples could be determined from Figure 7 (V/I) [28]. The electrical resistance of PI/Ag and PI/Ag/ZnO samples are calculated as 252 kΩ and 1.67 kΩ. Also, a four-point probe is used to determine the sheet resistance of samples. The Rs of PI/Ag and PI/Ag/ZnO samples are calculated as 884.45 kΩ/sq and 294.30 kΩ/sq. The high of sheet resistance of the PI/Ag sample is probably due to the presence of unbonded potassium ions on the PI surface after electroless deposition, which was also observed in SEM-EDAX analyses. The absence of these potassium ions in EDAX analysis after ZnO deposition revealed that ZnO passivated the PI/Ag surface and helped to reduce both bulk resistance and sheet resistance.

CONCLUSION

In conclusion, surface modification and silver metallization of polyimide (PI) film were successfully performed by immersion method and ZnO were deposited onto surface of PI for passivation purpose by electrochemical deposition. The structural and electrical properties of silver metalized PI film and ZnO deposited PI/Ag film have been investigated by FE-SEM, XRD and I-V measurement. FE-SEM analysis revealed that after the electroless deposition, an Ag film layer consisted of spherical Ag nanoparticle was formed on the surface of the PI film. The average diameter of spherical Ag nanoparticles is about 200 nm. FE-SEM analysis indicated that ZnO nanosheets were successfully fabricated by electrochemical deposition on PI/Ag film. The average thickness of the ZnO nanosheets are in the range of 500-1000 nm. The XRD analysis shows that for PI/Ag sample, the obtained structure of Ag nanoparticle was face-centered cubic (FCC) and Ag nanoparticles were oriented in the (111) direction. XRD analysis of ZnO deposited PI/Ag film indicates that ZnO nanosheets had hexagonal wurtzite crystalline structure and were oriented in the [002] direction. The optical absorption spectra were measured in the range from 200 nm to 800 nm, and the absorption peaks for bare PI, PI/Ag and PI/Ag/ZnO appeared around 250–300 nm. The current-voltage (I-V) analysis was carried out to examine the electrical properties of the PI/Ag and PI/Ag/ZnO samples in the dark environment at room temperature (300 K). The I-V measurements suggested that the samples exhibited ohmic characteristics. Also, the results of I-V measurements were clearly indicated that deposited ZnO passivated the PI/Ag surface and improved electrical conductivity. Consequently, the ZnO deposited PI/Ag could be a good candidate for the possible applications in optoelectronic and sensor devices.

CONFLICT OF INTEREST

I do not have any conflict of interest or common interest with any institution or person that I know that could affect my work.

References

1. Lee D, Youn DY, Luo Z, Kim I D. Highly flexible transparent electrodes using a silver nanowires-embedded colorless polyimide film via chemical modification. RSC Adv. 6 (2016) 30331–30336.
2. Yu Y, Shen W, Li F, Fang X, Duan H, Xu F, Xiong Y, Xu W, Song W. Solution-processed multifunctional transparent conductive films based on long silver nanowires/polyimide structure with highly thermostable and antibacterial properties. RSC Adv. 7 (2017) 28670–28676.
3. Kang L, Shi Y, Zhang J, Huang C, Zhang N, He Y, Li W, Wang C, Wu X, Zhou X. A flexible resistive temperature detector (RTD) based on in-situ growth of patterned Ag film on polyimide without lithography. Microelectron. Eng. 216 (2019) 111052.
4. Liaw DJ, Wang KL, Huang YC, Lee KR, Lai JY, Ha CS. Advanced polyimide materials: Syntheses, physical properties and applications. Prog. Polym. Sci. 37 (2012) 907–974.
5. Ou X, Lu X, Chen S, Lu Q. Thermal conductive hybrid polyimide with ultrahigh heat resistance, excellent mechanical properties and low coefficient of thermal expansion. Eur. Polym. J. 122 (2019) 109368.
6. Chen TP, Young SJ, Chang SJ, Hsiao CH. Photoconductive gain of vertical ZnO nanorods on flexible polyimide substrate by low-temperature process. IEEE Sens. J. 11 (2011) 3457–3461.
7. Cooper R, Ferguson D, Engelhart DP, Hoffmann R. Effects of radiation damage on polyimide resistivity. J. Spacecr. Rockets. 54 (2017) 343–348.
8. Shen FY, Huang SE, Dow WP. Silver metallization of polyimide surfaces using environmentally friendly reducing agents. ECS Electrochem. Lett. 2 (2013) 45–48.
9. Chen JJ, An Q, Rodriguez RD, Sheremet E, Wang Y, Sowade E, Baumann RR, Feng ZS. Surface modification with special morphology for the metallization of polyimide film. Appl. Surf. Sci. 487 (2019) 503–509.
10. Nguyen THL, Cortes LQ, Lonjon A, Dantras E, Lacabanne C. High conductive Ag nanowire-polyimide composites: Charge transport mechanism in thermoplastic thermostable materials. J. Non. Cryst. Solids. 385 (2014) 34–39.
11. Akamatsu K, Ikeda S, Nawafune H. Site-Selective Direct Silver Metallization on Surface-Modified Polyimide Layers. Langmuir. 19 (2003) 10366–10371.
12. Tang QY, Chan YC, Wong NB, Cheung R. Surfactant-assisted processing of polyimide/multiwall carbon nanotube nanocomposites formicroelectronics applications. Polym. Int. 59 (2010) 1240–1245.
13. Akamatsu K, Shinkai H, Ikeda S, Adachi S, Nawafune H, Tomita S. Controlling interparticle spacing among metal nanoparticles through metal-catalyzed decomposition of surrounding polymer matrix. J. Am. Chem. Soc. 127 (2005) 7980–7981.
14. Chang TFM, Wang CC, Yen CY, Chen SH, Chen CY, Sone M. Metallization of polyimide films with enlarged area by conducting the catalyzation in supercritical carbon dioxide. Microelectron. Eng. 153 (2016) 1–4.
15. Choi DJ, Maeng JS, Ahn KO, Jung MJ, Song SH, Kim YH. Synthesis of Cu or Cu2O-polyimide nanocomposites using Cu powders and their optical properties. Nanotechnology. 25 (2014), 375604.
16. Kou H, Jia L, Wang C. Electrochemical deposition of flower-like ZnO nanoparticles on a silver-modified carbon nanotube/polyimide membrane to improve its photoelectric activity and photocatalytic performance. Carbon. 50 (2012) 3522–3529.
17. Chen Q, Sun Y, Wang Y, Cheng H, Wang QM. ZnO nanowires-polyimide nanocomposite piezoresistive strain sensor. Sensors Actuators, A Phys. 190 (2013) 161-167.
18. Babrekar HA, Jejurikar SM, Jog JP, Adhi KP, Bhoraskar SV. Low thermal emissive surface properties of ZnO/polyimide composites prepared by pulsed laser deposition. Appl. Surf. Sci. 257 (2011) 1824–1828.
19. Li D, Wu C, Ruan L, Wang J, Qui Z, Wang K, Liu Y, Zhang Y, Guo T, Lin J, Kim TW. Electron-transfer mechanisms for confirmation of contact-electrification in ZnO/polyimide-based triboelectric nanogenerators. Nano Energy. 75 (2020) 104818.
20. Shishino K, Yamada T, Arai M, İkeda M, Hirata H, Motoi M,

Hatakeyama T, Teshima K. A strongly adhering ZnO crystal layer: Via a seed/buffer-free, low-temperature direct growth on a polyimide film via a solution process. CrystEngComm. 22 (2020) 5533-5538.

21. Wu Z, Wu D, Qi S, Zhang T, Jin R. Preparation of surface conductive and highly reflective silvered polyimide films by surface modification and in situ self-metallization technique. Thin Solid Films. 493 (2005) 179–184.
22. Liu TJ, Chen CH, Wu PY, Lin CH, Chen CM. Efficient and Adhesiveless Metallization of Flexible Polyimide by Functional Grafting of Carboxylic Acid Groups. Langmuir. 35 (2019) 7212–7221.
23. Cetinel A, Artunç N, Tarhan E. The growth of silver nanostructures on porous silicon for enhanced photoluminescence: The role of AgNO3 concentration and deposition time. EPJ Appl. Phys. 86 (2019) 11301.
24. Aydemir G, Utlu G, Çetinel A. Growth and characterization of ZnO nanostructures on porous silicon substrates: Effect of solution temperature. Chem. Phys. Lett. 737 (2019) 136827.
25. Yang J, Wang Y, Kong J, Jia H, Wang Z. Synthesis of ZnO nanosheets via electrodeposition method and their optical properties, growth mechanism. Opt. Mater. 46 (2015) 179–185.
26. Patterson AL. The scherrer formula for X-ray particle size determination. Phys. Rev. 56 (1939) 978–982.
27. Siegel J, Polívková M, Kasálková NS, Kolská Z, Švorčík V. Properties of silver nanostructure-coated PTFE and its biocompatibility. Nanoscale Res. Lett. 8 (2013) 1–10.
28. Sessler GM, Hahn B, Yoon DY. Electrical conduction in polyimide films. J. Appl. Phys. 60 (1986) 318–326.